

Chapter 3

Experimental Method

3.1 Coordinate Systems for Atomic Physics and Atomic Beam Optics

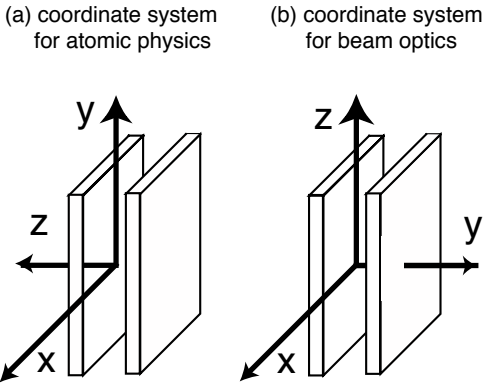


Figure 3.1: Coordinate systems used for (a) atomic physics and (b) beam trajectory calculations.

In sections discussing atomic physics and quantum mechanics we use the coordinate system (Fig. 3.1a) in which the electric field is parallel to the “ z ” direction, the atoms travel parallel to the “ y ” (vertical) direction, and the short axis of the electric field plates is parallel to the “ x ” direction. In sections discussing francium or cesium beam optics (such as Sections 3.12, 3.13, and Chapter 10), we use a coordinate system (Fig. 3.1b) in which the atoms move parallel to the “ z ” direction (vertical), the electric field is parallel to the “ y ” direction, and the short axis of the electric field plates is again parallel to the “ x ” direction.

Maintaining two coordinate systems minimizes the risk of an error in one of the calculations by allowing the experts in quantum calculations and in beam optics to use their respective customary coordinate systems.

3.2 Laser Propagation Directions

The atoms in the francium fountain may be state prepared using a laser propagating along any of the x , y , or z axes (Fig. 3.1a), or even along some arbitrary axis, and the atoms state analyzed using a laser propagating along any axis subject to constraints imposed by the choice of direction and polarization of the state preparation laser.

In sections discussing the calculations of motional systematic effects already published in Wundt, Munger and Jentschura (Ref. [WMJ12]), the state preparation laser propagates in the (atomic physics) z direction as it does in Ref. [WMJ12]. This allows the material in this comprehensive publication to be accessible without extensive recalculation.

In discussions of francium beam heating by laser optical pumping, the state preparation laser propagates in the x direction, which is the direction that we expect to use (at least initially) in the EDM experiment. For state preparation, which occurs before atoms enter the electric field, the francium beam transport is less sensitive to heating from excitation in the x direction than in the electric field direction, because there is more space for the cloud of atoms to expand in the x direction. At state analysis, the atoms have already passed through

the confines of the electric field plates, are accelerating in free fall, and have little time left until they are recovered: they can be optically pumped with laser beams in any direction with no loss due to heating.

In several places (Sections 3.7.5, 5.6) we use calculations in which the state preparation laser propagates in the vertical direction. For atoms with F odd (^{211}Fr , $F = 5$ and ^{221}Fr , $F = 3$, but not Cs, $F = 4$), the direction of laser propagation needs to be tipped to remove the $M = \pm 1$ states and might present some engineering issues. These instances will be recalculated to allow the state preparation laser to enter from the x direction with a slight tipping towards the z axis (but not enough to add any appreciable beam heating).

Should francium beam heating or laser propagation direction ever become an issue, it is possible to state prepare the atoms using laser beams in the z direction and using adiabatic rapid passage. This would produce little or no beam heating. However it is an additional experimental complication that may not be needed and so its consideration has been deferred. For the cesium prototype magnetic fountain (Section 7.1), which has no electric fields, there is no distinction between the z and x directions.

3.3 Overview of the Experiment

Loading francium (Section 3.11)

The traditional method of capturing francium atoms into a magneto-optic trap (MOT) is to first have francium ions from an accelerator land on a yttrium metal foil where they neutralize because yttrium's work function of 3.1 eV is lower than francium's ionization potential of 4.073 eV. After a period of collection (about ten seconds for our EDM experiment), the foil is heated, evaporating the francium into a dryfilm-coated [SRW94] glass cell. About once in every 5000 collisions of a Fr atom with the room-temperature dryfilm-coated wall, the Fr atom will recoil with sufficiently low kinetic energy [MvdS99a] to be further slowed by, and then captured into, a magneto-optic trap (MOT)

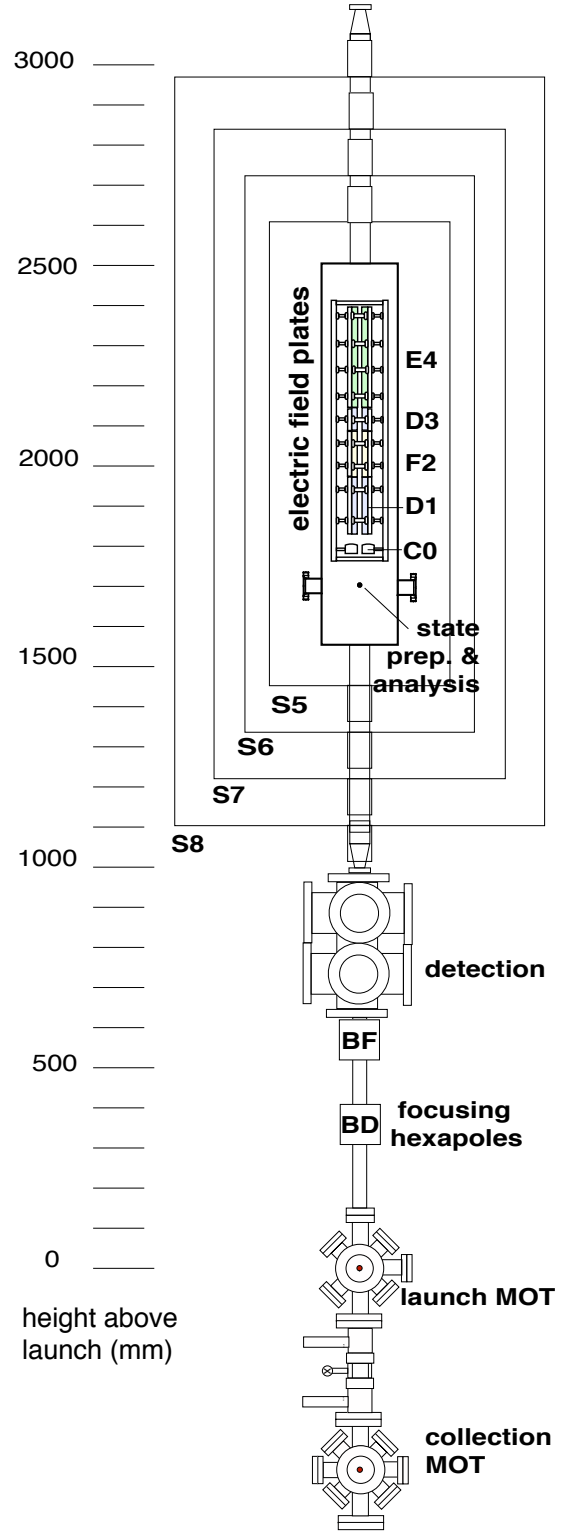


Figure 3.2: Schematic of the Fr fountain electron EDM apparatus.

Table 3.1: Key Experiment Parameters

Item	Value
Global quantities	
Experiment goal	$1.3 \times 10^{-50} \text{ C m}$
Primary isotope and state	$^{211}\text{Fr } 7^2S_{1/2}, F = 5$
Source of ^{211}Fr	TRIUMF ISOL
Secondary isotope and state	$^{221}\text{Fr } 7^2S_{1/2}, F = 3$
Source of ^{221}Fr	^{225}Ac decay ($t_{1/2} = 10 \text{ d}$)
Atom for null EDM and development	Cs $6^2S_{1/2}, F = 4$
Quantities related to sensitivity	
Francium enhancement factor R	903
Electric field (initial – goal)	$(9.6 \times 10^6 - 1.4 \times 10^7) \text{ V/m}$
Energy change of Fr atom	
with electron EDM of $1.3 \times 10^{-50} \text{ C m}$	
from electric field reversal of $9.56 \times 10^6 \text{ V/m}$	$2.27 \times 10^{-40} \text{ J } (3.4 \times 10^{-7} \text{ Hz})$
Time in electric field	0.67 s
Detected atoms needed	4.6×10^{13}
Anticipated TRIUMF ^{211}Fr intensity	$5 \times 10^9/\text{s}$ (now $1.3 \times 10^9/\text{s}$)
Capture efficiency of Fr into trap	
using dryfilm	0.4% to 1.5%
from high efficiency slower	$\approx 8\%$
Fraction of launched atoms returned	0.79
Counting time to reach $1.3 \times 10^{-50} \text{ C m}$	200 h
Time between launches	10 s
Atoms per launch (incl. recovered atoms)	6.4×10^8
Magnetic field sensitivity	2.9 fT (4 launches)
Quantities related to magnetic noise	
Ambient (room) magnetic noise	$\pm 33 \text{ nT}$
Experimental magnetic noise limit	1 fT
Radial shielding factor	$\geq 3.3 \times 10^7$
Quantities related to systematic effects	
Magnetic field (initial – goal)	$\leq 200 \text{ fT} - \leq 20 \text{ fT}$
E -field transition region magnetic field	$\leq 163 \text{ fT}$ (a)
Motional magnetic field (at 3.0 m/s)	330 pT
Allowed discharge current	5 nA – 34 pA (worst case)

(a) May be revised upward after changes in the electrostatic lens design.

formed by the intersection of six laser beams. The dryfilm coated wall technique has been used in all francium MOTs to date [SGG⁺96, LCV⁺97, AGLAO03, TBP⁺12]; however a francium atom is more likely to stick to the dryfilm than to be captured into the MOT so the efficiency is presently only about one percent.

An alternative method of producing slow francium atoms for capture into a MOT is to form a thermal beam which is then slowed with a counter propagating laser beam while the atoms pass through a magnetic field. The magnetic field changes along the beam path so as to keep the slowing atoms in resonance with the laser (Zeeman slower). The combination of a thermal source and Zeeman slower can produce bright beams of alkali atoms [HDV⁺96, LSHM99, SVH05], but is usually inefficient in its use of atoms. A design for a high efficiency Zeeman slower using multistage transverse cooling, magnetic focusing, and an orthotropic source [DGG96] is described in Chapter 10.

Forming a francium fountain (Section 3.11.3)

The francium atoms are first trapped in a collection MOT, and then transferred to a launching MOT. One implementation of this two-MOT system is shown in Fig. 3.2, where isolation valves allow for the rapid replacement of a collection MOT if the dryfilm coating should deteriorate during an accelerator run. The advantage of a two-MOT system is that the first MOT (collection MOT) can be optimized for collection and the second MOT can be optimized for launching (launch MOT). The launch MOT does not need a dryfilm coating, allowing for much better vacuum and better optical quality for the laser beams that do not need to pass through dryfilm coated windows. The packet of atoms is then launched nominally once every ten seconds but can be launched more or less often.

Each launch forms a single packet of atoms. Launch velocity is about 6.8 m/s (See Fig. 3.23). Immediately after launching, the atoms are sub-Doppler cooled in the moving frame to about $2\mu\text{K}$.

After cooling, the atoms enter a weak vertical solenoid magnetic field (not shown) and are optically pumped into the $|F = 5, M = -5\rangle$ state, using laser light propagated vertically (an up beam and a down beam of light). They then enter a sextupole magnet lens doublet that uses permanent magnets in a Halbach configuration [Hal80]. The beam transport system described in Section 3.12.

State preparation & analysis (Sec. 3.7, 3.8)

The atoms ascend undisturbed through the detection region and at about 1.5 m above their launch point enter the magnetically shielded region. (The shields are labeled S5–S8 in Fig. 3.2.) The shields, made from 3.17 mm thick mu-metal (Carpenter HyMu-80TM), are described in Chapter 8 and the shielding requirements are discussed in Section 4.4. The shields are fully demagnetized as described in Section 8.5. Remaining static magnetic fields and gradients are further reduced by magnetic field nulling coils (described in Section 5.5.2).

State preparation for the ascending atoms and state analysis for the descending atoms take place about 25 cm above the end cap of the inner magnetic shield¹(S5).

The atoms are state prepared by optical pumping with linearly polarized laser light propagating parallel to the z axis and whose axis of linear polarization in the x - y plane makes an angle θ with respect to the x axis. For $\theta = 0$ the atoms are pumped into the $|F = 5, M = 0\rangle$ state, but for $\theta \neq 0$ optical pumping produces a coherent superposition of $|F = 5, M = \pm 5\rangle$, with non-zero amplitudes for $|F = 5, M = \pm 3\rangle$ and $|F = 5, M = \pm 1\rangle$. The different M levels have sensitivities to the EDM that scale approximately as M and sensitivities to motional systematic effects that scale as $(1/M)^2$ and higher powers. By changing the angle of the linear polarization continuously between 0 and $\pi/2$ we can change both the relative and absolute sensitivity to an EDM and to motional systematic effects.

¹This distance helps minimize magnetic field gradients from the end cap (See Fig. 8.7) and helps reduce z -direction nonuniformity in the magnetic nulling field due to image currents.

In this way (see Fig. 5.5) it is possible to:

1. Maximize the sensitivity to the EDM (but not achieve the lowest possible systematic sensitivity),
2. Reverse the sign of the residual motional systematic effects relative to the sign of the EDM,
3. Further minimize the sensitivity to motional systematic effects (at some cost to EDM sensitivity), or even
4. Minimize the sensitivity to the EDM while maintaining near maximum sensitivity to the motional systematic effects.

This is better than any “comagnetometer” because the comparison is between the same atoms with the same transition probabilities following the same trajectory through the same electric (and any remnant magnetic) fields and laser beams. And this is in addition to other features that can already suppress the motional systematic effects to below the experimental limit.

The optical state preparation and analysis is done in a region of zero electric field, no applied magnetic field, and with residual magnetic fields and magnetic field gradients as small as can possibly be achieved. State preparation and analysis of atoms in a fountain in zero electric field and magnetic fields of less than 1 nT was demonstrated in Ref. [AMG07].

The francium atoms enter the electric field, slow under the influence of gravity, turn around, and fall out of the electric field plates, having spent about 0.67 s in the electric field. The atoms are then optically state analyzed (Section 3.8) in the same location as they were state prepared. The analysis puts some of the ^{211}Fr atoms, all initially in the $F = 5$ hyperfine level, into the $F = 4$ hyperfine level: it is the ratio of the atoms in the $F = 5$ level to the atoms in the $F = 4$ level that is the measured signal. The fraction of atoms transferred from the $F = 5$ hyperfine level to the $F = 4$ hyperfine level is measured (Section 3.10) on the descent in the detection region, just above the focusing sextupole doublet.

Electric fields (Chapter 9)

After state preparation, the atoms enter an electric field of $\approx 1 \times 10^7 \text{ V/m}$, produced by applying $\pm 50 \text{ kV}$ across a pair of electric field plates with a 0.5 cm half gap². The lower portion of the electric field plates form an electrostatic focusing triplet lens. Along with the magnetic sextupole doublet, just above the launch MOT, it compensates for the defocusing effect of the inhomogeneous electric fields seen by the atoms entering and exiting the electric field plates [Kal11, KAG05, MDG99].

Without electrostatic focusing, few francium atoms would travel through the electric field plate and return to be detected. With the focusing (Section 3.12) most of the francium atoms return and can be recaptured into the launching MOT. The electric field plate curvatures needed for focusing are slight, changing the gaps by 200 microns or less over the center one centimeter. The lenses operate at voltages nearly identical to the voltage of the main electric field plates: slight differences allow for tuning. They have negligible effect on systematic cancellation (Section 5.6).

The electric field plates are made from glass with a bulk resistivity of about $10^9 \Omega \text{ cm}$, allowing them to be sufficiently conducting to maintain electric fields. The glass will be lithium-alumino-silicate glass near room temperature (preferred) or soda-lime glass heated above 100°C . Compared to the use of metal or of (indium-tin-oxide) coated insulating glass, the use of low-resistivity bulk glass reduces magnetic Johnson noise (magnetic fields caused by the thermal motion of electrons in conductors) by orders of magnitude, as discussed in Ref. [Mun05], Section 4.4, and Chapter 9. Electric field plates with a low-resistivity glass cathode will also sustain higher electric fields than metal or coated-glass electrodes. The earlier use of glass electric field plates of similar design for a thallium atomic beam experiment is described in [Gou76].

²This is an initial design field intended to make it easier to build the high voltage feedthroughs and other high voltage components (See Sections 7.2, 9.4). By the time ^{211}Fr is run we expect the electric field to be $\approx 1.4 \times 10^7 \text{ V/m}$.

EDM measurement & electric field reversal

In ^{211}Fr , the presence of an EDM or a magnetic field in general introduces a phase difference between the states $|5, M\rangle$ and $|5, -M'\rangle$ (we except the case $M = M' = 0$). If $M = M'$, the phase difference due to the magnetic field is subtracted out when the electric field is reversed. In the absence of an EDM, a static electric field produces the same Stark effect phase difference regardless of the polarity of the field. The experiment is insensitive to an incomplete reversal of the electric field.

3.4 Interaction of Electric and Magnetic Dipole Moments with External Fields

The effective Hamiltonian within a manifold of states of total spin F has contributions from the permanent electric and magnetic dipole moments and from a \mathcal{CP} -conserving electric dipole moment induced in the polarizable atom by an external electric field (tensor polarizability³).

The contribution of the permanent electron EDM is

$$H_{\text{EDM}} = \frac{R(-d_e)\vec{F} \cdot \vec{E}}{F\hbar}, \quad (3.1)$$

where \vec{F} is the operator representing the total angular momentum of the atom, $\vec{F} = \vec{I} + \vec{J}$ where \vec{I} is the angular momentum of the nucleus and (in ground-state alkali atoms) \vec{J} is the atomic spin. (\vec{F} has S.I. units of J-s.) As before, d_e is the electron EDM, and R is the enhancement factor.

The contribution from the magnetic dipole moment

³The electric field causes the nucleus and electron clouds to move in opposite directions, inducing an electric dipole moment, which then interacts with the electric field to produce an energy shift quadratic in the electric field. There are very small differences in the polarizability of the $F = I + 1/2$ and $F = I - 1/2$ states and even smaller differences in polarizability, caused by relativistic effects, between states of the same F but different M . The resulting shifts are quadratic in M .

(Zeeman effect) is

$$H_{\text{Zeeman}} = \frac{\mu_B g_F \vec{F} \cdot \vec{B}}{\hbar}, \quad (3.2)$$

where $\mu_B \approx 9.27 \times 10^{-24} \text{ JT}^{-1}$ is the Bohr magneton and $g_F \approx 1/5$ is the Landé g factor for the ^{211}Fr $F = 5$ manifold.

Relative sensitivities to a magnetic and permanent electric dipole moment

Neglecting, for a moment, the induced electric dipole moment, when there are fields in the z direction only, the Hamiltonian H_z for the system reduces to

$$H_z = -\left(\mu_B g_F B_z + \frac{R d_e E_z}{F}\right) \mathbf{F}_z, \quad (3.3)$$

where we have defined the dimensionless operator⁴ $\mathbf{F} = \vec{F}/\hbar$.

Because the electron's magnetic and permanent electric dipole moments are both proportional to the electron spin, francium's sensitivity to the EDM is maximized only when the sensitivity to the magnetic dipole moment is also maximized. An experiment sensitive to a nonzero value of d_e will require an observable O whose value depends upon the operator \mathbf{F}_z . Such an observable maximizes sensitivity to the term $R d_e E_z$ if and only if it maximizes sensitivity to the term $\mu_B B_z$, because

$$\frac{\partial O}{\partial d_e} = E_z \frac{R}{\mu_B} \frac{\partial O}{\partial B_z}, \quad (3.4)$$

and so $O(d_e)$ and $O(B_z)$ attain their maxima together.

The interaction energy of a francium atom in a state $|F, \pm F\rangle$, due to an electron EDM of d_e of $1.3 \times 10^{-48} \text{ C m}$ (present limit) in an electric field of the experiment of 10^7 V/m , is $R d_e E = 1.2 \times 10^{-38} \text{ J}$. By comparison, the magnetic field needed to achieve the same interaction energy is $1.3 \times 10^{-15} \text{ T}$.

⁴The “Wundt-Munger-Jentschura” convention is that \vec{F} is an angular momentum with units of \hbar , and \mathbf{F} (that is in boldface) is \vec{F}/\hbar , and F (that is in math italic font) is the largest expectation value of \mathbf{F} , so for ^{211}Fr we have $F = 5$, a dimensionless integer.

Tensor polarizability

In the electric field E_z , the polarizability contributes to each level $|FM\rangle$ an energy shift

$$-\frac{1}{2}(\alpha_0 + \alpha_{FM}) E_z^2, \quad (3.5)$$

where α_0 is the scalar polarizability, which is independent of F and M , and α_{FM} is the tensor polarizability. The tensor polarizability splits [DFBD10, San67] into the sum

$$\alpha_{FM} = \alpha_F^S + \frac{3M^2 - F(F+1)}{F(2F-1)} \alpha_F^T, \quad (3.6)$$

where all dependence on the magnetic quantum number M is explicit. The parts of α_0 and of α_{FM} that are independent of F contribute to a global shift of the whole hyperfine manifold and so introduce no change in the atomic state other than a global phase. Dzuba et al. [DFBD10] have calculated $\alpha_F^T = -1.63 \times 10^{-11} \text{ Hz V}^{-2} \text{ m}^2$ and $5.06 \times 10^{-12} \text{ Hz V}^{-2} \text{ m}^2$ for ^{211}Fr and ^{221}Fr , respectively; the splittings are shown in Fig. 3.3.

Isolating the terms that are relevant for the quantum dynamics within the F -manifold, this gives an effective Hamiltonian

$$H_{\text{Stark}} = A_S E_z^2 F_z^2, \quad (3.7)$$

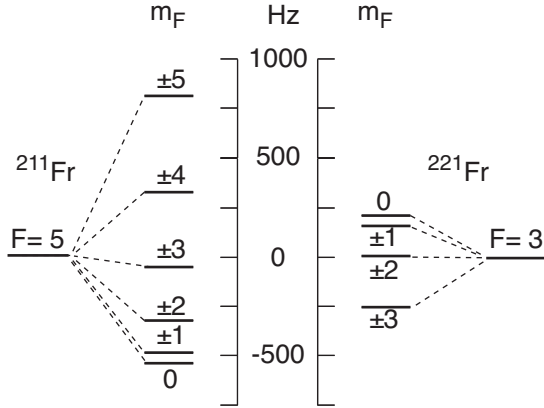


Figure 3.3: Energy of the francium M states of the $7S_{1/2}$ ground state upper hyperfine level in an electric field of 10^7 V/m , with no EDM and zero magnetic field. The left side is ^{211}Fr and the right side is ^{221}Fr .

where A_S is given by

$$A_S = \frac{3}{2F(2F-1)} (-\alpha_F^T). \quad (3.8)$$

The total effective Hamiltonian then is the sum of the tensor polarizability term, the EDM term, and the Zeeman term,

$$H = A_S \mathbf{F}_z^2 E_z^2 + \mu_B g_F \mathbf{F} \cdot \vec{B} - \frac{R d_e}{F} \mathbf{F}_z E_z. \quad (3.9)$$

In constant magnetic field B_z and constant electric field E_z , an atom that is in the state $|FM\rangle$ at time $t = 0$ acquires over time a phase

$$|FM\rangle \rightarrow \exp \left[\frac{-i}{\hbar} t \left(\left\{ -\frac{R d_e}{F} E_z + g_F \mu_B B_z \right\} M + A_S E_z^2 M^2 \right) \right] |FM\rangle. \quad (3.10)$$

If the magnetic and electric fields are not constant in time, the phase advance is given by

$$|FM\rangle \rightarrow \exp \left[\frac{-i}{\hbar} \left(\{E_1 + B_1\} M + E_2 M^2 \right) \right] |FM\rangle, \quad (3.11)$$

where

$$\begin{aligned} E_1 &= \frac{R d_e}{F} \int_0^t E_z dt, \\ B_1 &= g_F \mu_B \int_0^t B_z dt, \\ E_2 &= A_S \int_0^t E_z^2 dt. \end{aligned} \quad (3.12)$$

With electric field quantization, the net phase advances experienced by the atom between state preparation and state analysis are the important quantities. A key part of the experimental method is setting B_1 and E_2 such that the contribution to the phase advance due to each is an integer multiple of π (Sections 3.7.3, 3.7.4).

3.5 Introduction to Motional Systematic Effects and Electric Field Quantization

Because the electron’s magnetic and electric dipole moments are both proportional to the electron spin, magnetic fields that change synchronously with the electric field can mimic an EDM. Motional systematic errors in electron EDM experiments arise from the interaction between two kinds of magnetic field on an atom: those from static magnetic fields, and from the motional magnetic field

$$\vec{B}_{\text{mot}} = \vec{v} \times \vec{E}/c^2 \quad (3.13)$$

from the Lorentz transform of an atom’s motion through the static electric field.

For a fountain with 3 m/s atoms in an electric field of 10^7 V/m, the motional magnetic field is 3.3×10^{-10} T, and would be a factor of 100 or more larger for a thermal velocity beam.

The motional magnetic field is perpendicular to the electric field and to the motion of the atom, and exactly reverses when the electric field or the atomic velocity reverses. With the presence of a component of static magnetic parallel to \vec{B}_{mot} , the magnitude of the *total* magnetic field changes upon electric field reversal or velocity reversal. Unfortunately, static fields are always present, either as remnant magnetic fields or as externally applied magnetic fields (used in previous electron EDM experiments to lift the degeneracy between M states).

Systematic errors enter through eigenvalue shifts, but also through transitions induced between states, and through changes in the phase of atomic wavefunctions; the “geometric phase” is one such phase whose effect lies at or just below the present experimental upper limit on the electron EDM [RCSD02, Reg01].

Compared to thermal beams of atoms with typical velocities of several hundred m/s, a fountain provides improved rejection of systematic effects through the low velocity in the electric field region and the fountain geometry in which the vertical component of the atomic velocity, and hence \vec{B}_{mot} , reverses as each atom rises and falls.

The reciprocal of the time spent in the electric field (transit time broadening) by slow atoms is about 1.5 Hz. If the residual magnetic fields are sufficiently small, it is possible for the electric field of $\approx 10^7$ V/m (see Fig. 3.3) to itself set and maintain the axis of quantization.

To achieve electric field quantization, no external magnetic field is applied and the remaining magnetic fields are set as close to zero as possible so that the ratio of the interaction energy with the electric field ($H_{\text{Stark}} = A_S E_z^2 F_z^2$) to the interaction with the magnetic field ($H_{\text{Zeeman}} = \mu_{BGF} \vec{F} \cdot \vec{B}/\hbar$) is as large as possible. This ratio is $\sim 10^4$ and $\sim 10^5$ for magnetic fields (parallel to the electric field) of 200 fT and 20 fT, respectively.

Electric field quantization transforms the way in which motional systematic effects enter from being linear in applied electric field and hence indistinguishable from an EDM, to being a higher order effect, generally proportional to $1/E^3$ and higher inverse powers of the electric field. This and other dependencies, discussed in Chapter 5, help to distinguish an EDM from a motional systematic effect. A full calculation (“Suppression of motional magnetic field systematic effects in atomic fountain electron electric dipole moment experiments”) has been published by Wundt, Munger and Jentschura [WMJ12]. Electric field quantization⁵ was demonstrated in a slow atom electron EDM proof-of-principle experiment by Amini, Munger, and Gould [AMG07].

As an example of how electric field quantization transforms the experiment and of which factors become important, we use the results of a simple perturbation calculation to examine the eigenvalue shift W_{sys} of the ^{211}Fr $F = 5$ hyperfine state due to a small net velocity in the “ x ” direction, parallel to the electric field plates. The equations are found in Ref. [AMG07] and we jump to the term that is odd in the electric field and in M :

⁵Earlier uses of electric field quantization with thermal beams are described by Player and Sandars [PS70], who set an electron EDM limit using a metastable state of xenon, and by Gould [Gou76] who studied thallium tensor polarizability.

$$\frac{W_{\text{sys}}}{h} = -2K_2 \frac{(g\mu_B)^3 B_{\perp\text{res}} \vec{B}_{\text{mot}} B_{\parallel}}{(2A_S E^2)^2}. \quad (3.14)$$

Here B_{mot} and A_S are defined in Eq. 3.13 and Eq. 3.8, respectively; and g and μ_B are the g -factor and Bohr magneton, respectively. Here also B_{\parallel} is the component of magnetic field parallel to the electric field, $B_{\perp\text{res}}$ is the component of magnetic field perpendicular to the electric field and parallel to \vec{B}_{mot} , and all of the M dependence is contained in K_2 which is compiled for different hyperfine levels in Table 3.2 and is given by

$$K_2(M) = \frac{M[4F(F+1)+1]}{2(4M^2-1)^2}. \quad (3.15)$$

Table 3.2: Values of K_2				
M	K_2			
	$F=5$	$F=4$	$F=3$	$F=2$
5	0.031			
4	0.061	0.041		
3	0.148	0.099	0.060	
2	0.538	0.36	0.218	0.11
1	6.72	4.5	2.722	1.39
0	0.0	0.0	0.0	0.0
-1	-6.72	-4.5	-2.722	-1.39
-2	-0.538	-0.36	-0.218	-0.11
-3	-0.148	-0.099	-0.060	
-4	-0.061	-0.41		
-5	-0.031			

Equation 3.14 is odd in E (through \vec{B}_{mot}) and odd in M (through K_2) and thus mimics an EDM. Equation 3.14 has a single power of E in the numerator (through the motional magnetic field) and 4 powers of E in the denominator, resulting in a $1/E^3$ dependence.

From Eq. 3.14 and Eq. 3.15, some of the features of an experiment with small motional systematic effects become clear: a high tensor polarizability, high electric field, small velocity, and a large ratio $|M|/F$ (and especially choosing $|M| \neq 1$), lead to the smallest residual systematic effect. Reducing magnetic fields is paramount. This informs

our choice of ^{211}Fr with its high tensor polarizability [DFBD10]. Reducing magnetic fields through magnetic shielding, effective demagnetization of the shields (which are ferromagnetic), and the use of magnetic field coils to null any remnant magnetic field, are also necessary (Section 5.5).

Table 3.3 shows, for different atoms with net transverse velocity of $v_x = 2 \text{ mm/s}$ (and so $\vec{B}_{\text{mot}} = 2.2 \times 10^{-13} \text{ T}$), the shift upon reversing an electric field of 10^7 V/m , when the residual magnetic fields have $B_{\parallel} = B_z = 2 \times 10^{-13} \text{ T}$ and $B_{\perp\text{res}} = B_y = 2 \times 10^{-13} \text{ T}$. The shift of $3.9 \times 10^{-13} \text{ Hz}$ in ^{211}Fr corresponds to a false electron EDM of $3 \times 10^{-56} \text{ C m}$ (about a factor of 10^6 smaller than the sensitivity of the proposed experiment).

Table 3.3: Motional Systematic from a Transverse Velocity of 2 mm/s and for $|M| = F$

Atom	F	Tensor Polarizability ^(a) (Hz V ⁻² m ²)	Systematic Shift ^(b) (Hz)
^{211}Fr	5	1.6×10^{-11}	3.9×10^{-13}
^{221}Fr	3	5.1×10^{-12}	7.7×10^{-12}
^{133}Cs	4	3.7×10^{-12}	1.0×10^{-11}
^{87}Rb	2	1.4×10^{-12}	1.9×10^{-10}
^{85}Rb	3	4.5×10^{-13}	9.9×10^{-10}

(a) Calculated values for $^{211,221}\text{Fr}$ are taken from Ref. [DFBD10], experimental values for ^{133}Cs are taken from Ref. [GLW69, ORW03], and experimental values for $^{87,85}\text{Rb}$ are taken from Ref. [GLW69].

(b) Due to reversing an electric field of $1 \times 10^7 \text{ V/m}$ and with remnant magnetic fields $B_{\perp\text{res}} = B_{\parallel} = 2 \times 10^{-13} \text{ T}$.

However this is not the largest source of motional systematic effects.

3.6 Sensitivity of a Coherent Superposition of $|F, M\rangle$ States

Because the electron's magnetic and permanent electric dipole moments are both proportional to the electron spin, the behavior of an atom with a magnetic dipole moment in a magnetic field will be similar to the behavior of an atom with a permanent electric dipole moment in an electric field. To simplify the discussion of the sensitivity of a coherent superposition of states, we therefore imagine turning off the electric field—something that can also be done in the experiment, leaving only a magnetic field.

In constant magnetic field B_z , an atom that is in the state $|F, M\rangle$ at time $t = 0$ acquires over time t a phase

$$|F, M\rangle \rightarrow \exp\left(+i\frac{g_F\mu_B B_z}{\hbar F}Mt\right)|F, M\rangle. \quad (3.16)$$

If instead the initial state $|F, M\rangle$ is rotated about the z axis by an angle ϕ (where $\phi > 0$ corresponds to a rotation through an angle that is positive according to the usual right-hand rule) then the initial state acquires instead the phase

$$|F, M\rangle \rightarrow \exp(-iM\phi)|F, M\rangle. \quad (3.17)$$

Therefore if we apply a constant magnetic field for a fixed time, the effect is to rotate the initial state $|F, M\rangle$ by an angle

$$\phi = -\frac{g_F\mu_B B_z t}{\hbar F}. \quad (3.18)$$

Because μ_B is negative, a positive value of B_z corresponds to a positive angle ϕ .

An arbitrary state ψ in the hyperfine level is a linear superposition of the states $|F, M\rangle$, and can be written as

$$\psi = \sum_{M=-F}^F a_M |F, M\rangle, \quad (3.19)$$

where the numbers a_M are complex.

Rotation by an angle ϕ about the z axis changes the state to

$$\psi(\phi) = \sum_{M=-F}^F a_M e^{-iM\phi} |F, M\rangle, \quad (3.20)$$

or upon application instead of B_z , a magnetic field in the z direction changes the state to

$$\psi(\phi) = \sum_{M=-F}^F a_M \exp\left(\frac{i\mu_e B_z}{\hbar F}Mt\right) |F, M\rangle, \quad (3.21)$$

and so not only for the individual states $|F, M\rangle$ but for arbitrary states, the application of a constant magnetic field in the z direction effects a rotation of a state about the z axis by

$$\phi = -\frac{g_F\mu_B B_z t}{\hbar F}. \quad (3.22)$$

If F is an integer then the state $\psi(\phi)$ has a period⁶ of 2π .

Since the electron is purely spin-up in the state $|F, M = F\rangle$, and purely spin-down in the state $|F, M = -F\rangle$, for a system of spin F the superposition of states with the electron spin up $|F = 5, M = 5\rangle$ and spin down $|F = 5, M = -5\rangle$ is likely to be sensitive. The initial state is

$$\psi(0) = \frac{1}{\sqrt{2}}(|F, M = F\rangle + |F, M = -F\rangle), \quad (3.23)$$

where for ^{211}Fr we have $F = 5$.

If the state $\psi(0)$ is rotated about the z axis, for example by the application of a constant magnetic field B_z , then the new state $\psi(\theta)$ is

$$\begin{aligned} \psi(\theta) = \frac{1}{\sqrt{2}} [& \exp(+iF\theta)|F, F\rangle \\ & + \exp(-iF\theta)|F, -F\rangle], \end{aligned} \quad (3.24)$$

where $\theta = g_F\mu_B B_z t / F\hbar$.

The probability that an atom in the state $\psi(\theta)$ will be measured to be in the initial state $\psi(0)$ is

$$p(\theta) = |\langle\psi(0)|\psi(\theta)\rangle|^2, \quad (3.25)$$

⁶If F is a half-integer then the state $\psi(\phi)$ has a period 4π and a change of ϕ by 2π changes the sign of the wave function.

which is of course equal to 1 when $\theta = 0$.

The probability is periodic in θ with period 2π (and so has to return to the value of 1 for $\theta = 2\pi$). The probability remains 1 independent of θ if $\psi(0)$ is chosen to be one of the states $|F, M\rangle$; it dips below 1 if $\psi(0)$ is chosen to be a superposition of those states.

For the initial state of Eq. (3.23) the resulting function is

$$p(\theta) = |\langle\psi(0)|\psi(\theta)\rangle|^2 = \cos^2(F\theta), \quad (3.26)$$

which is plotted as the solid curve in Figure 3.4.

For just about any choice of the function ψ , the resulting curve $p(\theta)$ has a symmetric central peak at $\theta = 0$ that can be used as the basis for a magnetic field measurement or, with an electric field present, an EDM measurement.

Pick a particular angle θ ; suppose that one prepares the state $\psi(\theta)$, rotates it through a small angle ϕ about the z direction (an operation whose effect is to produce the state $\psi(\theta + \phi)$), and then computes the probability that the resulting state remains in the initial state; this probability is $p(\theta + \phi)$. For a positive value of θ , the probability decreases with increasing ϕ , and for a negative value of θ the probability increases, as is indicated by the dashed curve in Figure 3.4. Therefore for $\theta > 0$ the difference

$$p(-\theta + \phi) - p(\theta + \phi) \quad (3.27)$$

is positive for positive ϕ , and zero when ϕ is zero. The difference is sensitive to ϕ when θ is chosen to be at a point where $p(\theta)$ has a slope of large magnitude.

For the particular function p displayed in Fig. 3.4, the slope of maximum magnitude occurs at $\theta = \pi/(4F)$; this value of θ also marks the place where the probability falls to its half-maximum value of 1/2. For this choice of $\psi(0)$ and values for θ we find for ^{211}Fr (for which $F = 5$) just

$$\phi = p(-\pi/20 + \phi) - p(\pi/20 + \phi) + O(\phi^3). \quad (3.28)$$

This example shows explicitly how the presence of a small magnetic field (or with the electric field

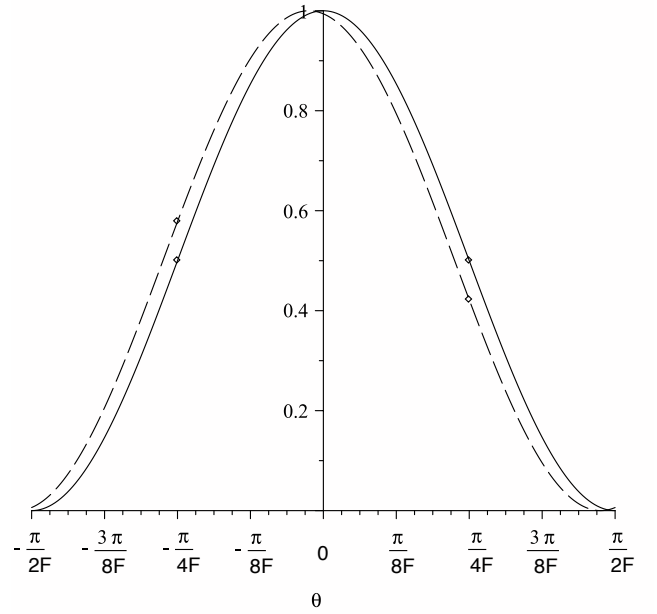


Figure 3.4: A plot of the probability that francium atom, in a state $\psi(\theta) = \frac{1}{\sqrt{2}}(e^{i5\theta}|5, 5\rangle + e^{-i5\theta}|5, -5\rangle)$, will be observed to be in the initial state $\psi(0) = \frac{1}{\sqrt{2}}(|5, 5\rangle + |5, -5\rangle)$ is shown as a solid line. The curve that results if the angle θ is shifted by a small positive amount ϕ is shown as the broken line; the difference $p(-\theta + \phi) - p(\theta + \phi)$ is sensitive to the value of ϕ and can therefore serve as a magnetometer.

present, an EDM) can be detected by measuring the corresponding small rotation by the angle ϕ .

The standard deviation of ϕ after N measurements is

$$\sigma_\phi = \frac{1}{2F} \frac{1}{\sqrt{N}}, \quad (3.29)$$

and the standard deviation of the error in the magnetic field⁷ is

$$\sigma_{B_z} = \frac{\hbar}{2|\mu_e|t} \frac{1}{\sqrt{N}}. \quad (3.30)$$

A practical magnetometer will not achieve the ideal but have

$$\sigma_{B_z} = c \times \frac{\hbar}{2|\mu_e|t} \frac{1}{\sqrt{N}}, \quad (3.31)$$

⁷This result holds only where we can make the assumption that changes in p are dominated by changes due to the slope of p , not to higher derivatives; and that assumption is violated where $p = 0$ and where $p = 1$ because the slope vanishes; it is also violated if the departure ϕ is so large that a linear approximation of p no longer represents the function.

where c is a constant of the rough order of unity that accounts for the increasing inefficiency of such a system with increasing atomic spin F . This constant is derived from our state analysis method (Section 3.8); the constant is unity for an ideal system of spin $1/2$. For ^{211}Fr which has $F = 5$ we have $c = 2.05$; smaller values of F have smaller values for c . If we express the error in terms of the number of atoms N_{launch} that are launched at once and return to be detected, we have

$$\sigma_{B_z} = c \times \frac{\hbar}{2|\mu_e|t} \frac{1}{\sqrt{N_{\text{launch}}}}, \quad (3.32)$$

For ^{211}Fr for the stated conditions, and for $N_{\text{launch}} = 10^8$ and a transit time from state preparation to analysis of 0.67 s, this is

$$\begin{aligned} \sigma_{B_z} &= 2.05 \\ &\times \frac{1.056 \times 10^{-34} \text{ J s}}{2 \times [9.27 \times 10^{-24} \text{ J/T}] \times 0.67 \text{ s}} \\ &\times \frac{1}{\sqrt{6.4 \times 10^8}} = 0.69 \text{ fT}. \end{aligned} \quad (3.33)$$

To make an actual magnetic field measurement four launches will be needed (see Section 3.9).

3.7 State Preparation

3.7.1 Preparing a Superposition

In this section we describe, in some detail, the method to create a superposition of M states that uses only polarized laser light. In accord with our goal of minimizing motional systematic effects by having the smallest possible magnetic fields, the state preparation is entirely optical, using only linearly polarized laser light: there are no applied static or oscillatory magnetic fields, and residual magnetic fields are set as close to zero as possible.

State preparation performed on the ascending ^{211}Fr atoms works as follows:

- It creates a superposition of $|F = 5, \pm M\rangle$ with non-zero amplitudes for $M = \pm 3$ and $M = \pm 1$.

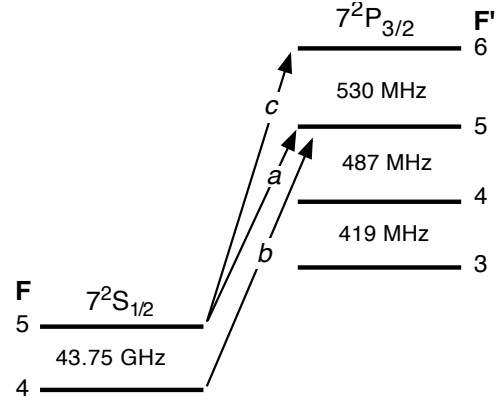


Figure 3.5: Transitions used for state preparation, analysis, and detection of ^{211}Fr . See text for explanation. The transition wavelengths are 718 nm.

- The method optically pumps the $7^2S_{1/2}, F = 5 \leftrightarrow 7^2P_{3/2}, F' = 5$ transition (where F' is the total spin of the upper hyperfine level): transition “a” in Fig. 3.5.
- The light propagates along the z direction
- The light is linearly polarized in the x - y plane at an angle of 0.21 radians to the x axis.

If the light were polarized parallel to the z axis, the state formed would be the $|F = 5, M = 0\rangle$ state, which upon rotation about the y axis (for instance by the application of a magnetic field in the y direction) would produce the desired states (See Section 3.7.2). As the experiment uses no applied magnetic fields, the desired states instead are produced by rotating the direction of laser polarization.

The probability that the state produced by rotation of the polarization by an angle θ to the x axis will be measured to be in the initial state $|F, M = 0\rangle$ is given by

$$p(\theta) = \frac{1}{16384} [63 \cos(5\theta) + 35 \cos(3\theta) + 30 \cos(\theta)]^2, \quad (3.34)$$

where the term in 5θ may be identified with $M = \pm 5$ and the terms in 3θ and θ with $M = \pm 3$ and ± 1 respectively. Note however that there are cross terms arising from the square.

Atoms that fall from the $7^2P_{3/2}, F' = 5$ state to the $7^2S_{1/2}, F = 4$ state are repumped using the $7^2S_{1/2}, F = 4 \leftrightarrow 7^2P_{3/2}, F' = 5$ transition (labeled “b” in Fig. 3.5).

State preparation and analysis is done in zero electric field not only for systematic but also for practical reasons: the large polarizabilities of all of the states in the $P_{3/2}$ and $P_{1/2}$ manifolds scramble the order of the levels, the selection rules for transitions, and even the quantum numbers of the levels, making it very difficult to optically pump selectively. These problems do not affect the ground state levels, which being S states have only very small hyperfine and tensor polarizabilities.

3.7.2 Equivalence of State Rotation by Magnetic Field and by Polarization Rotation

There is no efficient way to directly prepare a superposition of our ideal initial state

$$\psi(0) = \frac{1}{\sqrt{2}} \left((-1)^F |FF\rangle + |F, -F\rangle \right), \quad (3.35)$$

but we can start with the preparation of a pure $|F, M=0\rangle$ state and then rotate that state into a superposition of states that approximates our ideal state. When F is an integer, the state $|F, M=0\rangle$ may be prepared using light linearly polarized in the “ z ” direction, and tuned to the transition (for ^{211}Fr) $7S_{1/2}, F=5 \rightarrow 7P_{3/2}, F'=5$. All the atoms end in the $7S_{1/2}, F=5, M=0$ dark state.

If we then rotate the $|F, M=0\rangle$ state (where the quantization axis is along z) about the y axis by $\pi/2$ we produce a probability that the new state will be measured to be in the initial state $|F, M=0\rangle$ that is given by Eq. 3.34.

Shown in Fig. 3.6, is $p(\theta)$ together for comparison with the curve that would result from the use of the state in Eq. 3.35 consisting of a superposition of only $M = \pm 5$. The latter state would yield a magnetometer (via the $\delta\theta = (g_F\mu_B t / F\hbar) \cdot \delta B_z$) with the least shot-noise theoretically possible. In shifting to the rotated state, the center maximum broadens only a little, so the shot-noise achieved will be not far from ideal.

As we do not wish to rotate the state by applying a magnetic field, a laser polarization is used that will take us directly to, or at least close to, the desired

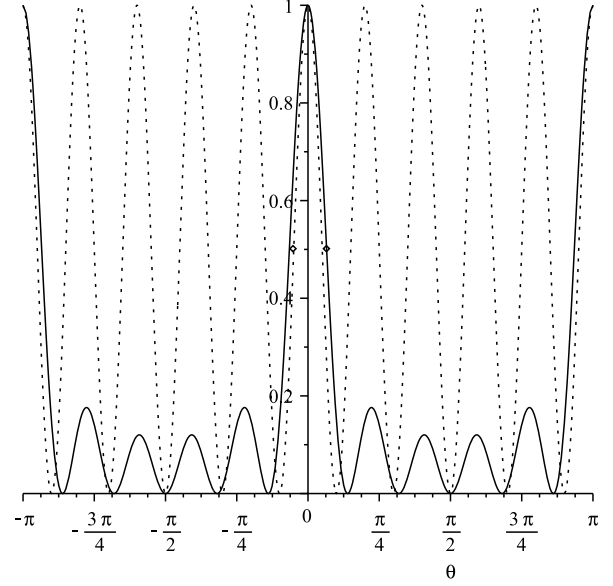


Figure 3.6: Plot of the curve $p(\theta)$ when a pure state $|50\rangle$ rotated by $\pi/2$ about the y axis is used as the initial state $\psi(0)$ (solid line), and when a pure state $(1/\sqrt{2})(|55\rangle + |5-5\rangle)$ is used as the initial state (dotted line). The latter yields the ideal statistical sensitivity. The change from ideal diminishes and somewhat shifts the side maxima, but leaves the central maximum almost unchanged. The solid points indicate the location of the half-maxima of the curves.

state. Consider the set of operations: create the state $\psi(\theta)$ that we need by taking a pure $|50\rangle$ state (using light linearly polarized along the z axis), then rotate that state by $\pi/2$ about the y axis, and then rotate the result by an angle θ about the z axis. This set of operations would be described mathematically as producing the state

$$R_z(\theta)R_y(\pi/2)|50\rangle. \quad (3.36)$$

Here R denotes an operator that rotates a state, the subscript indicates the axis of the rotation, and the argument denotes the angle, where the value of the angle is positive if the rotation of the state about the axis is anticlockwise according to the usual right-hand rule. This sequence of two rotations is equivalent to applying a sequence of magnetic fields. *However the same result can be accomplished merely by orienting correctly the axis of polarization of the laser that does the optical pumping.*

Consider the state that would result if the atom were pumped with light that propagated parallel to the z axis and whose axis of linear polarization in the x - y plane made a polar angle θ with respect to the x axis; call this state $|\Pi(\theta)\rangle$. If we were to rotate the axis of polarization and the state by $-\theta$ about the z axis, and then rotated both again by $-\pi/2$ about the y axis, then the axis of polarization would be parallel to the z axis. The state that polarization parallel to the z axis would produce would be the state $|50\rangle$, and so we must have

$$|50\rangle = R_y(-\pi/2)R_z(-\theta)|\Pi(\theta)\rangle. \quad (3.37)$$

Solving for $|\Pi(\theta)\rangle$ in terms of $|50\rangle$ gives

$$|\Pi(\theta)\rangle = R_z(\theta)R_y(\pi/2)|50\rangle, \quad (3.38)$$

and therefore the state $|\Pi(\theta)\rangle$, prepared with no magnetic fields at all, is precisely the state we desire.

3.7.3 Setting the Magnetic Field Phase Advance

We have so far discussed schemes as if the only interaction present is a tiny perturbation δB_z . This will result in only a tiny phase rotation about the z axis and consequently only a tiny change in $p(\theta)$ set near its point of maximum slope. But, if at the same time there is a large field B_z , or we include the interaction of the tensor polarizability with the electric field, then the state may be rotated to a region where $p(\theta)$ is much less sensitive to changes in θ .

To see how large a magnetic field B_z can be tolerated, we examine a superposition of the $|F = 5, M = \pm 5\rangle$ states where $p(\theta) = \cos^2(F\theta)$ and $\theta = g_F\mu_B B_z t / F\hbar$. With a transit time of 0.67 s from state preparation to analysis, we have $F\theta = 2\pi$ for $B_z = 5.3 \times 10^{-10}$ T. And as we are working with a central maximum of roughly $\pi/8$ this requires $B_z \ll 3.3 \times 10^{-11}$ T.

We note that in a time-dependent magnetic field B_z , any state

$$\psi = \sum_{M=-F}^F a_M |F, M\rangle \quad (3.39)$$

evolves to

$$\begin{aligned} \psi(t) = & \sum_{M=-F}^F a_M \\ & \times \exp\left(iM \frac{1}{\hbar} \frac{\mu_e}{F} \int_0^t B_z(t') dt'\right) |F, M\rangle, \end{aligned} \quad (3.40)$$

and so returns to itself when

$$\varphi_{\text{mag}} \equiv -\frac{1}{\hbar} \frac{\mu_e}{F} \int_0^t B_z(t') dt' \quad (3.41)$$

is an integer multiple of 2π . For the case $F = 5$ the particular initial states $\Pi(\theta)$ may be computed to be

$$\Pi(\theta) = \begin{pmatrix} (-3\sqrt{7}/16)(\cos(5\theta) - i\sin(5\theta)) \\ 0 \\ (+\sqrt{35}/16)(\cos(3\theta) - i\sin(3\theta)) \\ 0 \\ (-\sqrt{30}/16)(\cos(\theta) - i\sin(\theta)) \\ 0 \\ (+\sqrt{30}/16)(\cos(\theta) + i\sin(\theta)) \\ 0 \\ (-\sqrt{35}/16)(\cos(3\theta) + i\sin(3\theta)) \\ 0 \\ (+3\sqrt{7}/16)(\cos(5\theta) + i\sin(5\theta)) \end{pmatrix}, \quad (3.42)$$

and so have $a_M = 0$ for M even; such states return to themselves (except for an irrelevant global factor of -1) when φ_{mag} is any integer multiple of π , not 2π . Therefore the results of the scheme for $F = 5$ are a function of φ_{mag} with period π ; and the same proves to be true for any integer value of F . Thus the function of the magnetometer to detect a small perturbation δB_z that turns on and off is unchanged even if a larger, remnant magnetic field B_z is present, provided we can arrange for φ_{mag} to be an integer.

We shall therefore assume that the condition

$$-\frac{1}{\hbar} \frac{\mu_e}{F} \int_0^t B_z(t') dt' = k_\beta \pi, \quad (3.43)$$

where k_β is an integer, has been established before we try to detect the perturbing field δB_z .

Physically there will be some spatially varying remnant magnetic field in the apparatus; as an atom rises and falls in the atomic fountain it will experience, in its rest frame, a time-dependent field $B_z(t)$

that contributes to this integral. We use the atoms themselves to measure the departure of the phase φ_{mag} from $k\beta\pi$. By putting currents through wire coils (Section 5.5), we can provide just such laboratory magnetic fields as will eliminate the effect of the remnant magnetic fields *without having to zero those remnant fields everywhere*.

For suppression of motional systematic effects we ideally want the remnant magnetic field $B_z(t) = 0$. However to operate the experiment we need not eliminate $B_z(t)$ everywhere, or even know what its value is everywhere or know what fields a coil might everywhere provide; all we have to do is measure the departure of the integral from an integer and adjust the current in a nulling coil so that this departure is zero.

3.7.4 Setting the Electric Field Phase Advance

Now that we have this basic magnetometer, we wish to further adapt it to measuring an electric dipole moment. This requires applying a large electric field to the atoms, and therefore requires consideration of the Stark effect. Before we examine that, we look at the effect of global phases. Given two wavefunctions ψ_1 and ψ_2 , and any operator A , it is plain that the value of

$$|\langle \psi_1 | A | \psi_2 \rangle|^2 \quad (3.44)$$

is independent of a phase change of either wavefunction, that is, to substituting $\psi \rightarrow e^{i\Phi}\psi$ for any angle Φ . In particular one could arrange for different values of Φ to occur for different atoms; still the value would not change.

A state $S_{1/2}|F, M\rangle$ put in a constant electric field in the z direction acquires a shift in energy that for the hyperfine level $F = I + \frac{1}{2}$ may be written as

$$\Delta W = -\frac{1}{2}\alpha_0 E_z^2 + A_S M^2 E_z^2, \quad (3.45)$$

where α_0 and A_S (See Eq. 3.8) are independent of M , and where $\alpha_0 \gg A_S > 0$. If ψ is any coherent superposition of the states of this hyperfine level,

$$\psi = \sum_{M=-F}^F a_M |F, M\rangle, \quad (3.46)$$

then the effect of a time-dependent electric field in the z direction is to change the wavefunction to

$$\begin{aligned} \psi(t) \rightarrow & \exp\left(+\frac{1}{2}i\alpha_0 \int_0^t E_z^2(t') dt'\right) \\ & \times \sum_{M=-F}^F a_M \exp\left(-iA_S M^2 \int_0^t E_z^2(t') dt'\right) |F, M\rangle. \end{aligned} \quad (3.47)$$

The first, global phase

$$\exp\left(+\frac{1}{2}i\alpha_0 \int_0^t E_z^2(t') dt'\right) \quad (3.48)$$

has no effect on our observable; indeed it would not matter if different atoms acquired different global phases by passing through regions with different values of the integral $\int_0^t E_z^2(t') dt'$. The relative phases

$$\exp\left(-iA_S M^2 \int_0^t E_z^2(t') dt'\right), \quad (3.49)$$

that differentiate between states of different values of M , will change our observable; however we note that if we adjust the field-integral so that

$$A_S M^2 \int_0^t E_z^2(t') dt' \quad (3.50)$$

is an integer multiple of 2π , then the relative phases too will have no effect: except for an irrelevant global phase, any wavefunction becomes the same as if the electric field were zero throughout.

When F is odd, we have noted that the wavefunction for our initial state $\Pi(\theta)$ has, independent of the value of θ , amplitudes a_M that satisfy $a_M = 0$ for M even. Therefore, except for the irrelevant global phase, in an electric field this wavefunction becomes the same as if the electric field were zero throughout provided the value of the indicated integral is an integer multiple of π , not merely 2π . This is a useful property, and accordingly we assume that the electric field and the duration have been tuned so that

$$A_S M^2 \int_0^t E_z^2(t') dt' = k_\epsilon \pi \quad (3.51)$$

for some integer value of k_ϵ . (Our experiment will have $k_\epsilon \approx 66$.) As with the locking of the magnetic field phase φ_{mag} to $k_\beta\pi$, we can intuit that since a departure from $k_\epsilon\pi$ has the final state of the atom different from its initial state, it should be possible to measure that difference, and simply adjust the voltage applied to the electric field plates⁸ until that measured difference is zero, thus locking the electric field phase. It is not necessary to know what the electric field is everywhere in space. The details of how this measurement is done are in Section 5.6.

3.7.5 Zeroing of the $M = \pm 1$ Amplitude

When F is an even integer, after the rotation of a state $|F, M = 0\rangle$ by $\pi/2$ about the y axis to lie in the x - y plane, the amplitudes of the odd values of the M states are zero. Conversely when F is odd, after the rotation of $|F, M = 0\rangle$ by $\pi/2$ about the y axis to lie in the x - y plane, the amplitudes of being in an M state with an even value of M are zero, for example:

$$|4, 0\rangle \rightarrow \begin{pmatrix} \sqrt{70}/16 \\ 0 \\ -\sqrt{10}/8 \\ 0 \\ 3/8 \\ 0 \\ -\sqrt{10}/8 \\ 0 \\ \sqrt{70}/16 \end{pmatrix}, \quad |5, 0\rangle \rightarrow \begin{pmatrix} -3\sqrt{7}/16 \\ 0 \\ +\sqrt{35}/16 \\ 0 \\ -\sqrt{30}/16 \\ 0 \\ +\sqrt{30}/16 \\ 0 \\ -\sqrt{35}/16 \\ 0 \\ 3\sqrt{7}/16 \end{pmatrix}. \quad (3.52)$$

Therefore when F is even, there is zero amplitude for being in the states $|F, \pm 1\rangle$, while when F is

⁸The voltage on the electrostatic focusing triplet would also be changed to help maintain the fountain beam optics tune and the relative voltages on the individual electrostatic focusing elements might also be changed. Setting the phase advance and maintaining the fountain beam tune will likely be iterative, but the beam optics is designed to keep the tune stable, and once accomplished the settings need not be changed except to switch from k_ϵ even to k_ϵ odd and back for tuning to reduce systematic effects (Section 5.6).

odd, the amplitude for being in those states is finite.

We know from Section 3.5 and especially Table 3.2 that the $M = \pm 1$ states are subject to very large eigenvalue shifts (for $F = 5$ the eigenvalue shift in $M = \pm 1$ is a factor of 45 larger than for $M = \pm 3$). But other shifts also enter: in the absence of a magnetic field, states of the same $|M|$ are degenerate in energy, but only the states $M = \pm 1$ can be connected in second order by a magnetic field transverse to the z axis. For $|M| > 1$ however higher order effects are required and these are very small.

Francium isotopes ^{211}Fr and ^{221}Fr , and indeed all other EDM experiment-friendly francium isotopes, have for their upper ground-state hyperfine level a value of F that is odd. Cesium has F even. (Using francium's lower hyperfine level, which does have F even, complicates the optical pumping and the lower level generally has a smaller tensor polarizability.)

The key to eliminating these second-order errors in the experimentally important case of F odd is to note that the initial state used so far is

$$|F, 0\rangle = R_y(\pi/2)|F, 0\rangle; \quad (3.53)$$

in words, the state $|F, 0\rangle$ rotated by $\pi/2$ about the y axis.

Consider the result of rotating the state about the y axis by an additional small angle λ :

$$R_y(\pi/2)R_y(\lambda)|z, F0\rangle. \quad (3.54)$$

For certain values of λ , the amplitudes for the rotated state to be in the state $|F, 1\rangle$ or $|F, -1\rangle$ will both equal zero. For $F = 5$ the amplitude for being in the state $|5, 1\rangle$ computes to

$$-\frac{\sqrt{30}}{16}(21 \cos^4 \lambda - 28 \cos^2 \lambda + 8) \cos \lambda, \quad (3.55)$$

which is zero for $|\lambda|$ having the values

$$\begin{cases} \arccos\left(\frac{1}{21} \sqrt{294 + 42\sqrt{7}}\right) \approx 0.29 \text{ rad } (16.5^\circ) \\ \arccos\left(\frac{1}{21} \sqrt{294 - 42\sqrt{7}}\right) \approx 0.87 \text{ rad } (49.9^\circ) \end{cases} \quad (3.56)$$

Compared to using $\lambda = 0$, this rotation is less sensitive to a magnetic field or to an EDM signal by a global factor of $\cos \lambda$. (It is necessary to use the lasers' polarizations for both state preparation and analysis, rotated by the same angle λ , to avoid an additional loss in sensitivity.) For the two values of λ of Eq. (3.56) we have respectively

$$\begin{aligned}\cos(0.2892) &= 0.958 \\ \cos(0.8711) &= 0.644\end{aligned}\quad (3.57)$$

so by choosing to run at $\lambda = 0.29$ rad we can avoid the systematic errors associated with nonzero amplitudes for $M = \pm 1$ while losing only 4% of our sensitivity.

3.8 State Analysis

State analysis is performed on the descending atoms after they have left the electric field. State analysis is done at the same location as state preparation was done, for example by again optically pumping the $7^2S_{1/2}, F = 5 \leftrightarrow 7^2P_{3/2}, F' = 5$ transition. This is but one of several different methods to state prepare and analyze the ^{211}Fr atoms. For ^{221}Fr with $F = 3$, and for Cs with $F = 4$, further variations on these methods may be used (Appendix B.3).

Close to where $p(\theta)$ has its half-maximum (at $\theta = \pm 0.2114$ in Fig. 3.6), upwards of half of the atoms may be found in $|50\rangle$. The addition of a small magnetic field will change θ , and hence the fraction of atoms whose states project onto the $|50\rangle$ state. This constitutes the analysis. To get a signal that is zero when the magnetic field is zero, the difference between $p(\theta)$ and $p(-\theta)$ is used.

The fraction of atoms whose states project onto the $|50\rangle$ is measured by exciting the $7S_{1/2}, F = 5 \rightarrow 7P_{3/2}, F' = 5$ transition (labeled “a” in Fig. 3.5) with light that is linearly polarized with the axis of polarization parallel to the z axis. The $7s_{1/2}|50\rangle$ state is dark—it cannot be excited—and the probability an atom initially in that state remains in that state is therefore 1. Other states $|5M\rangle$ with $M \neq 0$ are excited by the laser; the subsequent spontaneous decay either: returns

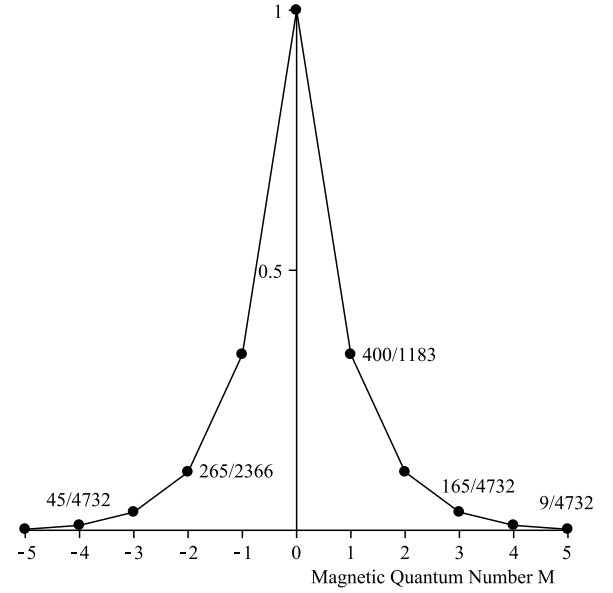


Figure 3.7: Probability that an atom initially in the state $7S_{1/2}, |5, M\rangle$ remains in the $F = 5$ hyperfine level when the illuminated with a laser tuned to the transition $7S_{1/2}, F = 5$ to $7P_{3/2}, F' = 5$ and that has linear polarization parallel to the z axis. Each probability depends only on Clebsch-Gordon coefficients.

the atom to the $7s_{1/2}, F = 5$ level where unless it drops into the dark state $|50\rangle$ it will excited again; or drops the atom into some state of the $7s_{1/2}, F = 4$ level. All the states in this level are dark (because the large ground-state hyperfine splitting makes the laser be off resonance with any transition, and because we do not otherwise repump the level).

The probability c_M as a function of M that an atom in an initial state $|5, M\rangle$ ends up in the $|50\rangle$ state, and therefore remains in the $F = 5$ hyperfine level, is plotted in Fig. 3.7. The probability decreases rapidly with increasing $|M|$ because an atom in an initial state $|5M\rangle$ has to survive multiple cycles of excitation and spontaneous emission back to the $F = 5$ level to drop into the $|50\rangle$ dark state. That we have $c_M > 0$ for $|M| > 0$ results in the small broadening of the central maximum of $p(\theta)$ shown in Fig. 3.8, compared to Fig. 3.6.

Once the atoms are sorted into $F = 4$ (mostly those that were not in $F = 5, M = 0$) and $F = 5$ (those

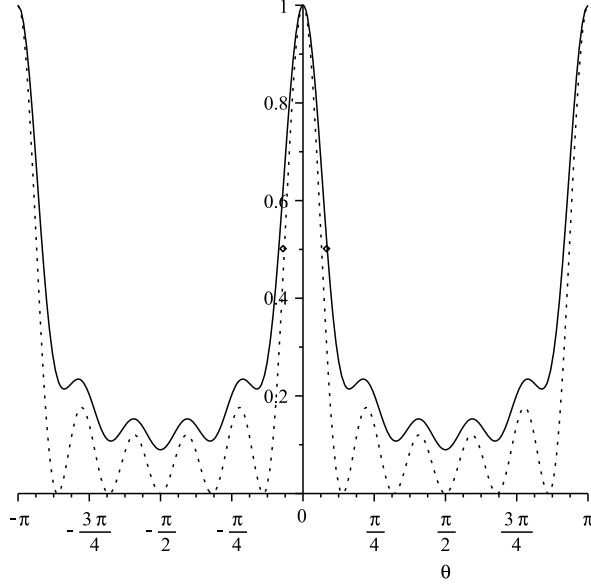


Figure 3.8: Change in the curve $p(\theta)$ due to transfer of $F = 5, M \neq 0$ into $F = 5, M = 0$. The broken line is for $c_M = 0$ for $M \neq 0$. The two points indicate the half-maxima of the curves.

that were in $M = 0$ plus those few that leaked into $F = 5, M = 0$ during optical pumping), the analysis is complete. Because the ratio of population of $F = 5$ to $F = 4$ is insensitive to laboratory electric and magnetic fields, the atoms can leave the magnetically shielded and nulled region and be detected at a more convenient location.

3.9 Atomic Magnetometer

We anticipate later work by stating that a sufficient condition for a measurement of an electron EDM at the level of 1.3×10^{-50} C m is to reduce along parts of the atomic trajectory the component in the vertical direction of any stray magnetic field to ≤ 200 fT⁹. A necessary condition is merely that in the ≈ 3 cm region between where the atoms experience the first rising of the electric field, the vertical component of stray magnetic field be ≤ 163 fT (this number may be adjusted upward

⁹With better shield demagnetization we expect to achieve ≤ 20 fT.

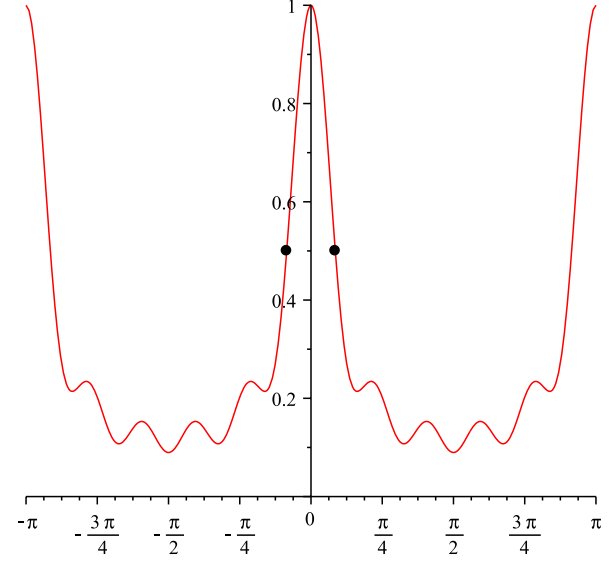


Figure 3.9: Plot of the probability an atom initially in the ^{211}Fr state $7S_{1/2}, |50\rangle$ remains in the $F = 5$ hyperfine level, instead of transferring to the lower, $F = 4$ hyperfine level, after illumination with a laser whose axis of linear polarization makes an angle θ with respect to the z axis, and that is tuned to the transition $7S_{1/2}, F = 5 \rightarrow 7P_{3/2}, F' = 5$. The locations of the full-width at half maximum of the central peak are shown as black dots where $|\theta| = 0.2678$ rad.

by small changes the electrostatic focusing lens design). Magnetic fields in some other locations can be an order of magnitude larger, subject to certain conditions being met for the integral of the magnetic field components seen by the atoms, as shown in Section 3.7.3.

We can turn the electric field off and measure the component of the magnetic field in any one of the cartesian directions with a statistical error of a few fT, by using the rising and falling atomic beam as a magnetometer. One such measurement takes four launches.

The basic idea of the magnetometer follows from computing the probability an atom will remain in the upper hyperfine level, when it is prepared in the state $|50\rangle$ using a laser whose axis of linear polarization is parallel to z but analyzed using a laser whose axis of linear polarization is in the x - z plane at a polar angle θ with respect to the positive z axis. This

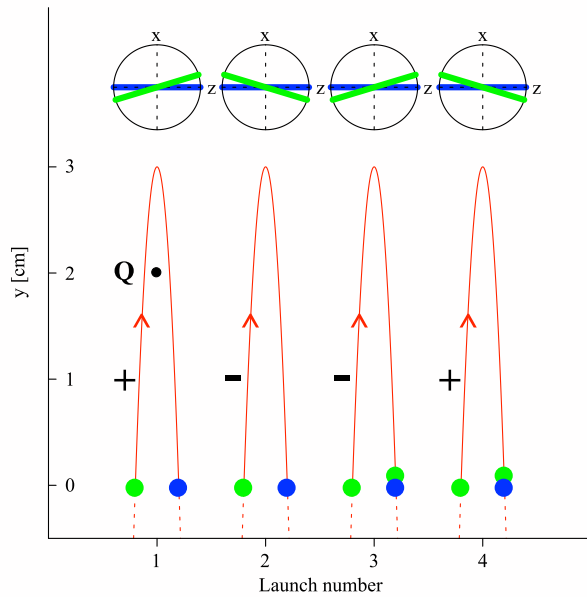


Figure 3.10: Measurement of vertical magnetic fields: Shown is the pattern of laser polarizations for vertically propagating laser beams that for four successive launches allow a measurement of the magnetic field in the vertical direction. The rise and fall of the atoms near apogee is indicated for each launch by a parabola; the magnetic field is measured at the point Q , which is 1 cm below apogee. In the circle above each launch is shown the orientation of the axis of linear polarization for state preparation (in green) and for state analysis (in blue); the location 3 cm below apogee where a laser pulse accomplishes state preparation or state analysis is shown by green and blue points, respectively. The sign, plus or minus, with which the data taken must be combined is shown for each pulse.

probability is plotted in Fig. 3.9. If a magnetic field is applied in the y (vertical) direction for a certain amount of time, the atomic state rotates by some small angle α , and the whole pattern shifts by α to the right; that shift will make the probability measured at some value θ on the slope of the principal peak go up, and the probability measured at the symmetric angle on the reverse slope go down; the difference is therefore a measure of α and hence of the time integral of the magnetic field.

The pattern of laser polarizations and the timing of the laser pulses to measure a magnetic field in the (most crucial) y direction at some point Q in space is shown in Fig. 3.10. The launch velocity

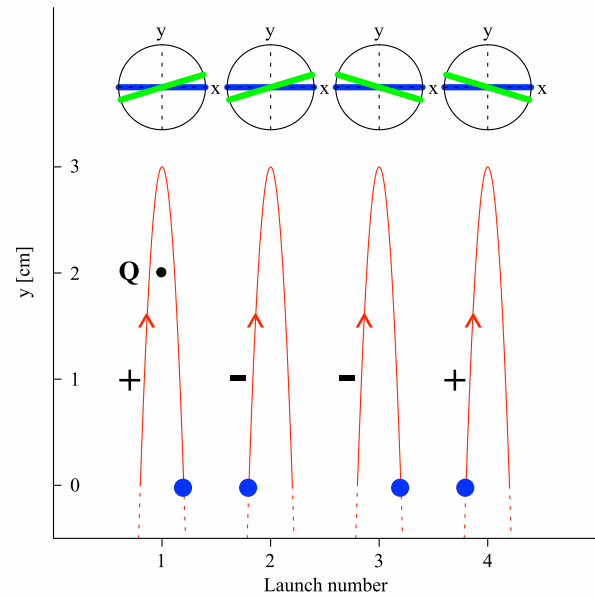


Figure 3.11: Measurement of transverse (horizontal) magnetic fields: Shown is the pattern of laser polarizations for four successive launches that allows a measurement of the magnetic field in the z direction. The rise and fall of the atoms near apogee is indicated for each launch by a parabola; the magnetic field is measured at the point Q , which is 1 cm below apogee. In the circle above each launch is shown the orientation of the axis of linear polarization for state preparation (in green) and for state analysis (in blue). State preparation is done with a laser that propagates horizontally in z and that intercepts the atomic beam below the electric field plates; state analysis is done with a laser that propagates vertically and is pulsed to intercept the atomic beam 3 cm below apogee at the locations shown by the blue points. The sign, plus or minus, with which the data taken must be combined is shown for each pulse. To measure magnetic fields in the x direction, transpose the role of x and z so that state preparation uses a laser that propagates in the x direction and state analysis is done with a laser that propagates vertically but is linearly polarized in the z direction.

of the atoms is to be adjusted so atoms rising and falling under gravity reach apogee 1 cm above Q . The lasers for preparation and analysis pulses are pulsed to intercept the atoms 2 cm below Q ; because the lasers propagate vertically, we can adjust the launch velocity and can time the laser pulses to measure at any point Q that we wish. With the electric field turned off there are no issues of defo-

cusing: the atoms can enter the interaction region at low velocity and turn around at any height.

The first two launches, launches 1 and 2 in Fig. 3.10, suffice to measure the magnetic field if the polarization of the lasers is perfect. Launches 3 and 4 contain a second state-preparation pulse that occurs as the atoms descend, just before state analysis; the difference between the result for launches 1 and 2, and the result for launches 3 and 4, subtracts any contribution from imperfect polarization for the preparation and analysis lasers (and any contribution from birefringence in the vacuum windows). Because the second state preparation pulse in launches 3 and 4 occurs immediately before the state analysis pulse, there is little time for the cloud of atoms to expand from the additional heating of the second state preparation pulse, and the cloud will therefore be the same size as for launches 1 and 2.

The patterns of laser polarizations and launches that measure fields in the x or z directions, shown in Fig. 3.11, are different because the state preparation laser does not propagate vertically but horizontally. The statistical errors are the same as for magnetic field measurement in the y direction.

If the vertically traveling lasers are timed to prepare the state at a position $y = 0$ in Fig. 3.10, and to analyze the state after it falls back to $y = 0$, what is measured is the rotation of the atomic system about the y axis above the position $y = 0$; if the atom reaches apogee at a height Y , then the net rotation angle is

$$2\left(\frac{g_f\mu_B}{\hbar}\right)\sqrt{\frac{2Y}{g}} \times \int_0^Y \frac{B(y)}{2\sqrt{Y(Y-y)}} dy, \quad (3.58)$$

where g is the acceleration due to gravity. This rotation angle closely measures the value of the magnetic field in the y direction at a height $y_0 = 2Y/3$, since

$$\begin{aligned} \int_0^Y \frac{B(y)}{2\sqrt{Y(Y-y)}} dy \\ = B(y_0) + 0 \times B'(y_0) + \frac{2}{45} Y^2 B''(y_0) + \dots \end{aligned} \quad (3.59)$$

Any systematic error in the value of the field at point Q due to a magnetic field gradient cancels. Error due to quadratic variations in the field will (under the conditions we anticipate in our apparatus) contribute at the level of a few percent.

If the time between state preparation and analysis is t , the statistical error in the measurement of the field is

$$\sigma_{B_z} = c \times \frac{\hbar}{2|\mu_e|t} \frac{1}{\sqrt{N_{\text{launch}}}}. \quad (3.60)$$

Here c is a constant of the rough order of unity that accounts for the increasing inefficiency (Section 3.8) of such a system with increasing atomic spin F ; the constant is unity for an ideal system of spin $1/2$. For ^{211}Fr we have $c = 2.05$. Here also μ_e is the electron magnetic moment, and t is the time between state preparation and analysis, and N_{launch} is the number of atoms in a single launch. For ^{211}Fr for the stated conditions and for $N_{\text{launch}} = 6.4 \times 10^8$, the statistical error in the measurement of the y component of the magnetic fields at Q is

$$\begin{aligned} \sigma_{B_z} &= 2.05 \\ &\times \frac{1.056 \cdot 10^{-34} \text{ J s}}{2 \times |9.27 \times 10^{-24} \text{ J/T}| \times 0.1566 \text{ s}} \\ &\times \frac{1}{\sqrt{6.4 \times 10^8}} = 2.9 \text{ fT}, \end{aligned} \quad (3.61)$$

for less than one minute of measurement.

3.10 Detection

3.10.1 Overview of Detection

Detection of the atoms remaining in the $7^2S_{1/2}, F = 5$ state is done using circularly polarized light to excite the cycling transition (labeled “ c ” in Fig. 3.5) from which the intensity of the fluorescence radiation $7^2S_{1/2}, F = 5 \leftrightarrow 7^2P_{3/2}, F' = 6$ is measured. The circular polarization helps prevent accidental transitions that could transfer the atoms to $7^2S_{1/2}, F = 4$ due to excitation of the Lorentz tail of P transitions with $F' = F$ [BHL⁺06, Bon99,

Mun07a]. Finally the atoms in the $7^2S_{1/2}, F = 4$ are repumped back into the $F = 5$ level by excitation to the $7^2P_{3/2}, F' = 5$ and the detection process is repeated. The ratio of the intensities gives the probability an atom in the beam was initially in the $F = 5$ level.

It is necessary use anti-propagating beams of equal intensity so that no net momentum is transferred to the atoms by photon absorption; and to tune the laser somewhat below resonance to minimize changes in the rate of scattered photons due to the Doppler shifts caused by the gradual heating of the atoms [BHL⁺06, Mun07a]; and to reduce the overall heating by using the mechanism of laser cooling.

Detection requires only measuring the relative populations in the two ground state hyperfine levels without regard to their distribution over states of different M . There is very little that can affect the populations of atoms in atomic hyperfine levels separated, as they are in ^{211}Fr , by 44 GHz. Magnetic shielding is not needed and detection is done below the state preparation and analysis region and outside of the magnetic shielding, as shown in Fig 3.2. This allows the detector, typically a photomultiplier, to be placed close to the beam and keeps photomultiplier magnetic material and magnetic fields due to detection currents outside of the interaction region. Because each atom can fluoresce thousands of photons, photon collection optics with even a modest light collection efficiency will oversample the atoms.

Table 3.4: Atomic data for ^{211}Fr cycling transition $7S_{1/2}, F = 5 \rightarrow 7P_{3/2}, F' = 6$

wavelength λ	$7.183 \times 10^{-7} \text{ m}$
frequency ν	$4.174 \times 10^{14} \text{ Hz}$
$7P_{3/2}$ lifetime	$2.10 \times 10^{-8} \text{ s}$
$7P_{3/2}$ decay rate Γ	$4.76 \times 10^7 \text{ s}^{-1}$
$7P_{3/2}$ linewidth (FWHM) ν_w	$7.58 \times 10^6 \text{ Hz}$
one-photon recoil velocity v_r	$2.64 \times 10^{-3} \text{ m/s}$
one-photon recoil shift ν_r	$3.67 \times 10^3 \text{ Hz}$
Laser detuning $ \Delta = \Gamma\sqrt{3}/6$	$1.37 \times 10^7 \text{ Hz}$
Saturation intensity I_{sat}	$2.67 \times 10^1 \text{ W/m}^2$

Atomic data for the cycling transition $7S_{1/2}, F =$

$5 \rightarrow 7P_{3/2}, F' = 6$ (labeled “c” in Fig. 3.5) in ^{211}Fr may be found in Table 3.4.

3.10.2 Transmission of Photons Out of the Vacuum System

The detection system is shown in Fig. 3.12. In this section we use beam optics coordinates shown in Fig. 3.1 (b): z is the vertical direction of francium atom travel, and x and y are horizontal and form a right-handed system, with the y axis parallel to the electric fields applied by the main electric field plates.

An elliptical cloud of atoms longer than it is wide falls through four locations where the atoms in the cloud pass through a laser spot. The lasers are

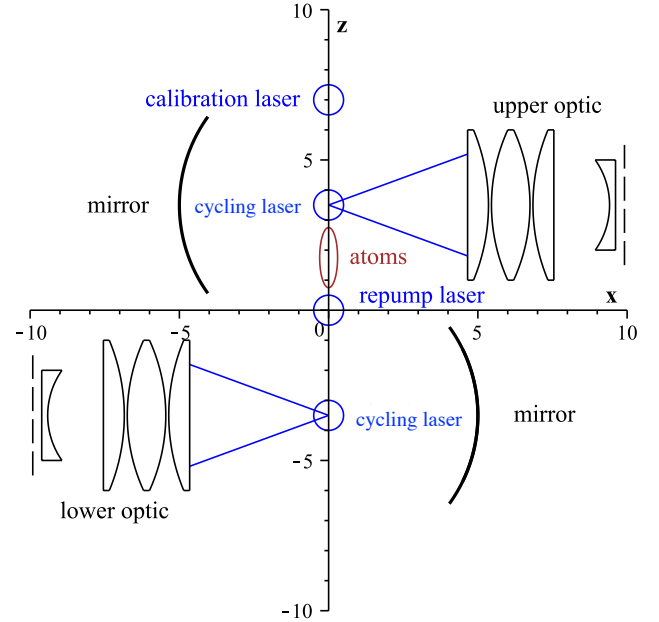


Figure 3.12: Cross section view of the fluorescence detection region. In two regions combination of a spherical mirror and a unit-magnification optic symmetric optic (the first half of which is shown) collects photons scattered from the atoms as they pass through a laser spot (“cycling laser”) that excites the cycling transition. At two other locations, marked “calibration laser” and “repump laser” the atoms may pass through a laser to adjust their atomic state. A window between the atoms and the optic is not shown. Dimensions in centimeters.

turned on just before the cloud enters a laser spot, and off again just after it exits. At all four locations lasers both propagate and anti-propagate (as if retroreflected) so that absorption and emission of photons imparts no net momentum to the beam.

In Fig. 3.12, two points, marked “calibration laser” and “repump laser” allow for adjusting the atomic state of the atoms by the scatter of so few photons that there is negligible heating. At two other points, marked “cycling laser,” the cycling transition $7S_{1/2}, F = 5 \rightarrow 7P_{3/2}, F' = 6$ is excited; at these points significant heating of the beam occurs. The photons scattered as the atoms pass through either “cycling laser” location are collected by a spherical mirror and an optic (the first half of which is shown in Fig. 3.12) and counted to generate a signal proportional to the number of atoms that enter the laser spot while in the upper ground-state hyperfine level $7S_{1/2}, F = 5$. Some basic design parameters for the fluorescence region may be found in Table 3.5.

Table 3.5: Detection System Design Parameters

Quantity	Gap
fluorescence laser beam waist w_0	3.0 mm
fluorescence regions vert. separation	7.0 cm
transverse beam radius ^a	2.8 mm
beam bunch length ^a	1.5 cm
descending velocity of the beam	5.5 m/s

(a) 90% containment

The first and simplest task is to design a collection system that will count at least several photons from each atom in the falling cloud.

A suitable device to count the photons from fluorescence is the Hamamatsu R943-02 photomultiplier tube [hama], kept in the standard Hamamatsu thermoelectric cooler [hamb] to reduce the dark rate¹⁰ from $\sim 4 \cdot 10^4$ Hz at 20 °C to about 20 Hz

¹⁰The dark count rate of the R943-02 [hama] at 20 °C is typically $4 \cdot 10^4 \text{ s}^{-1}$, and so in a counting interval of $1 \cdot 10^{-4} \text{ s}$ one would record ~ 4 counts. This would be a significant fraction of the ~ 20 total counts we would expect in that time for a single atom, but would be a negligible fraction of the signal expected from a cloud of $\sim 10^6$ atoms; however for the purposes of design we include the (modest) extra solid

at about -20 °C.

The quantum efficiency of the R943-02 photocathode¹¹ at 718 nm is 0.12.

The Hamamatsu tube has a square photocathode 10 mm on a side, with its center 19 mm behind the front face of the glass tube. The clear diameter of that tube is 22 mm, which would limit the half-angle of the cone of rays that could be collected at the center of the photocathode to 30 degrees; however there are internal structures with a clear diameter of 11.5 mm that lie somewhat closer to the photocathode that limit the half-angle in practice to 24 degrees; when installed in the thermoelectric cooler, the half-angle for acceptance narrows further to 21 degrees. The acceptance of the tube will therefore match a source that has roughly a 6 mm diameter, which we have assumed, and an angular distribution with a half-angle of 20 degrees. Photons from the cloud that are directed in a 20 degree cone opposite the collection optic are redirected using a gold-coated spherical mirror.

We image this cloud of atoms onto the photocathode using the unit-magnification optical periscope whose lens layout is shown in Fig. 3.13. The locations and radii of curvature of the various lens surfaces for the first half of the (symmetric) periscope are listed in Table 3.6. Another unit-magnification optic more complicated than this has already been built and used in the proof-of-principle experiment [AMG07, Ami06] on cesium; a photograph is shown in Fig. 3.14.

The lenses in this design are stock Melles-Griot catalog lenses of standard BK7 glass. We deal with monochromatic light, so of the seven classic third-order Seidel aberrations, two (chromatic aberrations) are automatically zero, leaving five to deal with. In any inversion symmetric optical system

angle restrictions that come using the cooler. The dark count rate of the tube falls to $\sim 10^3 \text{ s}^{-1}$ at 0 °C, to $\sim 2.0 \cdot 10^1 \text{ s}^{-1}$ at -20 °C and to $\sim 4 \text{ s}^{-1}$ at -30 °C, which is the lowest operating point of the cooler.

¹¹A charge-coupled device such as the Hamamatsu ORCA-R2 [hamc] can achieve a higher quantum efficiency of 0.45 at 718 nm when operated in “Low light mode” over a photocathode of essentially equivalent area; however the noise injected by the readout amplifier built into the chip removes most of the advantage for mere photon counting of the higher quantum efficiency.

Oslo unit-magnification symmetric design

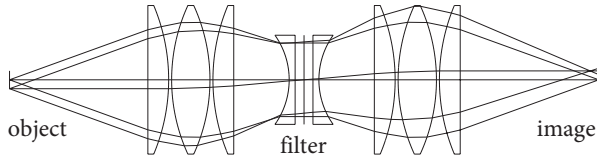


Figure 3.13: Cross sectional diagram of the lens layout of the unit-magnification optical periscope with a numerical aperture of 0.342. Cancellation of spherical aberration allows a high-quality image to be transmitted despite the use of stock spherical-surface lenses and rays that deviate from horizontal by 20 degrees. Shown are the envelopes of rays that originate from the object center and from a point lowered 3 mm. The diameter of the largest lens in the system is 25.0 mm and the distance from object to image is 190.2 mm.

Table 3.6: Lenses and lens locations (mm) for first half of a unit-magnification optical periscope with a numerical aperture of 0.342.

surface	gap	R [mm]
object	0.000	—
1	45.556	0.000
2	7.000	−64.800
3	1.000	60.000
4	12.900	−60.000
5	1.000	64.800
6	7.000	0.000
7	18.660	−25.900
8	2.000	0.000

two of these five (distortion and coma) necessarily cancel. This fact is used to eliminate these aberrations in the design overall; it is also used in that each triplet of two planoconvex lenses and one biconvex lens is itself inversion symmetric about its center and the light path through each triplet is nearly an inversion symmetric path, so neither distortion nor coma are ever very large at any location in the lens system; as it happens, in these triplets a lot of other aberrations, while nonzero, tend to be small.

That leaves four parameters of the system to control: the third-order errors of spherical aberration, astigmatism, and pincushion distortion; and the



Figure 3.14: Photograph of the unit magnification optical periscope used in Ref. [AMG07, Ami06].

overall scale of the optic. There are four parameters that are easily adjusted in the design: the radius of curvature of the planoconvex lens; the radius of curvature of the (symmetric) biconvex lens; the radius of curvature of the planoconcave lens; and the separation between the triplet and the planoconvex lens (changing the thickness of the various lenses does rather little). Using the optical code OSLOTM [osl] it is straightforward to solve for values of the parameters that zero the three third-order errors for a given scale of the optic.

One then chooses those catalog lenses whose properties are close to the solution found; and then adjusts the separation of the triplet and the planoconcave lens to zero not the third-order spherical aberration, but a general sum of third, fifth, and seventh order spherical aberrations, letting the astigmatism and pincushion distortion depart weakly from zero. The resulting optic gathers light over a numerical aperture of 0.342 (a cone of half-angle 20 degrees); even at full aperture, the image of a point source has a diameter of only 40 μm .

At the symmetry point of the optic, between the two planoconcave lenses, is a gap in which we insert an interference filter to cut out ambient light. The rays in the gap coming from the center of the object are

Table 3.7: Optical System Efficiency

Fraction of 4π solid angle transmitted	0.0603
Efficiency due to anisotropic angular distribution	> 0.750
Average reflectance ^a at 718 nm with Au-coated mirror	0.995
Vacuum window efficiency (reflectance loss) ^b	$(0.995)^2 = 0.990$
Air-glass interface efficiency in lenses ^c	$(0.995)^{16} = 0.923$
Transmission of a ≈ 10 nm bandpass filter ^d at 720 nm	0.59
Refrigerator window efficiency ^e	0.85
Uncoated PMT air-glass-vacuum interface efficiency	$(0.96)^2 = 0.922$
Quantum efficiency of the photocathode ^f	0.12
Net photoelectrons per emitted photon	0.00228

(a) Half the photons take one bounce, and half none.

(b) Standard MgF_2 “V” antireflection coating.

(c) Standard Melles-Griot “Hebbar” antireflection coating.

(d) Thorlabs FL720-10.

(e) Uncoated silica double window; anti-reflection coatings could be applied.

(f) Hamamatsu R943-02 at 718 nm.

nominally parallel; rays from a point 3 mm below the object center are inclined at 4.6° relative to the optical axis. The effect of tipping a ray relative to the normal to an interference filter is (roughly) to leave the width of the passband unchanged, but to shift its center to the blue; the formula for the shift in center wavelength of a filter whose nominal center wavelength is λ_0 is [fil]

$$\lambda_0 \left(1 - \left[1 - \left(\frac{\sin \theta}{n_{\text{eff}}} \right)^2 \right]^{1/2} \right), \quad (3.62)$$

where n_{eff} is an effective index of refraction that depends on the polarization of the light; typical values of n_{eff} range from 1.62 to 2.08. The smaller value gives the largest shift; for $\theta = 4.6^\circ$ and $\lambda_0 = 718$ nm the shift is 0.88 nm, which is negligible for an interference filter with a standard 10 nm passband¹².

Use of a periscope with a center where the rays are nearly parallel has several advantages:

1. For the desired numerical aperture of 0.342 the rays barely exceed the 21 mm clear diameter of a standard interference filter, while the angular range of the rays is small enough to pass through the filter despite the tuning of the filter toward the blue.
2. The radiation emitted from the atoms normal to the laser beam is linearly polarized, while the exciting laser is circularly polarized. The center allows the option of using a linear polarizer [New] to try to improve the ratio of photons emitted from the atoms to those scattered from the laser by a factor of 2.
3. At the places between either doublet of converging lenses, the rays from the image are nearly parallel, and rays from a “hot spot” on the spherical mirror will pass through a particular point on the plane. The noise from such a hot spot can therefore be easily blocked with a suitable mask.

¹²The use of a laser line filter [nar] would offer a passband that is appreciably smaller with (on paper) a higher transmission at the laser wavelength ($\sim 90\%$ in some cases). Such a filter centered at any wavelength from 720 nm to 780 nm loses its high blocking ability (optical density 6) outside a 200 nm band centered at the laser wavelength; to block the visible spectrum requires extra layers, which reduce the transmission to the that characteristic of a high-quality interference filter.

In Table 3.7 we list the individual and cumulative losses for the optical system; for each photon scattered from the laser the probability of getting a count from the multiplier is greater than 2.3×10^{-3} . Care has been taken to estimate the cumulative losses at vacuum-glass and air-glass interfaces. A multilayer “V” coating [rai] of MgF_2 on a fused sil-

ica substrate can at a single laser frequency achieve a reflectance loss of 0.1% at an angle of incidence of 0° , rising to but 0.75% at an angle of incidence of 45° . In the design where the angle of incidence is never more than 20° we have conservatively assumed an reflectance loss averaged over all angles of incidence of 0.5% for all coatings¹³, though here there is scope for improvement [Mel].

3.10.3 Photons Detected Per Atom Illuminated

A transition $S_{1/2}, F \rightarrow P_{3/2}, F' = F+1$ illuminated by a single, helicity positive laser settles into the cycling transition $S|FF\rangle \rightarrow P|F+1, F+1\rangle$; the rate of photon scatter, R_{sc} , is [Str]

$$R_{sc} = \frac{\Gamma}{2} \frac{I/I_{sat}}{1 + 4(\Delta/\Gamma)^2 + I/I_{sat}}, \quad (3.63)$$

where Γ is the total decay rate of the P state and Δ is the departure (in Hz) of the laser frequency from resonance, with negative Δ indicating that the laser is tuned below resonance. The intensity (power per unit area) of the laser incident on the atom is I , and a convenient scale is the saturation intensity

$$I_{sat} = \frac{\hbar\omega^3\Gamma}{12\pi c^2}, \quad (3.64)$$

where ω is the angular frequency of the transition $P_{3/2}, F' \rightarrow S_{1/2}, F$. For ^{211}Fr we have $I_{sat} = 2.67 \text{ mW/cm}^2$.

The quantity Δ is the amount the laser is tuned off of resonance; to cancel [Mun07a] the leading shift in the scatter rate due to heating of the atomic beam we shall shortly show we wish to have $\Delta/\Gamma = \sqrt{3}/6 = 0.289$. Thus for $I = I_{sat}$ and $\Delta/\Gamma = \sqrt{3}/6$ we have for ^{211}Fr a scatter rate of

$$\begin{aligned} R_{sc} &= \frac{4.76 \times 10^7 \text{ s}^{-1}}{2} \frac{1}{1 + 4(\sqrt{3}/6)^2 + 1} \\ &= 1.02 \times 10^7 \text{ s}^{-1}. \end{aligned} \quad (3.65)$$

¹³A Melles-Griot “Hebbar” coating has a reflectance at the Fr cycling transition wavelength of 718 nm of roughly 0.4%, and at the Rb cycling transition wavelength of 780 nm of roughly 0.25%, though a smaller figure (0.1%) at each wavelength may be achieved with care.

By increasing the laser intensity past I_{sat} the rate could be increased about a factor of 2 or so, towards the limiting value of $2.28 \times 10^7 \text{ s}^{-1}$, but we shall not rely upon doing this for the present set of estimates.

If an atom scattering photons is observed for 1.09 ms, which is the time for an atom falling at 5.5 m/s to fall through twice our nominal laser radius of 3 mm, then the number of scattered photons would be

$$1.02 \times 10^7 \text{ s}^{-1} \times 1.09 \times 10^{-3} \text{ s} = 1.11 \times 10^4. \quad (3.66)$$

With the given number of photoelectrons per emitted photon, the number of photoelectrons would be

$$1.16 \times 10^4 \times 2.28 \times 10^{-3} = 25.4. \quad (3.67)$$

We therefore have considerable margin to lose photons and still achieve several photoelectrons per illuminated atom, so that photon counting statistics will contribute negligibly to the shot noise. We note that Ref. [BHL⁺06] achieved about 20 photoelectrons per atom with the same photomultiplier tube when fluorescing rubidium, and so this estimate is consistent with what has previously been achieved.

These computations are for a laser that propagates in one direction; it is desirable to illuminate the atom with equal-intensity lasers that propagate in opposite directions. This geometry introduces some technical complications into the calculation of the fluorescence rate. A beam of intensity I when retroreflected produces a one-dimensional intensity grating with a spatial period of $\lambda/2$ and whose maximum intensity is $4I$ and whose minimum intensity is zero, explicitly

$$I(z) = 4I \cos^2(\pi z/\lambda), \quad (3.68)$$

where z is distance along the laser axis. While it is possible that an atom might fall vertically through the entire laser beam and remain at a node where the excitation probability is zero, this is exceedingly unlikely in practice. The period of a grating with a wavelength of 718 nm is 359 nm; the separation between an intensity minimum and an intensity maximum is half that, or 180 nm. We will suppose the

laser is round with a beam waist w_0 of 3 mm; if the laser has a vertical width of $2w_0 = 6$ mm the angle an atom that passes from minimum to maximum intensity as it crosses the laser beam deviates from perpendicular by but

$$\frac{180 \times 10^{-9} \text{ m}}{6.0 \times 10^{-3} \text{ m}} = 2.99 \times 10^{-5} \text{ radian} . \quad (3.69)$$

The recoil velocity imparted to an atom of ^{211}Fr by the emission of a single cycling photon is 2.64 mm/s; an atom with this velocity parallel to the laser beam is inclined with respect to the grating by an angle that is greater than

$$\frac{2.64 \times 10^{-3} \text{ m/s}}{5.5 \text{ m/s}} = 4.80 \times 10^{-4} \text{ radian} . \quad (3.70)$$

The ratio of the two angles is $2.99 \times 10^{-5} / 4.80 \times 10^{-4} = 0.0623$.

The heating of the beam by state preparation heats the beam to have a root-mean-square momentum in the direction of propagation of the fluorescence laser of many multiples of the recoil velocity from a single photon, so the chance an atom misses an intensity maximum and so avoids being fluoresced is negligible. When doing state preparation on ^{211}Fr using optical pumping, an essential first step is preparing a state $S_{1/2} |50\rangle$ from the output of the magneto-optic trap, which is an ensemble of atoms that is an incoherent mixture of all states in the $S_{1/2} F = 5$ level. Even if the output of the trap were unphysically supposed to be at zero temperature, the root-mean-square value of the velocity parallel to the preparation beam is a multiple of the recoil velocity that has been calculated [Mun07a] to be at least $\sqrt{13.5} = 3.67$, so the ratio of the angle spanned by the grating to the root-mean-square angle would be at least $\sim 0.0623/3.67 \approx 0.017$.

This ratio is so small that it is appropriate to assume that a typical atom will, as it falls, cut across many intensity maxima and minima. The time spent at an intensity maximum will tend to be slightly less than the time spent at an intensity minimum, because the atoms scatter and so speed up at a maximum whereas they maintain a constant velocity near a minimum, but this effect is surely minute. Consequently for a retroreflected

laser whose one-way intensity is I , the rate of photon scatter for a typical atom is the rate averaged over the position of atoms along the laser axis, and so changes from R_{sc} to

$$R_{\text{av}} = \frac{2}{\lambda} \int_0^{\lambda/2} \frac{\Gamma}{2} \frac{I(z)/I_{\text{sat}}}{1 + 4(\Delta/\Gamma)^2 + I(z)/I_{\text{sat}}} dz . \quad (3.71)$$

As one would expect, the fluorescence rate is somewhat higher for a laser of intensity I that is retroreflected than for a single laser of the same intensity; numerically this is not a big effect; for $I \ll I_{\text{sat}}$ the number of scattered photons increases by a factor of 2. We do not include the possibility of this increase in our estimates.

The remaining problem is to reduce the number of counts from light scattered from the laser that transits the vacuum cavity. A ratio of signal to noise of 4.5:1 was achieved in Ref. [BHL⁺06] for the signal from a *single atom*; given that we will have $\sim 10^6$ atoms, the ratio of genuine counts from atoms to counts from scattered laser light is, on paper, that same factor $\sim 10^6$ greater, so getting a high signal-to-noise ratio is certainly a solvable problem. We note however that these same authors found that the signal to noise degraded [Bon99] when a retroreflected, instead of single-pass, laser beam was employed, and we certainly wish to use both a propagating and an anti-propagating laser; so we will have to exercise some care.

The first task is to ensure that we have adequate internal clearance for the passage of a laser beam with a waist sufficient to cover our atomic cloud. A standard Gaussian laser [Gau] with a beam waist of w_0 and with a center intensity (power per unit area) of I_0 will have a number of photons per unit time that appear at radii $r > R$, for any circular aperture of radius R ; that number per unit time is

$$\frac{\lambda}{hc} \frac{\pi w_0^2 I_0}{2} e^{-2R^2/w_0^2} . \quad (3.72)$$

Even if an effort were made to double the number of photons counted per atom to set up two optical periscopes per fluorescence region, even then the nearest approach of the edge of a lens or of the required spherical mirror opposite would be more than 28 mm. Let us assume very pessimistically that every photon from the laser that scrapes

against the edge of a circular aperture of radius $R = 28$ mm has the same chance of reaching the photomultiplier tube as a photon emitted from an atom at the focus of the spherical mirror; and suppose we desire the count rate from photons scattered to equal a factor $1/100$ times the rate of $1.02 \times 10^7 \text{ s}^{-1}$ from a *single atom*. We could nonetheless afford to have a beam waist with $w_0 \leq 7.88$ mm, which is much larger than the ~ 2 mm effective radius we have assumed for our atomic cloud, and also much larger than the ~ 3 mm beam waist that we have chosen to rough out a design.

Light will inevitably scatter from dirt or flaws in the windows themselves. We will examine the scope of this problem by constructing prototypes; on general principles, we will put these potential light sources at some distance by mounting the windows at the ends of arms such that the window separation is ≈ 1 m. What light that still scatters within the vacuum chamber will be attenuated by coating inside surfaces with a UHV-compatible but black coating, such as diamond-like-carbon [KBC⁺08], which can be discharge-applied even to awkward surfaces, like to the inside of narrow tubes. We will also as needed insert apertures and light-traps so that light from the windows can reach the spherical mirror's inner surface, and so scatter to reach the photomultiplier, only after multiple bounces off of nominally black objects. Because this whole assembly is outside the magnetic shielding (Fig. 3.2), there is considerable latitude to add whatever pumps, coatings, and hardware is needed.

If the laser light were to exit and enter the chamber through parallel flat windows, and even were these windows flawless and perfectly clean, still beam that reflected several times from the windows would “walk” out to large radii; in other language, the optical cavity formed by two parallel surfaces flat surfaces is unstable, and it gets more unstable if the surfaces aren't in fact parallel. While the windows will be anti-reflection coated at the laser wavelength¹⁴, and so the intensity of a beam re-

flected multiple times will be weak, still the photons that appear at large radii from the main laser beam are a potential problem. The extent of this potential problem will be determined using a prototype; if significant, this problem can be avoided by using windows that consist of two parallel spherical surfaces of equal radii r , chosen such that all the cavities formed by reflecting surfaces, whether spherical mirrors bounding the laser cavity itself or the window surfaces within it, are stable. One such configuration is to have the retroreflected laser operate in a confocal cavity of length $L = 2$ m and so between mirrors of radius $R = L$, and have the vacuum windows located symmetrically at ± 0.5 m with surfaces of radius $r \geq 3L/4$. A radius $r \approx L$ would probably prove close to optimum.

It is necessary that the atoms be fluoresced using a propagating and an anti-propagating beam of equal intensity. If a single beam was used, then the absorption of each photon would move an atom off of resonance by 3.67 kHz; if the intended 1.11×10^4 photons were scattered, the cumulative shift would be

$$3.67 \text{ kHz} \times 1.11 \times 10^4 = 4.08 \times 10^7 \text{ Hz} . \quad (3.73)$$

This would exceed the linewidth of $\nu_w = 7.58 \times 10^6 \text{ Hz}$ of the francium $7P_{3/2}$ state by a factor of 5.4. The atom would walk completely off-resonance if the laser were not ramped in frequency. Even if the frequency were ramped, the cumulative recoil velocity in the direction of the laser would be

$$2.64 \times 10^{-3} \text{ m/s} \times 1.11 \times 10^4 = 29.4 \text{ m/s} , \quad (3.74)$$

which would exceed even the atoms' original downward speed of 5.5 m/s by a factor of 5.3: the beam would be kicked so hard it would never enter the laser spot in the lower fluorescence region.

In contrast if the transition is excited with equal-intensity, anti-propagating beams, then there is no shift in recoil velocity or Doppler shift that is linear in the number of photons scattered. There is a gradual growth in the expectation value of the square of each component of the atom's momentum. If we imagine the transverse temperature of the beam to be zero before fluorescence, and if we let the fluorescence lasers propagate parallel to the x axis, then

¹⁴A fused silica viewport on a standard ConflatTM flange can be anti-reflection coated with a standard “V” coating of MgF_2 , to have a reflectance of 0.25% and still be baked to 200 °C. See for example <http://mpfpi.com/stock-products/viewports.aspx>.

absent some mechanism to cool the atomic beam we have for the cycling transition [Mun07a]

$$\begin{aligned} \frac{d\langle p_y^2 \rangle}{dt} &= p^2 \left(\frac{\Gamma}{2} \right) \left[\frac{3}{10} \frac{I/I_{\text{sat}}}{1 + 4(\Delta/\Gamma)^2 + I/I_{\text{sat}}} \right] = \frac{d\langle p_z^2 \rangle}{dt} \\ \frac{d\langle p_x^2 \rangle}{dt} &= p^2 \left(\frac{\Gamma}{2} \right) \left[\frac{7}{5} \frac{I/I_{\text{sat}}}{1 + 4(\Delta/\Gamma)^2 + I/I_{\text{sat}}} \right. \\ &\quad \left. + 2 \left(\frac{I/I_{\text{sat}}}{1 + 4(\Delta/\Gamma)^2} \right)^2 \right]. \end{aligned} \quad (3.75)$$

Here p is the magnitude momentum transfer due to the absorption of one photon. The components of atomic momentum transverse to the lasers grow only due to spontaneous emission. The component parallel to the lasers grows due to spontaneous emission, and due to the absorption of a photon before a spontaneous emission, and due to the absorption of one photon from one laser and the stimulated emission of a photon into the other laser.

If the beam in the upper fluorescence region was a point, zero-temperature cloud, then after fluorescing 1.11×10^4 photons from a laser running in the upper fluorescence region horizontally and parallel to x , the velocity distributions would be

$$\begin{aligned} \langle v_y^2 \rangle^{1/2} &= \langle v_z^2 \rangle^{1/2} = 0.153 \text{ m/s} \\ \langle v_x^2 \rangle^{1/2} &= 0.558 \text{ m/s}; \end{aligned} \quad (3.76)$$

and after falling 7 cm at a speed of 5.5 m/s into the lower fluorescence region even an initially point beam would acquire a finite transverse spatial distribution with root-mean-square distributions of

$$\begin{aligned} \langle y^2 \rangle^{1/2} &= \langle z^2 \rangle^{1/2} = 1.94 \text{ mm} \\ \langle x^2 \rangle^{1/2} &= 7.11 \text{ mm}. \end{aligned} \quad (3.77)$$

In particular the growth in the x direction, parallel to the fluorescing laser beam, would exceed the nominal ± 3 mm of the field of view of the optical periscope in the transverse direction.

The velocity distribution of the beam in the direction parallel to the fluorescing lasers does not grow as much as this because the lasers are tuned below resonance and Doppler cooling occurs. The kinetic temperature of the atomic beam in the direction

parallel to the lasers would increase from zero but have an upper bound set by [MvdS99b]

$$T(\Delta) = T_D \frac{1}{2} \left(\frac{2\Delta}{\Gamma} + \frac{\Gamma}{2\Delta} \right), \quad (3.78)$$

where T_D is the Doppler temperature defined by

$$T_D = \frac{1}{2} \frac{\hbar \Gamma}{k_B}. \quad (3.79)$$

Here Γ is the total decay rate of the $7P_{3/2}$ state and k_B is Boltzmann's constant. For the transition $7P_{3/2} \rightarrow 7S_{1/2}$ we have

$$T_D = 1.82 \times 10^{-4} \text{ }^\circ\text{K}. \quad (3.80)$$

At the Doppler temperature the velocity parallel to the beam equilibrates such that

$$\langle v_x^2 \rangle^{1/2} \leq 0.0847 \text{ m/s}, \quad (3.81)$$

and so the actual growth in the beam size in the lower region would limit to

$$\langle x^2 \rangle^{1/2} \leq 1.08 \text{ mm}, \quad (3.82)$$

which would be acceptable.

It may be objected that the Doppler temperature applies to lasers tuned with $|\Delta/\Gamma| = 1/2$, while to raise the fluorescence rate and to compensate for changes in count rate due to the Doppler shift we have instead required $|\Delta/\Gamma| = \sqrt{3}/6$. With this latter tuning the temperature at equilibrium is

$$T \rightarrow \frac{2\sqrt{3}}{3} T_D \approx 1.155 T_D = 2.10 \times 10^{-4} \text{ K}, \quad (3.83)$$

and the limit on the rms velocity in the lower fluorescence region increases slightly to

$$\langle v_x^2 \rangle^{1/2} \rightarrow 0.0910 \text{ m/s}, \quad (3.84)$$

and the upper limit to the contribution to the size of the beam in the lower fluorescence region increases correspondingly to

$$\langle x^2 \rangle^{1/2} \rightarrow 1.16 \text{ mm}, \quad (3.85)$$

which is still acceptable.

We may ask if laser cooling will in fact operate at the desired tuning of $\Delta/\Gamma = \sqrt{3}/6 \approx 0.288$ instead

of at the standard tuning of $\Delta/\Gamma = 1/2 = 0.500$. In the standard tune, a shift in velocity of 2.72 m/s will shift an atomic frequency so that it lies at the peak of, instead of on the side of, the Lorentz profile of one of the lasers; we will take this as a measure of the Doppler cooling being significantly distorted. However that shift is 32.2 times the equilibrium rms velocity of 0.0847 m/s, and so an atom acquiring that velocity is improbable. For our desired tune the shift required to lose an atom is smaller, 1.57 m/s, and the rms velocity at equilibrium is larger, 0.0910 m/s; even so, the shift is still 17.3 times the rms velocity, so the distortion should still be negligible.

The growth in the beam size transverse to the laser beam scales as the square of the number of photons scattered, and so we could lower the contributions to $\langle z^2 \rangle^{1/2}$ and to $\langle y^2 \rangle^{1/2}$ by a factor of 2, down to 0.97 mm, if we can afford to reduce the number of photons scattered per atom by a factor of 4. Given that the number of photoelectrons counted per atom is presently 25.4, and that $25.4/4 = 6.34$ photoelectrons per atom would be acceptable, we have room to explore doing this.

3.10.4 Doppler Shift from Beam Heating

We examine the standard Lorentz profile for an atomic resonance of frequency ν_0 , and width in frequency ν_w , illuminated by a laser of frequency ν :

$$\frac{(\nu_w/2)^2}{(\nu_0 - \nu)^2 + (\nu_w/2)^2} . \quad (3.86)$$

We note that this profile has been scaled such that it equals 1 for $\nu = \nu_0$ and is 1/2 for $|\nu - \nu_0| = \nu_w/2$, where for ^{211}Fr and for the $7P_{3/2}$ state the full width at half maximum is $\nu_w = 7.58 \times 10^6$ Hz.

When illuminated by equal intensity, anti-propagating lasers, an atom is as likely to absorb a photon traveling left as one traveling right, and the average recoil velocity imparted to the atom for each photon scattered will be zero. Nonetheless the atom will acquire a distribution of velocities parallel to the laser axis with a finite root-mean-square

value, whose effects we seek to minimize [ret]. If ν is the frequency shift for some individual atom due to its velocity parallel to the beam, then the frequency of the laser as seen in the atomic rest frame is $\nu = \nu_l + \nu$, where ν_l is the frequency of the laser as seen in the lab. The rate of photon scatter in a retroreflected laser will be

$$f \equiv \frac{1}{2} \left[\frac{(\nu_w/2)^2}{(\nu_0 - \nu_l - \nu)^2 + (\nu_w/2)^2} + \frac{(\nu_w/2)^2}{(\nu_0 - \nu_l + \nu)^2 + (\nu_w/2)^2} \right] . \quad (3.87)$$

We note ν enters with different signs in the two denominators; and we note that we have scaled the result so that $f = 1$ when $\nu_l = \nu_0$ and $\nu = 0$.

We note that f is an even function of ν and so an expansion in powers of ν contains even powers only. If we were to tune the laser to $|\nu_0 - \nu_l| = \nu_w/2$ to optimize the Doppler cooling, we would have

$$f \rightarrow \frac{1}{2} + \left(\frac{\nu}{\nu_w}\right)^2 - 2\left(\frac{\nu}{\nu_w}\right)^4 + O(\nu^6) . \quad (3.88)$$

A Gaussian distribution in one dimension over the variable ν that has a standard deviation σ has the form

$$\frac{dP}{d\nu} = \frac{1}{\sigma\sqrt{2\pi}} e^{-\nu^2/2\sigma^2} , \quad (3.89)$$

and has the normalization

$$\int_{-\infty}^{\infty} \frac{dP}{d\nu} d\nu = 1 \quad (3.90)$$

and the expectation values

$$\int_{-\infty}^{\infty} \nu^2 \frac{dP}{d\nu} d\nu = \sigma^2 \quad \text{and} \quad \int_{-\infty}^{\infty} \nu^4 \frac{dP}{d\nu} d\nu = 3\sigma^4 . \quad (3.91)$$

If the velocity distribution is modeled as a Gaussian, then

$$\int_{-\infty}^{\infty} \frac{dP}{d\nu} \left[\frac{1}{2} + \frac{\nu^2}{\nu_w^2} + \dots \right] d\nu = \frac{1}{2} \left[1 + 2\left(\frac{\sigma}{\nu_w}\right)^2 + \dots \right] \quad (3.92)$$

Doppler cooling in the standard tune sets an upper limit to the velocity distribution of atoms moving parallel to the fluorescence laser of

$$\langle v_x^2 \rangle^{1/2} \leq 0.0847 \text{ m/s} . \quad (3.93)$$

If the velocity distribution is modeled as a Gaussian, the distribution of the corresponding Doppler shift has a standard deviation of

$$\sigma = \frac{0.0847 \text{ m/s}}{2.998 \times 10^8 \text{ m/s}} \times 4.17 \times 10^{14} \text{ Hz} = 1.18 \times 10^5 \text{ Hz} \quad (3.94)$$

and so for this limiting distribution we will have the dimensionless ratio

$$\frac{\sigma_z}{\nu_w} = \frac{1.18 \times 10^5 \text{ Hz}}{7.58 \times 10^6 \text{ Hz}} = 1.56 \times 10^{-2} . \quad (3.95)$$

Thus the fractional change in the fluorescence rate as a zero-temperature cloud warms to the Doppler cooling limit would be

$$+2 \left(\frac{\sigma_z}{\nu_w} \right)^2 = +4.8 \times 10^{-4} . \quad (3.96)$$

We choose to make this shift smaller by reducing the detuning of the lasers. If the lasers are tuned [ret] either above or below resonance so that

$$\frac{|\nu_0 - \nu_l|}{\nu_w} = \frac{\sqrt{3}}{6} , \quad (3.97)$$

then coefficient of the term in f of order ν^2 is zeroed, so that

$$f \rightarrow \frac{3}{4} + \frac{27}{4} \left(\frac{\nu}{\nu_w} \right)^4 + O(\nu)^6 . \quad (3.98)$$

From this we conclude

$$\begin{aligned} \int_{-\infty}^{\infty} \frac{dP}{d\nu} \left[\frac{3}{4} + \frac{27}{4} \frac{\nu^4}{\nu_w^4} + \dots \right] d\nu \\ = \frac{3}{4} \left[1 + 27 \left(\frac{\sigma}{\nu_w} \right)^4 + \dots \right] . \end{aligned} \quad (3.99)$$

We recall that changing the detuning from $|\Delta/\Gamma| = 1/2$ to $|\Delta/\Gamma| = \sqrt{3}/6$ increases the cooling limit on the velocity of atoms parallel to the laser beams to

$$\langle v_x^2 \rangle^{1/2} \rightarrow 0.0909 \text{ m/s} , \quad (3.100)$$

and correspondingly increases σ to

$$\sigma \rightarrow \frac{0.0909 \text{ m/s}}{2.998 \times 10^8 \text{ m/s}} \times 4.17 \times 10^{14} \text{ Hz} = 1.26 \times 10^5 \text{ Hz} \quad (3.101)$$

For this limiting distribution we will therefore have the dimensionless ratio

$$\frac{\sigma_z}{\nu_w} \rightarrow \frac{1.26 \times 10^5 \text{ Hz}}{7.58 \times 10^6 \text{ Hz}} = 1.67 \times 10^{-2} , \quad (3.102)$$

and the fractional change

$$27 \left(\frac{\sigma_z}{\nu_w} \right)^4 \rightarrow 2.11 \times 10^{-6} , \quad (3.103)$$

which is smaller by more than two orders of magnitude than the limit when one instead optimizes the Doppler cooling, while the fluorescence rate is actually larger by a factor of 1.5.

3.10.5 Detection Calibration

Our basic observable is the “survival probability”—the probability that in a mix of atoms that enter the upper fluorescence region in the ground $S_{1/2}$ state an atom will be found in the upper, $S_{1/2}$, $F = 5$ hyperfine level. We first fluoresce the transition $S_{1/2}$, $F = 5 \rightarrow P_{3/2}$, $F' = 6$ in the upper fluorescence region, and count photons. Then we apply the repump laser, tuned to the transition $S_{1/2}$, $F = 4 \rightarrow P_{3/2}$, $F' = 5$, which pumps the population in the lower hyperfine level into the upper. Then we fluoresce the transition $S_{1/2}$, $F = 5 \rightarrow P_{3/2}$, $F' = 6$ in the lower fluorescence region, and again count photons. If the detection efficiency in the upper and lower fluorescence regions were identical, the ratio of the counts recorded in the upper region to those recorded in the lower region would give the desired probability.

The detection efficiency cannot be made identical in the two regions. If we ignore at first the heating of the atomic beam in the upper region, finding the ratio of the actual detection efficiencies is straightforward. We first fluoresce the transition $S_{1/2}$, $F = 5 \rightarrow P_{3/2}$, $F' = 6$ in the upper fluorescence region, and count photons. Then we leave the repump laser off, and we fluoresce the transition $S_{1/2}$, $F = 5 \rightarrow P_{3/2}$, $F' = 6$ in the lower fluorescence region, and again count photons. The ratio of the number of photons recorded gives the desired ratio of detection efficiency. Given the assumption that no heating occurs in the upper region, the distribution of atoms entering the lower

region, and so the detection efficiency in the lower region, is independent of whether the atoms are in fact fluoresced in the upper region or not. All the inevitable differences in practice between the upper and lower regions—laser power, spot size, and alignment with the descending cloud; natural expansion of the cloud; transmission efficiency of the optic; quantum efficiency of the photomultiplier; what-have-you—would be taken into account exactly.

In practice the heating in the upper fluorescence region is significant, in the present design adding in quadrature the order of 1 mm rms to the beam size in the lower region in all three cartesian directions. What is produced in the upper region are two classes of atoms: the ones that began in the lower hyperfine level, that are not fluoresced, and remain “cold;” and the ones that began in the upper hyperfine level, that are fluoresced, and become “hot.” The cloud of “hot” atoms expands significantly before it enters the lower fluorescence region, and so the detection efficiency in the lower region will be different (almost certainly lower) than for the cloud of “cold” atoms.

The ratio of the detection efficiency for “hot” atoms in the lower region, to the detection efficiency for atoms in the upper region, is what in fact is measured by the calibration procedure already done. What is needed is the ratio for “cold” atoms in the lower region. This can be extracted by using the calibration laser (see Fig. 3.12) to optically pump the atoms before they enter the upper fluorescence region so that they have a predetermined, known ratio of population of atoms in the upper and in the lower hyperfine level; on fluorescence in the upper region, the population in the upper level becomes “hot” and that in the lower level remains “cold.” Measuring the detection efficiency as a function of the population allows the desired ratio to be extracted.

Most of the observables used to tune systematic effects to zero involve taking differences of the survival probability for atoms prepared with the axis of linear polarization of a state preparation laser making angles of opposite sign. These differences are zero even if the measured calibration of the detection efficiency for hot beam and for cold beam

are off, provided the true but unknown calibration is independent of the sign of the angle. We have arranged the experiment so that even the small beam heating on state preparation is independent of the sign of the angle, and so the true calibration will indeed be independent. We therefore do not need the calibration to be perfect in order, for example, to tune the various magnetic field integrals to zero.

3.11 Forming a Fountain of Atoms

3.11.1 Capture from a Vapor

Trap loading by capture from a vapor

The two commonly used methods for loading a magneto-optic trap are vapor capture [MvdS99a] and capture from a laser-slowed atomic beam. In vapor capture, neutral atoms are introduced into the magneto-optic trap vacuum chamber at thermal energies and allowed to collide with walls and windows. In one out of every 10^3 to 10^4 collisions, the atom will emerge with a velocity low enough to be captured into the magneto-optic trap.

This however only works if the atoms do not stick to the vacuum chamber walls or windows. For high vapor pressure, stable atoms, available in inexhaustible quantities, such as cesium and rubidium, it is only necessary to admit the vapor from a reservoir and allow the walls and windows to be coated with one or several layers of atoms before the vapor capture begins to work (over several days to a few weeks depending upon reservoir temperature and chamber surface area). And if kept under vacuum, vapor-capture MOTs with a small alkali reservoir containing a gram or so can operate without maintenance for years—the one used for the experiments in Ref. [AMG07, KAG05, AG03] and shown in Fig. 3.15 required only that the ion pump be refurbished roughly every 3 years.

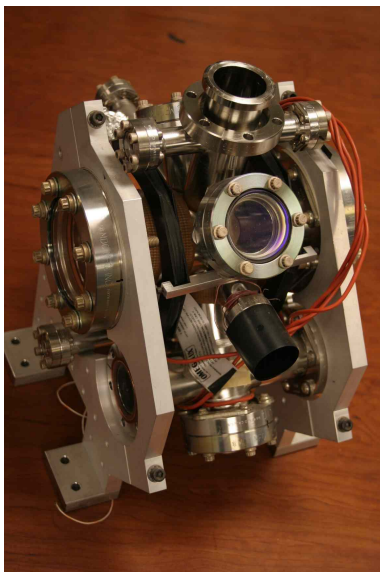


Figure 3.15: Magneto-optic trap chamber used for Cs fountain electron EDM proof-of-principle experiment and which may be recycled for use with one of the Cs prototype fountains.

Dryfilm coated walls

For francium (and other scarce, short lived, alkali atoms), the vapor capture technique is modified by using a clear nonstick coating, commonly referred to as dryfilm. Dryfilm coatings have been used for all francium trapping and cooling experiments done to date [SGG⁺96, LCV⁺97, AGLAO03, TBP⁺12] including ²²¹Fr trapping experiments done by collaboration members [LCV⁺97, TBP⁺12]. Dryfilm is a generic name for a number of polymer coatings with a silicon-oxygen backbone terminated with methyl groups. The suitability of these coatings for vapor capture trapping of scarce alkali atoms was extensively examined by Stephens, Rhodes, and Wieman [SRW94] who measured outgassing rates, chemical reaction rates, the effect of substrate material, and physisorption rates, and considered the relative difficulty of preparation.

Octadecyltrichlorosilane (OTS) on a PyrexTM (borosilicate glass) surface was found to give the best results. For this reason a glass cell is usually placed inside a vacuum chamber [AGLAO03], rather than coating the glass and metal chamber surfaces. The coatings, which require a hood, an

N₂ filled dry box, and standard laboratory safety procedures to prepare, but little else in the way of specialized equipment, are inexpensive, not particularly time consuming, and can be done in the laboratory. Unfortunately they do not work as well as desired.

It is thought that incorrectly formed polymers and insufficient numbers of methyl groups that shield the SiO bond in the backbone of the polymer from the alkali vapor lead to higher reaction rates [SRW94]. This would explain why OTS, which has 18 methyl groups, was the best dryfilm tested and why dryfilm on metals, where it is more difficult for the polymer to form correctly, was not as successful as dryfilm on glass¹⁵. The incorrectly formed region will react with alkali atoms. To prevent total chemical absorption of the francium at these sites, the coating is first “cured” with alkali (rubidium) vapor to fill these sites. The curing time [SRW94] needed is from a few hours when starting with a well formed coating to about a day for a less well formed coating¹⁶. Even when seemingly identical steps are used, there is some variability in the final product. Extreme heat will damage the coating creating a trade-off between the most efficient release of foil-collected francium and the longest coating lifetime.

Forming a francium vapor

To use francium, from TRIUMF or from the decay ²²⁵Ac, in a fountain, it must first be slowed, neutralized, and captured into a magneto-optic trap. Francium atoms from TRIUMF arrive at a kinetic energy of 30 keV while the francium daughter from the decay of ²²⁵Ac recoils with a kinetic energy of 105 keV from the 6 MeV alpha emission. The simplest way to thermalize the francium atoms is to stop them in the surface of a low-work-function

¹⁵Glass has a complex surface chemistry with atmospheric water vapor and liquid water, with different glass compositions behaving differently. An interesting investigation would be to try different glass compositions, especially those with the lowest percentages of alkali and alkaline earth ingredients.

¹⁶The coating used in Ref. [LCV⁺97], which was onto a glass and metal chamber, took longer than a few hours to cure.

metal such as yttrium (work function of 3.1 eV compared to francium's ionization potential of 4.073 eV) from which they may subsequently be evaporated as neutral atoms¹⁷ by heating. Because the 30 keV francium travels deeper into the foil than does few-keV francium, which has been previously used for loading magneto-optic traps, a smaller fraction will be released.

Using data from Melconian et al. [MTG⁺04] on the release of 15 keV ³⁷K TRIUMF beams, and on the release of 105 keV ²²¹Fr from Ni and Pt foils from Dinneen, Ghiorso and Gould [DGG96], we estimate that the release fraction of 30 keV Fr will be about half of the release fraction at 2–3 keV (about 0.4 compared to 0.8). The yield may be improved by heating to higher temperatures (in excess of 1200 K) but this poses some risk of shortening the lifetime of the dryfilm coating which is heat sensitive.

After collecting francium for about 10 seconds, the yttrium foil is heated to drive off neutral francium at thermal energies. The foil is positioned near a small opening in a dryfilm-coated glass cell inside the vacuum chamber. For ²¹⁰Fr collected at just a few keV on a yttrium foil, the overall loading efficiency, dominated by losses in the dryfilm-coated walls, has been measured by Aubin et al. [AGL03] to be 1.2%. The 1.2% efficiency may represent a situation where everything is working well. That may not be expected to continue over the hundreds of hours needed to perform an EDM experiment because dryfilm coatings deteriorate both with age and exposure to heat. And it is common to have differences in the performance of seemingly identically prepared dryfilm coatings. Combined with a possible reduced efficiency from using Fr ion beams with kinetic energies higher than 2–3 keV, we estimate an average combined efficiency of 0.4% in going from francium ions to trapped francium atoms. This may be expected to improve with further development work at the francium trapping facility at TRIUMF [TBP⁺13].

¹⁷There are only a few metals whose work functions are lower than francium's 4.073 eV ionization potential and only cesium has a lower ionization potential than francium. Rubidium's ionization potential (4.177 eV) is nearly identical to francium's.

Dual trap system

While all francium MOTs to date have had their laser beams pass through dryfilm-coated glass, the dryfilm coating may not allow laser beams to have the optical quality and spatial uniformity desired to achieve optimal launching and sub-Doppler cooling of the atoms. And to launch the francium atoms into a fountain, some portion of the chamber must be opened. Therefore, a dual-trap system shown in Fig. 3.16 with a collector MOT and a main MOT will be used.

The collector MOT will be formed inside the dryfilm coated glass cell, placed inside a metal vacuum chamber with glass viewports, and the thermal francium vapor will be introduced through a small opening. After the atoms from the yttrium foil are trapped, the yttrium foil is removed and the packet of cold atoms are pushed by a laser beam back through the opening to a main MOT, a short distance away in a separate chamber. Although there are too few background francium atoms to cause significant collisional losses, the dryfilm coating itself has a high outgassing rate and consequently the pressure inside the cell is unlikely to be compatible

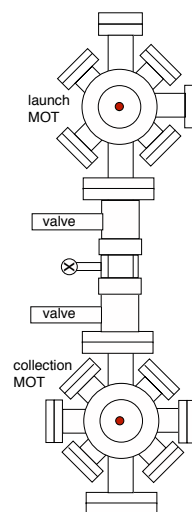


Figure 3.16: Magneto-optic traps (MOTs) used to collect, cool, trap, and launch Fr. The transfer line between the MOTs doubles as an air lock allowing the collector MOT vacuum chamber to be replaced without exposing either the launching MOT or the new (or old) collector MOT to air.

with long trap lifetimes.

The main MOT, containing only francium atoms that have already been cooled to a few hundred μK and trapped, needs no wall coatings and can operate at vacuum pressures compatible with long trap lifetimes. Multiple packets of francium atoms can be transferred from the collection MOT to the main MOT (because the atoms are laser cooled). From the main MOT, the atoms can be launched and cooled by laser beams that have not had to pass through dryfilm coated surfaces.

For Cs, which will be used to develop the experiment (See Chapter 7), the rate at which atoms are loaded into a MOT is proportional to the vapor pressure of the alkali atoms, typically about 10^{-8} Torr, which is set by the reservoir temperature, as is the rate at which thermal alkali atoms from the vapor scatter atoms out of the trap. About 10^8 atoms can be loaded in 100 ms. The Cs fountain(s) will use a two-MOT configuration although the airlock system is not needed for cesium. This is the technique used by, among others, Gibble and coworkers [LG98, GCL95, HXLG07, Har07, Gib08] at Pennsylvania State University. They launch a packet of 1.6×10^9 cesium atoms every second.

Using dryfilm-coated cells with ^{211}Fr and ^{221}Fr

For an experiment on a stable alkali atom, losing a day or two to replace a poorly functioning or worn out dryfilm cell is a mild nuisance; during a ^{221}Fr experiment, with a ten-day half-life source, it is a setback; but during a run at TRIUMF, it is a hardship. One way around this problem is to have a spare dryfilm coated cell, already cured with rubidium vapor, mounted in a replacement chamber with its own connection valve, vacuum pump, and MOT hardware (magnetic field coils, anti-reflection coated windows etc.), and held under vacuum. The collector chamber is attached to the main chamber with two vacuum gate valves having a small pump out between the valves as shown in Fig. 3.16.

To replace chambers, an airlock is formed as two valves facing each other are closed and the space

between them brought up to air (dry nitrogen). The MOT-forming laser optics will need to be easily removed and replaced in position (See, for example [KTK⁺08]). The old collection chamber is then removed, a new collection chamber with its own pump and valve then replaces the old collection MOT chamber, and the space between the valves pumped out by a separate (turbomolecular) pump¹⁸. With planning and practice this procedure could be completed in under one hour.

3.11.2 Capture from a Laser-Slowed Beam

While vapor capture of francium from dryfilm coated walls is easy, convenient, and established, the capture yields are disappointing and its reliability is a potential concern. The alternative method to capturing francium is to form a thermal beam of francium and slow it with counter propagating laser light. While a beam slower of the efficiency we propose has not yet be constructed, many of the features we need have already been demonstrated in high brightness beam slowers and in low divergence thermal beam sources [SVH05, DGG96].

In laser slowing, a laser beam in resonance with the cycling transition ($7S_{1/2}$, $F = 5 \leftrightarrow 7P_{3/2}$ $F = 6$ in ^{211}Fr) is directed against the atomic beam direction. A longitudinally changing magnetic field is applied along the atomic beam to compensate for the changing Doppler shift as the atoms slow. Commonly called Zeeman slowers, these devices have been used to produce very bright beams of alkali atoms, but there has until now been no incentive to build a very high efficiency Zeeman slower. In Chapter 10 we describe the conceptual design for a Zeeman slower with a ratio of slowed atoms to atoms leaving the thermal source of nearly one half¹⁹. A summary of the design and a schematic is

¹⁸It may be desirable to set up a dry nitrogen tent. Such a tent is used at the LBNL Advanced Light Source (ALS) to access the main ring ($\approx 10^{-11}$ Torr) without having to bake afterwards.

¹⁹The increase in (normalized) phase space due to slowing can, in alkali atoms, be removed by laser cooling as many times as necessary, transforming the problem to one of beam transport.

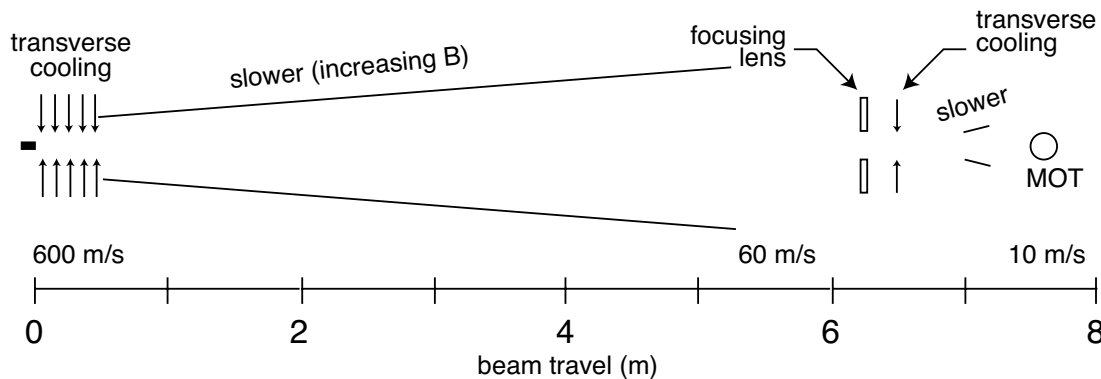


Figure 3.17: Schematic diagram of the slowing apparatus. The orthotropic oven (dark rectangle at the extreme left) operates at 1220 K and produces a beam of Fr with a maximum divergence of 0.030 radians. In the francium beam, 88.8% of the atoms have velocity of 600 m/s or less and therefore have transverse velocities of 18 m/s or less. It is these atoms that are cooled and slowed. The atoms are first transversely cooled to reduce the transverse velocity to ≈ 0.1 m/s using a succession of lasers beams detuned by three, two and one linewidths. The francium beam, which at this point has grown to about ± 5 mm width, enters the first slower section. It is slowed to 60 m/s and, due to heating, increases its transverse velocity to about 1.25 m/s. At 60 m/s its divergence is now 0.021 radians. The beam is allowed to drift and is then focused by a permanent-magnet sextupole (or by a two-dimensional MOT) with a focal length of 30 cm. This bring the beam to a focus with a transverse velocity of about 6 m/s. At this point the francium is laser cooled back to about 0.1 m/s. It then enters a second slower which reduces the atom's velocity to 10 m/s. From there it can either directly enter the MOT or be further focused and transported.

given in Fig. 3.17.

The problems to be overcome include the large divergence of a thermal beam source, the relatively low deceleration due to francium's high mass, and the increase in divergence as the beam is slowed. These are overcome by using an orthotropic oven, multiple stages of two-dimensional transverse cooling, and a very long slower in two sections with focusing and transverse cooling between the sections. If necessary, a final focus to match the francium beam to the MOT can be added. The resulting apparatus (Fig. 10.1) is long and may require over a Watt of laser power, but appears capable of accepting over half of the atoms, initially free inside the oven, into a MOT with a capture velocity of as low as ten m/s.

3.11.3 Atom Launching and Cooling

The MOT geometry (Fig. 3.16) has two laser beams in the horizontal plane and four laser beams in the vertical plane with the vertical beams at 45 degrees to the horizontal. In this geometry there is

no vertical laser beam for trapping or launching and so it can be used where there is a set of electric field plates with limited gap spacing above the trap. It also allows the trap to begin operating again while the atoms are traveling on their ballistic trajectory. The atoms are launched from the MOT starting from a cloud that is 2 mm FWHM for a cloud of 1×10^8 atoms [LSW92, PAEC94], and is smaller for fewer atoms. After launching, and in the moving frame, the atoms are cooled below the Doppler limit using polarization gradient cooling [MvdS99c] with the same lasers used for launching. This will cool the atoms to $2.5 \mu\text{K}$ (most probable transverse velocity is 14 mm/s) or less [FG99, LG98, JSP⁺02, VRM⁺05].

The standard method for launching atoms, used for previous related experiments [AMG07, KAG05, AG03, MDG99] and all other fountains and fountain clocks, is to create a moving molasses by blue detuning the upward pointing laser beams and red detuning, by the same amount, the downward pointing laser beams. The atoms accelerate upward until they reach a velocity where their Doppler shift makes all of the laser beams appear to be of the same wavelength. Just before detuning the laser

beams, the MOT magnetic field is turned off. If the detunings are too large (or too small) the acceleration approaches zero. To reach launch velocities beyond about 5 m/s it is most efficient to perform a two-step launch: first the lasers are detuned to accelerate the atoms to 3.5 m/s and then detuned again to complete the acceleration²⁰.

To capture the largest numbers of atoms from a background vapor, or to capture atoms with the highest velocities from a beam, illuminating a large volume with high laser power is unsurpassed [GKC92]. And for efficient launching and cooling, starting with laser beams of high power density allows large areas to be illuminated and the wavefronts to be cleaned up by collimation. In systems that trap large numbers of atoms, lasers with over 1000 mW output are used [GKC92], and in systems that trap, launch, and cool atoms, multiple Ti:sapphire laser systems producing 1750 mW of power have been used [Har07, Gib08]. In the case of ²¹¹Fr and ²²¹Fr with 7S_{1/2} ground state hyperfine splittings of 43.6 GHz and 18.6 GHz, respectively²¹, a separate laser will be needed for repumping, although this can be a low power laser.

3.12 Atom Transport and Focusing

3.12.1 Atoms in Inhomogeneous Electric Fields

All atoms are polarizable. In an external electric field E , the electron cloud is attracted to the positive electrode and the nucleus is attracted to the negative electrode, resulting in an *induced* electric

dipole moment of the atom that conserves parity and time reversal invariance. Consequently, all atoms in an electric field gradient will experience a force and having, in their ground states, lower potential energies in an electric field will therefore accelerate into the field. The induced electric dipole moment interacting with the electric field results in an increase in the (binding) energy W of the ground state given by

$$W = -\frac{1}{2}\alpha E^2, \quad (3.104)$$

where $E = (E_x^2 + E_y^2 + E_z^2)^{1/2}$, and $\alpha = 5.3 \times 10^{-39} \text{ J m}^2 \text{ V}^{-2} = 8.0 \times 10^{-6} \text{ Hz m}^2 \text{ V}^{-2}$ is the static dipole polarizability of francium in its 7S_{1/2} ground state [SJD99]. An electric field of 10^7 V/m will increase the ground state binding energy by 800 MHz²². Neglecting gravity, a francium atom with initial velocity of v_i entering an electric field of 10^7 V/m will, from conservation of energy, reach a final velocity v_f given by

$$v_f^2 = v_i^2 + \frac{\alpha E^2}{m} = v_i^2 + 1.51 \text{ J/m}, \quad (3.105)$$

where $m = 3.5 \times 10^{-25} \text{ kg}$ is the mass of ²¹¹Fr. Consequently a francium atom traveling at 3 m/s will accelerate to 3.24 m/s upon entering the electric field, but an atom traveling at 0.5 m/s will accelerate to 1.3 m/s.

At any given point, the electric field gradient interacting with the induced electric dipole moment produces a force on the atom and an acceleration a . For a gradient in the z direction the acceleration is

$$a_z = -\frac{1}{m} \frac{\partial W}{\partial z} = -\frac{1}{m} \frac{\partial W}{\partial E} \frac{\partial E}{\partial z} = \frac{\alpha}{m} E \frac{\partial E}{\partial z}. \quad (3.106)$$

The force from an electric field gradient on ground state atoms is always towards the stronger field (strong-field seeking). As shown in Fig. 3.18, this

²⁰Because the atoms start out in a MOT located near the center of the laser beams, the lower half of the laser beams is not available to contribute to the launch and to cooling. More of the laser beam can be utilized by first launching the atoms downward at a small velocity and after some milliseconds, applying the larger upward acceleration [Gib08].

²¹Relative to cesium, ²¹¹Fr and ²²¹Fr fountain primary frequency standards would respectively be five times and two times more precise. The collisional phase shifts for francium isotopes are to our knowledge, not yet known.

²²Because the hyperfine splittings involve radial wavefunctions, relativistic effects cause small differences in the polarizability of the two ground state hyperfine levels and even smaller differences between M levels; these relativistic effects give rise to the tensor polarizabilities which are roughly six orders of magnitude smaller than the static dipole polarizability.

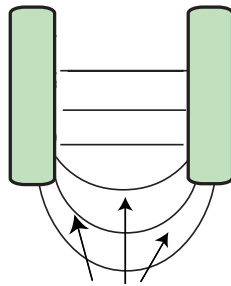


Figure 3.18: Defocusing in the fringe electric field. The force on ground state atoms is always towards the stronger field.

results in a beam of atoms being accelerated into the electric field and defocused as they enter or exit the electric field. If the atom, displaced 2 mm from the axis, experiences an increase of 2% in the fringe field of $5 \times 10^6 \text{ V m}^{-1}$, the gradient is $2 \times 10^8 \text{ V m}^{-2}$ and $a_y = 15 \text{ ms}^{-2}$ (about 50% larger than the acceleration due to gravity). An atom spending 10^{-3} seconds (the time it takes to travel about 3 mm) in an average field and gradient of this magnitude will then acquire a transverse velocity $v_y = 15 \text{ mm/s}$, which is too large for it to survive the 0.67 second journey through electric field plates with a 5 mm half-gap.

The way to overcome the defocusing and maintain a reasonable electric field gap spacing, reasonable voltages, and hence a manageably-sized apparatus, is to focus the atoms using electrostatic lenses placed at the entrance to the main electric field.

3.12.2 Electrostatic Focusing Lenses

It is necessary to use at least two lenses with alternating gradients in the directions perpendicular to the beam direction (transverse directions). Each lens focuses in one transverse direction while defocusing in the other, because an electric field that is uniform along the beam direction can not, in free space, also have a *maximum* in both transverse directions. A net focusing in both transverse directions is achieved if the alternating gradient lenses have linear restoring forces. Atoms defocused, in

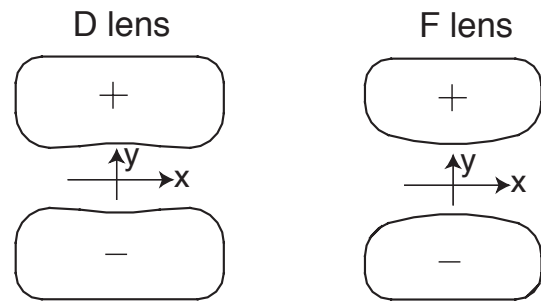


Figure 3.19: Electrostatic lenses that focus in the y direction and defocus in the x direction (D lens) and focus in the x direction and defocus in the y direction (F lens). The curvature of the focusing electrodes has been greatly exaggerated.

say the x direction in the first lens, experience a stronger restoring force in the second lens. And atoms focused in the y direction in the first lens are closer to the centerline and experience smaller defocusing in the second lens.

The focusing direction is determined by the curvature of the electrodes, as shown in Fig. 3.19. For best results the forces should be linear in the displacement in x and y from the z axis. The electric field that comes closest to producing forces that are linear in displacement from the z axis of the lens is the field generated by the combination of a sextupole potential plus a dipole potential [KLG02]. A quadrupole component is not used because it will deflect the atoms. A small decapole potential may improve the linearity slightly, but otherwise the presence of higher order terms found in cylindrical electrodes produces forces that are nonlinear in the displacement [KLG02]. Nonlinear forces can cause beam loss and larger, more diffuse, beams.

The amount of curvature needed to form a focusing lens is slight. In fact if the curvature is anything but slight, nonlinearities will arise. For focusing francium, the variation in gap spacing within a lens is 200 microns or less over the center 1 cm, or less than 2%. It is important to note that the force does not depend on the direction of the electric field.

Although an F–D or D–F lens doublet can focus a beam in both transverse planes, the ratio of image size to object size (magnification) in

the two planes are unequal: if one magnification is less than one, the other will be greater than one. We therefore chose a triplet (D–F–D) lens, which allows us to focus the beam equally in both planes. The physics of lens design and the methods used for trajectory calculations are described in Ref. [KLG02, KAG05, Kal11] and their application to the francium fountain is discussed in the following sections.

As shown in Fig. 3.20, the fountain uses an electrostatic focusing triplet D1–F2–D3 at the entrance to the E4 main electric field plates. It consists of two D lenses (Fig. 3.19) that defocus in the transverse x direction while focusing in the y direction (which is the electric field direction). The F lens (Fig. 3.19) in the middle, does the opposite. The fo-

cusing triplet is close to E4 to, otherwise the atoms would defocus traveling through additional electric fringe fields. A grounded electric field clamp (C0 in Table 3.8), is located 2.4 cm upstream of the entrance to the D1 lens. The polarity of D1, F2, and D3 is the same as E4 and reverses when E4 reverses. In the absence of a permanent EDM, the forces on an atom generated by the lenses are independent of their polarity.

Table 3.8: Electrostatic Lens Parameters

Lens	length L_p (m)	bottom	top	Sextupole
		radius r_c (mm)	radius r_d (mm)	strength A_3 (m ⁻²)
C0	0.0180	6	6	0
D1	0.1420	30	1.5	+400
F2	0.1137	1.5	1.5	-400
D3	0.0557	1.5	1.5	+400
E4	0.60	2.5	2.5	0

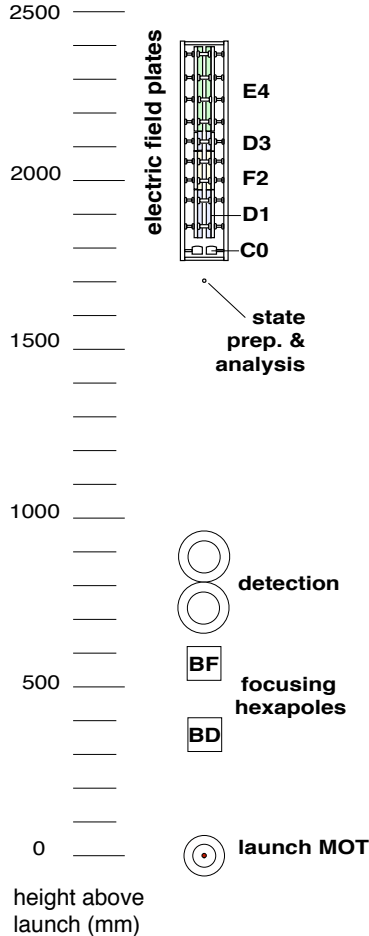


Figure 3.20: Schematic of the Fr fountain electron EDM experiment electric field elements.

Table 3.8 shows the lens parameters used. The half-gap spacing, r_p , for the F and D triplet lens elements is 6 mm, and the half gap spacing for the main electric field plates E4 is 5 mm. The larger gap spacing for the triplet lenses keeps the electric fields in the D lenses from exceeding those in E4 as one moves away from the beam centerline. The nominal voltages for all of the D, F, and E elements is ± 50 kV. In order to tune the lenses, the voltages on the triplet elements will need to be varied slightly: to allow this the D and F lens elements are electrically isolated from each other and from E4 and have a 1.5 mm space between them.

The 30 cm end radii (r_c) at the bottom the of the D lenses helps reduce defocusing effects (See [Kal11]). The spacing from the end of C0 to the start of D1 is 24 mm (but may be reduced to 12 mm). C0 is used to limit the time that state prepared atoms spend in weak electric fields. This helps reduce motional systematic effects.

The total electric field in the fountain can be expressed ([KLG02, KAG05, Kal11]) in the

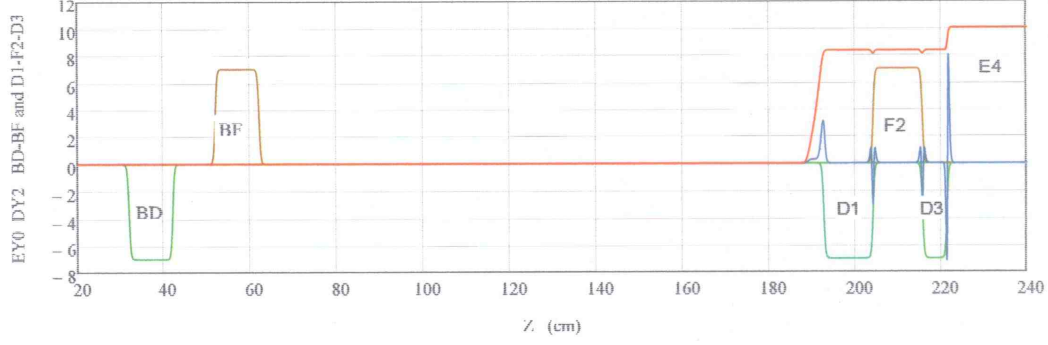


Figure 3.21: The lens-fields E_{y0} (red), D_{y2} (blue), and E_{s0} and B_{s2} (arbitrary scale) in the eEDM-fountain. BF and F3 are shown in brown and BD, D1, and D3 in green.

form:

$$\begin{aligned}
 E^2(x, y, z) = & E_{y0}^2(z) \\
 & + 2A_3 E_{y0}(z) E_{s0}(z) [x^2 - y^2] \\
 & + A_3^2 E_{s0}^2(z) [x^2 + y^2]^2 \\
 & + D_{y2}(z) [1 + 3A_3 x^2] y^2 \\
 & + \frac{1}{2} D_{y4}(z) y^4 + \frac{1}{3} D_{y6}(z) y^6
 \end{aligned} \quad (3.107)$$

where $E_{y0}(z) \equiv E(x = 0, y = 0, z)$ is the electric field on axis with derivatives $E_{y1} = dE_{y0}/dz$ etc.

The lens end-field focusing/defocusing is given by the functions D_{y2} , D_{y4} , and D_{y6} , which can be calculated from the field on axis:

$$D_{y2} = E_{y1}^2 - E_{y0} E_{y2}$$

$$D_{y4} = \frac{1}{2} E_{y2}^2 - \frac{2}{3} E_{y1} E_{y3} + \frac{1}{6} E_{y0} E_{y4}$$

$$D_{y6} = \frac{1}{12} E_{y3}^2 - \frac{1}{8} E_{y2} E_{y4} + \frac{1}{20} E_{y1} E_{y5} - \frac{1}{120} E_{y0} E_{y6}$$

or extracted from the 2D (y, z) longitudinal field (with no transverse sextupole field) for which

$$\begin{aligned}
 D_{ye}(y, z) & \equiv \frac{1}{2y} \frac{\partial E^2}{\partial y} \\
 & = D_{y2}(z) + D_{y4}(z) y^2 + D_{y6}(z) y^4
 \end{aligned}$$

In general, the defocusing field consists of short range focusing/defocusing peaks at a lens entrance/exit, or in the gaps between lenses, as shown in Fig. 3.21.

The lens transverse-focusing is given by the sextupole field $E_{A3}(z) \equiv A_3 E_{s0}(z)$, where A_3 is the sextupole strength relative to the dipole field E_{y0} . The sign of A_3 gives the direction in which the atoms are focused:

$A_3 < 0$ then F-lens (x -focus, y -defocus)

$A_3 > 0$ then D-lens (x -defocus, y -focus)

and its value determines the transverse curvature of the F and D lenses. To lowest order ($r_p^2 |A_3| \ll 1$), the plate half-gap is:

$$y_p = r_{p0} [1 - A_3 x^2 + A_3^2 x^4], \quad (3.108)$$

where r_{p0} is its value at the center ($x = 0$). **This is the equation that is used to generate the F and D lenses.**

The sextupole field's longitudinal dependence is given by the form function $E_{s0}(z)$, with normalization $(E_{s0})_{\max} = E_p = (E_{y0})_{\max}$. Here the maximum dipole field is $E_p = V_p/r_p$, for an electrode with half-gap r_p and plate potential V_p .

The lens-fields E_{y0} , D_{y2} and E_{s0} , needed to calculate the linear-focusing envelope in the eEDM-fountain, are shown in Fig. 3.21.

The D1 lens end-fields D_{y2} , D_{y4} and D_{y6} are as shown in Fig. 3.22.

The linear/nonlinear defocusing powers for the C0-D1 end-field are $p_{y2} = 0.2818$, $p_{y4} = 0.0330$, and $p_{y6} = 0.0070$. The linear defocusing power for the D1-F2, F2-D3 gaps is $p_{y2} = 0.0028$, and for the D3-E4 gap it is $p_{y2} = 0.0527$.

3.12.3 Atom Focusing with Magnetic Sextupole Fields

Outside the magnetic shielding, we can use a magnetic sextupole-field in the BD-BF lens doublet to focus or defocus the beam in the transverse plane. The magnetic scalar sextupole potential in the lens is:

$$-\Phi_B(x, y, z) = \frac{1}{2} B_{s2}(Z) (x^2 y - \frac{1}{3} y^3)$$

where

$$B_{s2} \equiv \frac{\partial^2 B}{\partial r^2} = \frac{2B_s}{r_s^2}$$

and B_s is the pole-tip field and r_s its radius.

The transverse magnetic fields are then

$$\begin{aligned} B_x(x, y, Z) &= B_{s2}(Z)xy \\ B_y(x, y, Z) &= \frac{1}{2} B_{s2}(Z)(x^2 - y^2) \end{aligned}$$

and the total magnetic field in the lenses is then just the pure sextupole field

$$B(x, y, Z) = \frac{1}{2} B_{s2}(Z)(x^2 + y^2) \quad (3.109)$$

since the end-field and nonlinear terms can be neglected.

An atom with magnetic dipole moment μ_B in the magnetic field B has the potential energy:

$$W = -\sigma_B \mu_B g_F M B$$

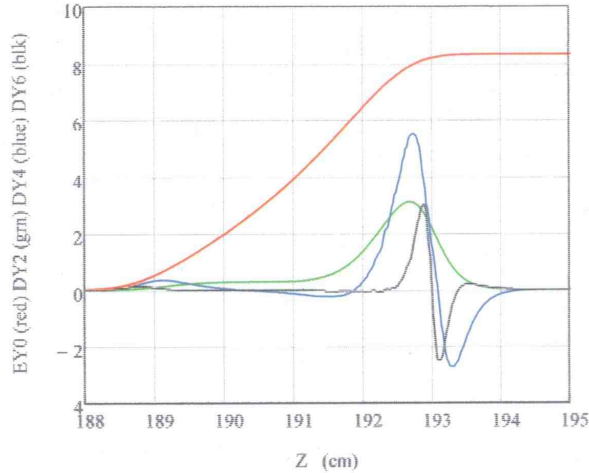


Figure 3.22: The lens-fields E_{y0} , D_{y2} , D_{y4} and D_{y6} (arbitrary scale) at the entrance of the D1 lens. The field colors are listed in the left axis.

where $\mu_B = 9.274 \times 10^{-24} \text{ JT}^{-1}$ is the magnetic dipole moment (Bohr magneton), which can be respectively parallel (defocusing: $\sigma_B = +1$ corresponding to $M = -5$) or antiparallel (focusing: $\sigma_B = -1$ corresponding to $M = +5$) to the magnetic field B and $g_F \approx 1/5$ is the Landé g factor for the ^{211}Fr $F = 5$ manifold.

This produces a focusing/defocusing force on the atom in the transverse plane of:

$$F_r = -\frac{\partial W}{\partial r} = \sigma_B \mu_B B_{s2} r$$

where $r = \sqrt{x^2 + y^2}$ in cylindrical coordinates. We see that the force produced is linear with displacement r , and has the same strength in all transverse directions (x and y).

Table 3.9: Magnetic Lens Parameters

Quantity	BD Lens	BF Lens
Length L_p (cm)	10.0	10.0
Focusing polarity σ_B	+1 (defocus)	-1 (focus)
Strength B_{s2} (T/m ²)	95.6	55.8

The magnetic lens parameters for the francium fountain are given in Table 3.9. An atom will focus if it is in a magnetic field in a state of $M > 0$ and defocus if $M < 0$. Francium atoms, after launch and cooling, enter a weak vertical magnetic field (guide field) and are optically pumped into the $M = -5$ state using vertically traveling circular polarized laser beams. Between the BD and BF lenses, the magnetic guide field goes to zero and then reverses, so that atoms entering the BF lens are now relative to the magnetic field in the $M = +5$ state and will focus in the BF magnet. The guide magnetic field may be just two loops of wire forming an anti Helmholtz field.

We will of course optically pump all francium atoms into a common state aligned with the magnetic field, either the $7S_{1/2} |55\rangle$ or the $7S_{1/2} |5, -5\rangle$, before the atoms pass through a magnetic lens so that all the atoms in the beam focus or defocus equally.

3.12.4 Equations of Motion

The Hamiltonian of a neutral francium atom in the fountain, with static electric and magnetic lens-fields, and in the coordinate system of Fig. 3.21, is:

$$H = \frac{m|\mathbf{v}|^2}{2} + mgZ - \sigma_B \mu_B B - \frac{\alpha E^2}{2} \quad (3.110)$$

where $m = 3.504 \times 10^{-25}$ kg is the mass (for ^{211}Fr), and $|\mathbf{v}| = \sqrt{\mathbf{v}_x^2 + \mathbf{v}_y^2 + \mathbf{v}_z^2}$ is the total velocity, $g = 9.80 \text{ m s}^{-2}$ is the acceleration of gravity, $\alpha = 5.27 \times 10^{-39} \text{ J m}^2 \text{ V}^{-2}$ is the static dipole polarizability of francium in its ground state [SJD99] (virtually identical for all M and F), and E is the electric field strength.

The equation of motion for an atom in the fountain is:

$$m \frac{d\mathbf{v}}{dt} = -\nabla H.$$

where the Hamiltonian H is given in Eq. 3.110, the C0–D1–F2–D3–E4 lens electrostatic field E is given in Eq. 3.107, and the BD–BF lens magnetic field B is given in Eq. 3.109.

The trajectory equations (acceleration/force) in the transverse (x - y) plane, for an atom in a fountain with gravitational and static electric and magnetic fields are then:

$$\begin{aligned} \frac{dv_x}{dt} &= -\frac{1}{m} \frac{\partial H}{\partial x} = \left[\left(\frac{\sigma_B \mu_B}{m} \right) B_{S2}(Z) + \frac{\alpha}{m} J_x(x, y, Z) \right] x \\ \frac{dv_y}{dt} &= -\frac{1}{m} \frac{\partial H}{\partial y} = \left[\left(\frac{\sigma_B \mu_B}{m} \right) B_{S2}(Z) + \frac{\alpha}{m} J_y(x, y, Z) \right] y \end{aligned}$$

where

$$\begin{aligned} J_x(x, y, Z) &= 2A_3 E_{S0}(Z) \\ &\quad \times [+E_{y0}(Z) + A_3 E_{S0}(Z)(x^2 + y^2) \\ &\quad + 3A_3 D_{y2}(Z)y^2] \\ J_y(x, y, Z) &= 2A_3 E_{S0}(Z) \\ &\quad \times [-E_{y0}(Z) + A_3 E_{S0}(Z)(x^2 + y^2) \\ &\quad + D_{y2}(Z)[1 + 3A_3 x^2] \\ &\quad + D_{y4}(Z)y^2 + D_{y6}(Z)y^4] \end{aligned}$$

and in the longitudinal (Z) direction we have:

$$\begin{aligned} \frac{dv_Z}{dt} &= -\frac{1}{m} \frac{\partial H}{\partial Z} \\ &= -g + \frac{\sigma_B \mu_B}{2m} B_{S2}(Z)(x^2 + y^2) \\ &\quad + 2\frac{\alpha}{m} \left\{ E_{y0}(Z)E_{y1}(Z) \right. \\ &\quad + \frac{1}{2}D'_{y2}(Z)[1 + 3A_3 x^2]y^2 \\ &\quad + \frac{1}{4}D'_{y4}(Z)y^4 + \frac{1}{6}D'_{y6}(Z)y^6 \\ &\quad + A_3 [E_{y1}(Z)E_{S0}(Z) \\ &\quad \quad + E_{y0}(Z)E_{S1}(Z)](x^2 - y^2) \\ &\quad \left. + A_3^2 E_{S0}(Z)E_{S1}(Z)(x^2 + y^2)^2 \right\} \end{aligned}$$

where

$$E_{S1} = \frac{dE_{S0}}{dz}, \quad B_{S1} = \frac{dB_{S0}}{dz} \quad \text{and} \quad D'_{y2} = \frac{dD_{y2}}{dz} \quad \text{etc.}$$

The central trajectory of the atom bunch ($x_c = 0$, $v_{xc} = 0$, $y_c = 0$, Z_c , v_{x0}) can be calculated from:

$$v_{Zc} \frac{dv_{Zc}}{dZ_c} = -g + \frac{\alpha}{m} E_{y0}(Z_c)E_{y1}(Z_c)$$

and this gives us the local longitudinal phase-space coordinates ($Z = Z - Z_c$, $v_Z = v_Z - v_{Zc}$). If the forces in the (x, y, z)-direction are linear and uncoupled, then the trajectory equations become:

$$\frac{d\mathbf{v}_x}{dt} + G_x x = 0, \quad \frac{d\mathbf{v}_y}{dt} + G_y y = 0, \quad \frac{dv_z}{dt} + G_z z = 0,$$

with focusing fields:

$$G_x(Z_c) = -\frac{\sigma_B \mu_B}{m} B_{S2}(Z) - \frac{\alpha}{m} 2A_3 E_{S0}(Z_c)E_{y0}(Z_c)$$

$$\begin{aligned} G_y(Z_c) &= -\frac{\sigma_B \mu_B}{m} B_{S2}(Z) + \frac{\alpha}{m} 2A_3 E_{S0}(Z_c)E_{y0}(Z_c) \\ &\quad - D_{y2}(Z_c) \end{aligned}$$

$$G_z(Z_c) = -\frac{\alpha}{m} D_{z2}(Z_c)$$

where

$$D_{y2} = E_{y1}^2 - E_{y0}E_{y2} \quad \text{and} \quad D_{z2} = E_{y1}^2 + E_{y0}E_{y2}.$$

The atom trajectories in the three 2D phase-spaces (x, v_x) , etc., are independent of each other, with the focusing/defocusing fields depending only on the longitudinal position Z_c .

The atom bunch central trajectory is taken to be the one with the average beam phase-space coordinates $\langle x \rangle = 0, \langle v_x \rangle = 0, \langle y \rangle = 0, \langle v_y \rangle = 0, \langle Z \rangle = Z_c$, and $\langle V_z \rangle = V_{Zc}$ and ideally the central trajectory moves along the optic axis of the lenses with no steering. Any single atom in the bunch then has the relative phase-space coordinates $(x, v_x, y, v_y, z = Z - Z_c, v_z = V_z - V_{Zc})$, and the atom distribution is specified by its RMS moments: $\sigma_x^2 = \langle x^2 \rangle$, $\sigma_{xvx} = \langle xv_x \rangle$, $\sigma_{vx}^2 = \langle v_x^2 \rangle$, etc.

Then, for any beam distribution in phase-space, we can calculate the evolution of its RMS moments, $(\sigma_x^2, \sigma_{xvx}, \sigma_{vx}^2 \text{ etc.})$, from the envelope equations for the x -direction (focusing: $G_x > 0$, defocusing: $G_x < 0$)

$$\begin{aligned} \frac{d\sigma_x^2}{dt} - 2\sigma_{xvx} &= 0 \\ \frac{d\sigma_{xvx}}{dt} - \sigma_{vx}^2 + G_x(Z_c)\sigma_x^2 &= 0 \\ \frac{d\sigma_{vx}^2}{dt} + 2G_x(Z_c)\sigma_{xvx} &= 0 \end{aligned}$$

and equations of the same form for the y and z directions. Here at time t the central atom is at the longitudinal position Z_c with velocity V_{zc} .

The above three envelope equations are not independent, but are connected by the constant of the motion the RMS emittance:

$$\epsilon_x = \sqrt{\sigma_x^2 \sigma_{vx}^2 - \sigma_{xvx}^2}$$

These RMS/envelope equations also apply to the evolution of the Kapchinsky-Vladimirsky (KV) beam distribution, which at any time t or position Z_c , consists of a uniform distribution of trajectories on the boundary of a 2D (x, v_x) phase-space ellipse given by:

$$\sigma_{vx}^2 x^2 - 2\sigma_{xvx} x v_x + \sigma_x^2 v_x^2 = \epsilon_x^2$$

with conserved emittance area $A_x = \pi \epsilon_x$ and maximum envelope sizes (σ_x, σ_{vx}) .

At a waist ($\sigma_{xvx} = 0$), such as the fountain launch point, the phase-space ellipse is upright with

$$\frac{x^2}{\sigma_x^2} + \frac{v_x^2}{\sigma_{vx}^2} = 1 \text{ and emittance } \epsilon_x = \sigma_x \sigma_{vx}$$

3.12.5 Linear Focusing Design Optics

The atom bunch at launch ($z = 0$) has a central velocity $V_{z0} = 6.80 \text{ m/s}$, which decreases in the fountain as shown in Fig. 3.23. The total transit time is $t_C = 1.446 \text{ s}$. The time spent (up and down) in the D1, F2, D3, and E4 lenses is 0.67 s , and in the E4 lens it is 0.42 s (with the turnaround point 22 cm inside the E4 lens).

The initial transverse RMS sizes are $\sigma_x = \sigma_y = 1.00 \text{ mm}$ and $\sigma_{vx} = \sigma_{vy} = 14.0 \text{ mm/s}$ with an RMS emittance area of $A_x = A_y = 44 \text{ mm}^2/\text{s}$. The transverse beam envelope for the design optics considered here is shown in Fig. 3.24.

In the design optics shown in Fig. 3.24, the BD-BF doublet focuses the initial RMS beam envelope to a small double waist at the state-selection position ($Z_{si} = 167 \text{ cm}$) just in front of the D1 lens. This

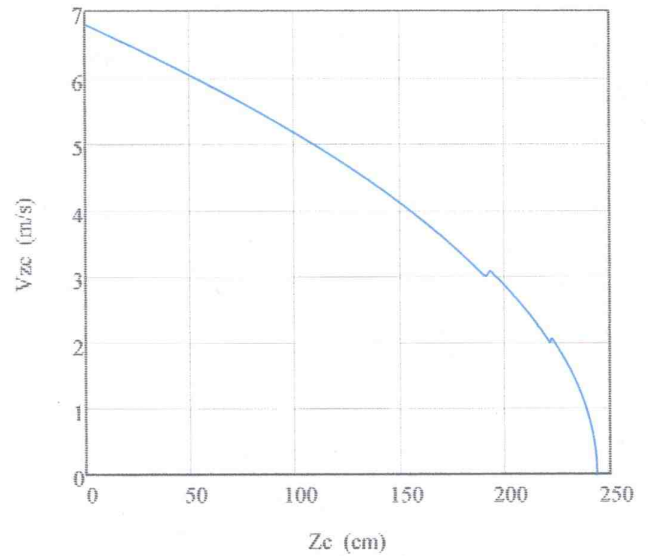


Figure 3.23: The eEDM-fountain's central bunch velocity.

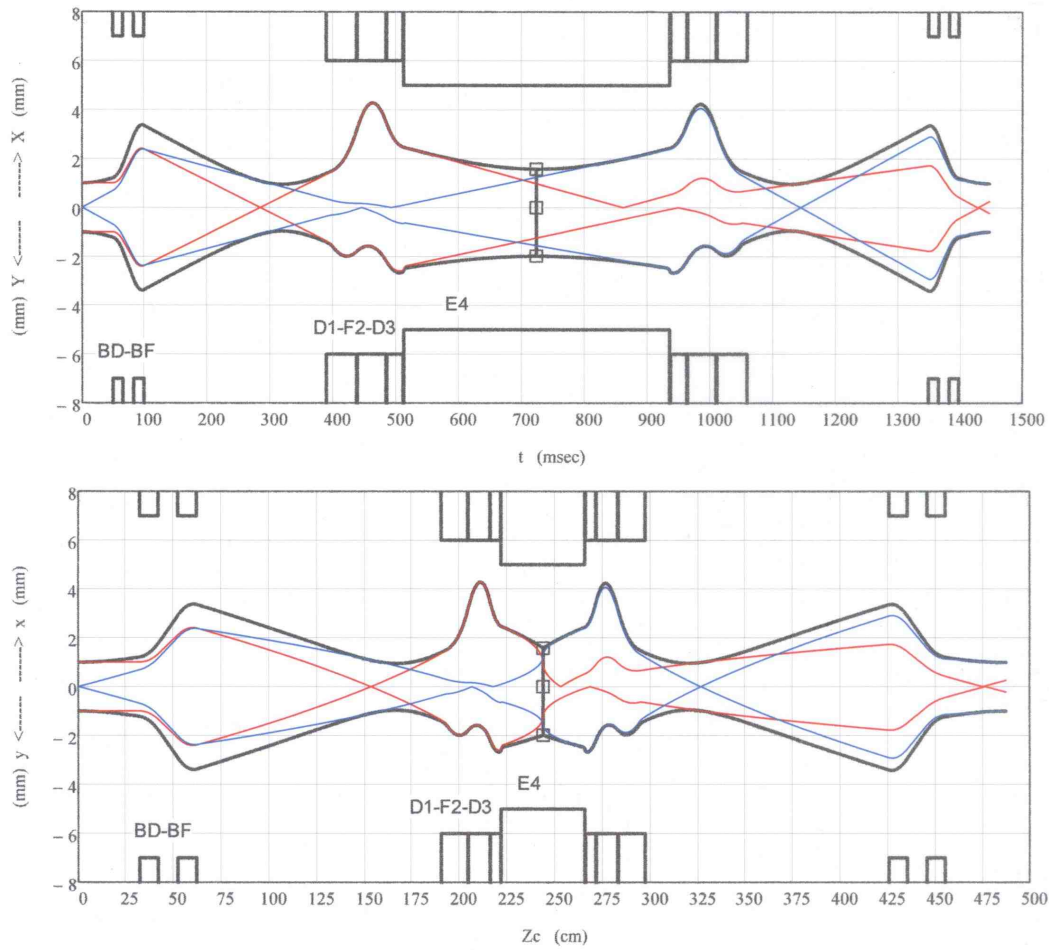


Figure 3.24: The electron EDM-fountain RMS envelope as a function of travel time (upper figure) and travel distance (lower figure). The red lines show the trajectory of francium atoms with no initial transverse velocity but with displacements of 1 mm from the axis. The blue lines show the trajectory of francium atoms with initial transverse velocity of 14 mm/s but no initial displacement. The outboard set of black curves shows the trajectory with both 1 mm displacement and 14 mm/s initial transverse velocity. In each graph, the upper (lower) curves are for the x (y) direction. The center of each figure is the turnaround of the fountain (≈ 723 ms and 244 cm). The focusing doublet (BD-BF) and triplet (D1-F2-D3) and main electric field plates (E4) are depicted schematically at the top and bottom of each figure. There is no restriction in the x direction.

minimizes the end-field defocusing of the atoms at the entrance of the D1 lens, and reduces the phase-space emittance growth from the state-selection process. This intermediate focal point also allows us to tune the BD-BF doublet and the D1-F2-D3 triplet independently of each other. The D1-F2-D3 triplet focuses the beam to a weak double waist at the turnaround point ($Z_{rev} = 244$ cm), to maximize the phase-space acceptance and reduce the change in beam size due to focusing-field perturbations.

3.12.6 Emittance Growth from State Preparation

State preparation will increase the temperature of the atom bunch (Table 3.10), and will therefore produce emittance growth in the beam²³. This increase

²³State analysis also heats the beam but at this point the atoms have already traveled through the electric field and so have few restrictions, are accelerating under gravity, and only

will be primarily in the velocity, since the state-selection region is short (impulse force) and so will produce little change in displacement.

Table 3.10: Beam Heating from State Preparation

Location	Quantity	Direction	
		x	y & z
Launch	Temp. T_i (μK)	2.5	2.5
	RMS vel. v_i (mm/s)	14.0	14.0
Prep.	Temp. inc. ΔT_s (μK)	2.2	0.5
	Final temp. T_f (μK)	4.7	3.0
	RMS vel. v_f (mm/s)	19.2	15.4

If the atom bunch at state-selection has a RMS-size $\sigma_r(r = x, y, z)$, we can estimate the emittance growth to be $\Delta\epsilon_r \approx 2\sigma_r(v_f - v_i)$. So to minimize this, we want the beam size to be as small as possible.

The RMS-envelope (Fig. 3.24) has an approximate double waist at $z_{si} = 167$ cm on the way up ($z_{sf} = 321$ cm on the way down), where the atom bunch has a central velocity $V_{zc} = 3.7$ m/s and RMS-sizes $\sigma_x = 0.95$ mm and $\sigma_y = 0.95$ mm. This is our optimum state-selection point which will minimize the emittance growth.

At any point z in the fountain, the (x, v_x) phase-space RMS-moments ($\sigma_x, \sigma_{xvx}, \sigma_{vx}$) of the atom bunch, gives us the Gaussian Kapchinsky-Vladimirsky (KV) distribution function [KV59] for

a short time remains until recapture.

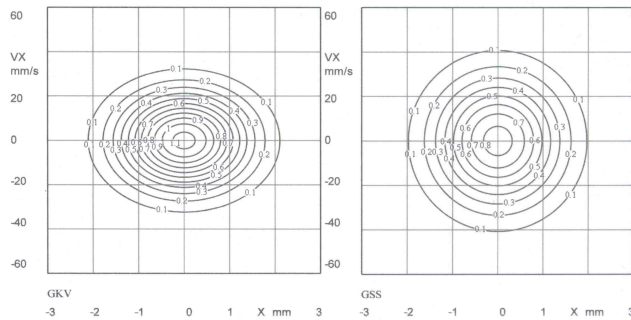


Figure 3.25: The (x, v_x) phase-space density f_{GKV} at $Z_{si} = 167$ cm; initial on left and final on right.

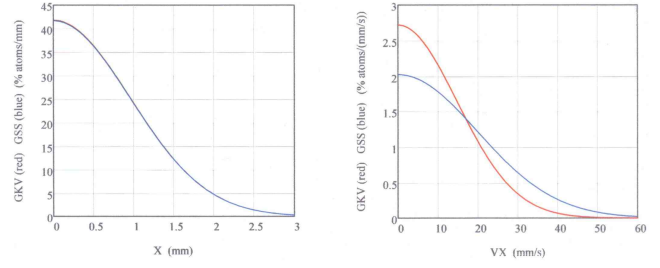


Figure 3.26: The atom density at $Z_{si} = 167$ cm in the x and v_x directions; red is the initial and blue the final.

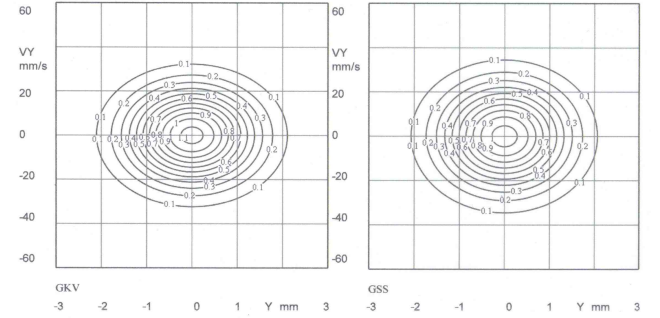


Figure 3.27: The (y, v_y) phase-space density f_{GKV} at $Z_{si} = 167$ cm; initial on left and final on right.

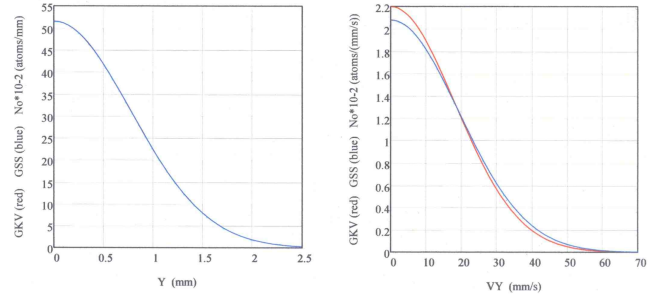


Figure 3.28: The atom density at $Z_{si} = 167$ cm in the y and v_y directions; red is the initial and blue the final.

the particle phase-space density

$$f_{GKV}(x, v_x) = \frac{d^2 N}{dx dv_x} = \eta_{Gx} \exp \left[-\frac{\Gamma_{KV}(x, v_x)}{2} \right]$$

where the central density is:

$$\eta_{Gx} = \frac{N_0}{2\pi \epsilon_{x0}},$$

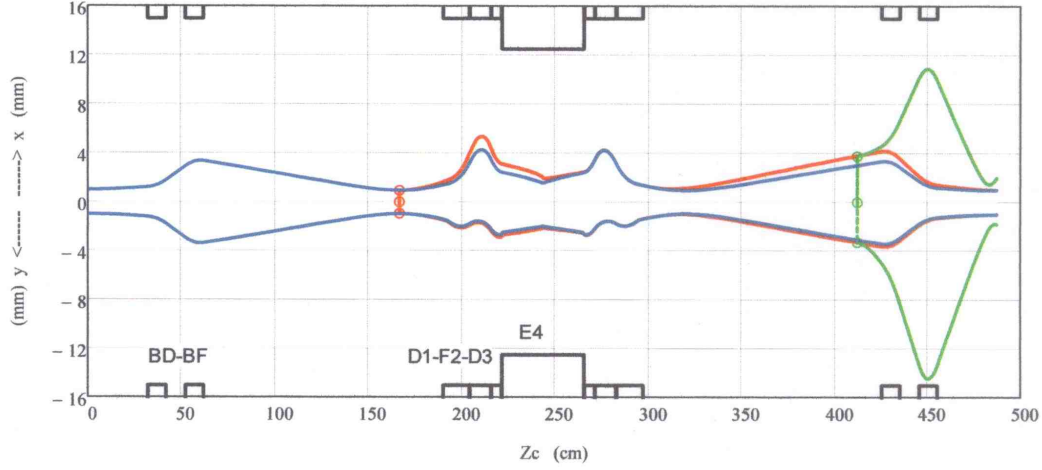


Figure 3.29: The effect on the RMS beam size (blue) of the heating in the state selection at $Z_c = 167$ cm (red) and the fluorescence region at $Z_c = 412$ cm (green). The lens apertures shown are not physical, but only give their positions in the fountain.

the total number of atoms is N_0 , the conserved emittance is $\epsilon_{x0}^2 = \sigma_x^2 \sigma_{vx}^2 - \sigma_{xvx}^2$, and the KV-invariant is

$$\Gamma_{KV} = \frac{\sigma_{vx}^2 x^2 - 2\sigma_{xvx} x v_x + \sigma_x^2 v_{vx}^2}{\epsilon_{x0}^2}$$

We have the same form for the atom distribution in the (y, v_y) phase-space. This allows us to calculate the change in the atom distribution due to state-selection, and to determine the fraction of the bunch that is transmitted to the detectors by the francium fountain phase-space acceptance area.

At the state-selection point, in the impulse approximation, the atoms' displacement in the x -direction is unchanged (RMS-size remains the same), but at each phase-space point (x, v_x) they are scattered in the v_x -direction into a Gaussian/Maxwellian distribution:

$$f_{Gvx} = \frac{dN}{dv_x} = \eta_{Gvx} \exp\left(-\frac{v_x^2}{2\sigma_{vx}^2}\right)$$

where the central density is:

$$\eta_{Gvx} = \frac{dN}{\sqrt{2\pi} \sigma_{vx}},$$

and $dN_0 = f_{GKV}(x, v_x) dx dv_x$ is the number of atoms at in the phase-space area $dA_x = dx dv_x$.

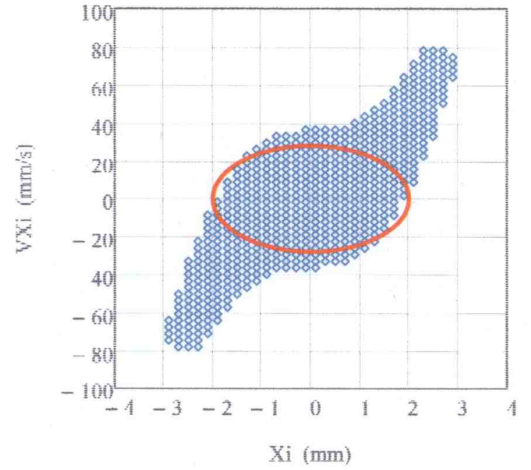


Figure 3.30: The (x, v_x) phase-space acceptance area A_{acc} at the launch position ($Z = 0$), is shown in blue (physical apertures and nonlinear forces included), with a 2 RMS beam ellipse shown in red for comparison.

- (x, v_x) phase-space: The atom distribution in the (x, v_x) phase-space, before (left) and after (right) state-selection, is shown in Fig. 3.25, where the 2D phase-space density is given in % beam atoms/(mm²/s).

The emittance growth in the x -direction due to state-selection is 33%. The projections of the atom distributions onto the x and v_x axes are

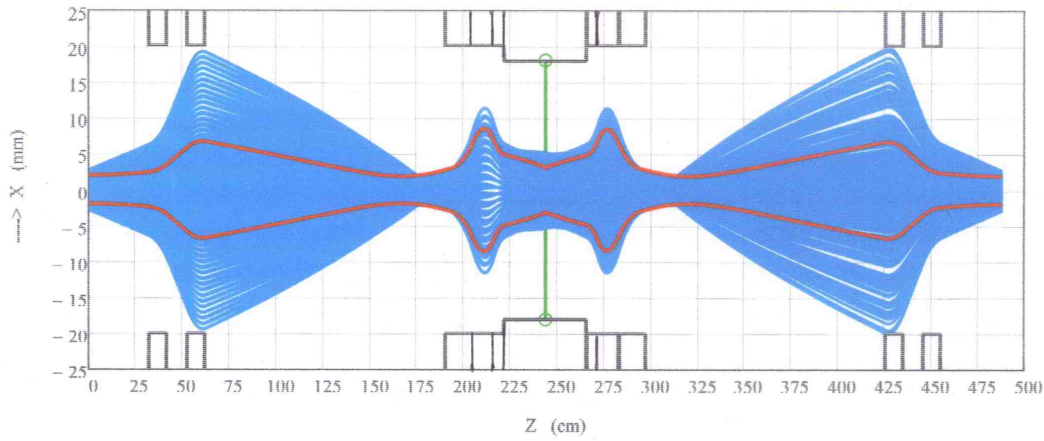


Figure 3.31: The A_{xacc} acceptance-area trajectories (blue) in the francium fountain with a 2 RMS beam envelope (red) shown for comparison (physical apertures shown are not physical but only give their position in the fountain).

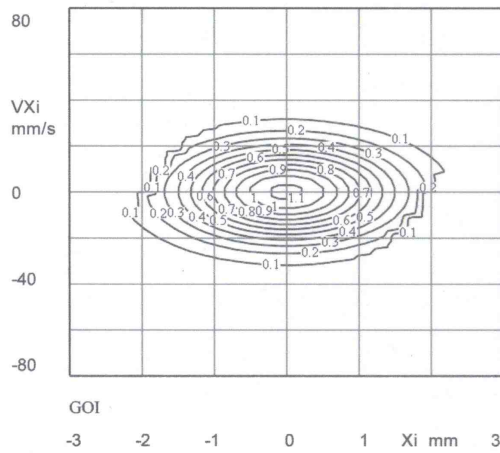


Figure 3.32: The (x, v_x) phase-space beam density (% atoms mm^{-2}s) inside the acceptance area A_{xacc} (Fig. 3.30) at the launch position ($Z = 0$) includes 92% of the beam.

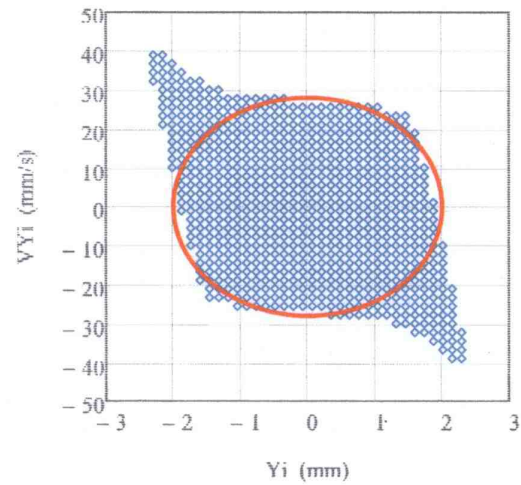


Figure 3.33: The (y, v_y) phase-space acceptance area A_{yacc} at the launch position ($Z = 0$) is shown in blue (physical apertures and nonlinear forces included), with a 2 RMS beam ellipse shown in red for comparison.

shown in Fig. 3.26. As expected there is no change in the beam size, but the RMS velocity increased from $\sigma_{vx} = 14.7 \text{ mm/s}$ to $\sigma_{vx} = 19.5 \text{ mm/s}$.

- (y, v_y) phase-space: The atom distribution in the (y, v_y) phase-space, before (left) and after (right) state-selection, is shown in Fig. 3.27. The emittance growth in the y -direction due to state-selection is 9%. The projection of the atom distributions onto the y and v_y axes are shown in Fig. 3.28. There is no change

in the beam size and the RMS velocity increased only slightly from $\sigma_{vy} = 14.7 \text{ mm/s}$ to $\sigma_{vy} = 15.9 \text{ mm/s}$.

In Fig. 3.29 we show the change in the beam RMS-envelope due to the state-preparation emittance growth (33% in x and 9% in y) at $z_{si} = 167 \text{ cm}$ (red square). Here in blue is the RMS beam size without state preparation and in red the beam size afterwards.

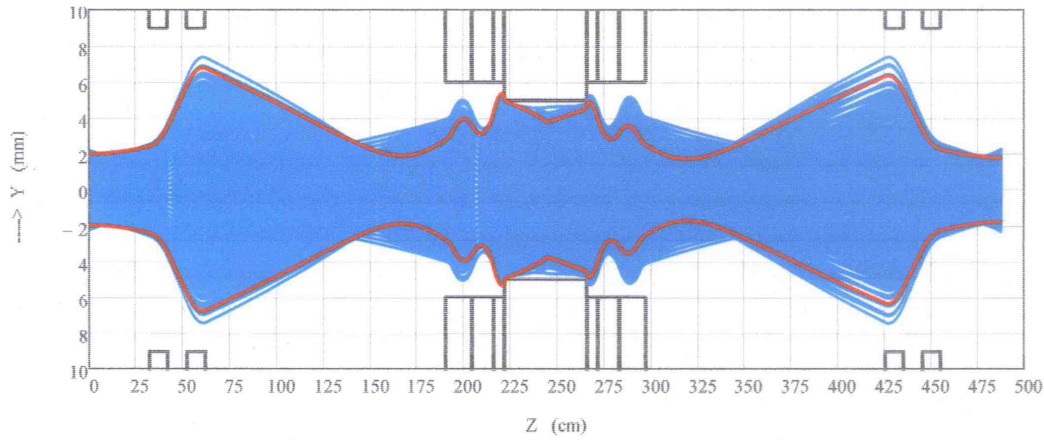


Figure 3.34: The A_{yacc} acceptance-area trajectories (blue) in the fountain with a 2 RMS beam envelope (red) shown for comparison (the lens apertures shown are the physical ones except for the BD–BF doublet where they only give their position in the fountain).

As we see, there is only a small effect on the beam size in the y -direction.

3.12.7 The (x, v_x) Phase-Space Acceptance and the Nonlinear Forces

In the x -direction the 33% increase in the RMS velocity produces a significant increase in the beam size inside the D1–F2–D3 triplet (Fig. 3.29 [red]) on the way up, but not on the way down, and this will result in some small beam loss from the nonlinear lens forces.

In the x -direction the phase-space acceptance area A_{xacc} at the launch position ($Z = 0$), with the physical apertures and nonlinear forces included in the trajectory calculation, is shown in Fig. 3.30 in blue, with a 2 RMS beam ellipse shown in red. The fountain acceptance has a phase-space area of $A_{xacc} = 375 \text{ mm}^2/\text{s}$ which is much larger than the 2 RMS beam ellipse area of $A_{xrms} = 176 \text{ mm}^2/\text{s}$.

The A_{xacc} acceptance-area trajectories in the francium-fountain are shown in Fig. 3.31, for an aperture limit of 20 mm in the BD–BF doublet, and a good-field half-width of 12 mm in the D1–F2–D3 triplet (In the figure the D1–F2–D3–E4 apertures shown are nonphysical—they are only used to show

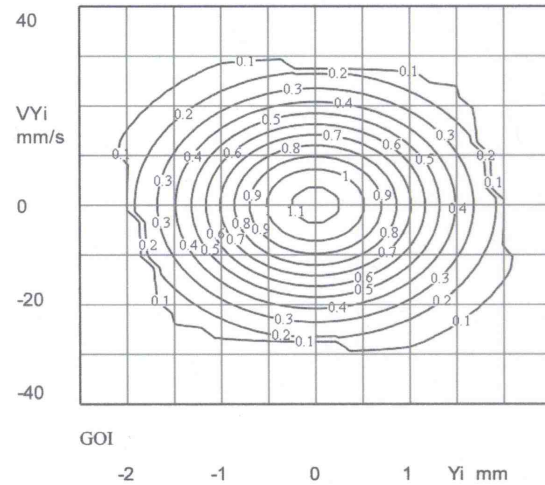


Figure 3.35: The (y, v_y) phase-space beam density (% atoms $\text{mm}^{-2} \text{s}$) inside the acceptance area A_{xacc} (Fig. 3.33) at the launch position ($Z = 0$) includes 89% of the beam.

the lens positions).

For a Francium beam with initial RMS size $\sigma_x = 1 \text{ mm}$ and $\sigma_{vx} = 14 \text{ mm/s}$, the 2D phase-space beam density (% atoms/(mm^2/s)) in the A_{xacc} acceptance area (Fig. 3.30) is shown in Fig. 3.32, and includes 92% of the beam.

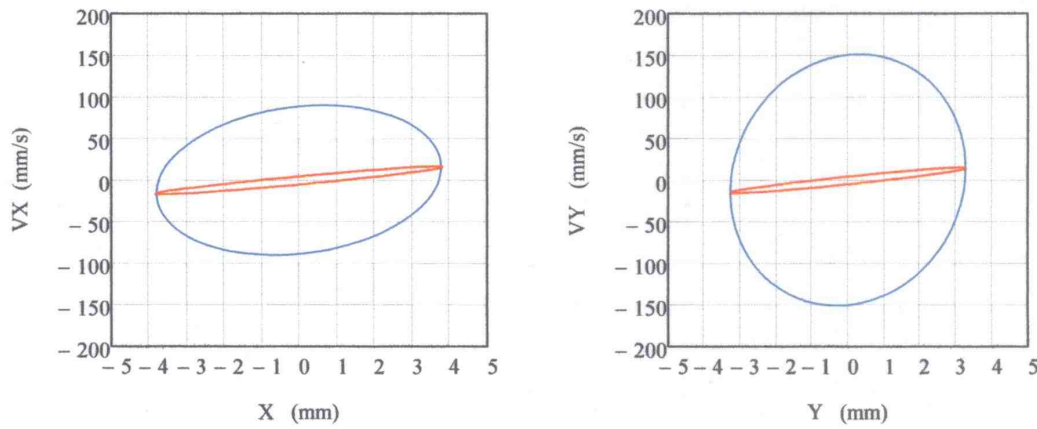


Figure 3.36: The beam RMS phase-space ellipse entering (red) the fluorescence region at $Z_{rf} = 412$ cm, and its growth after heating (blue).

3.12.8 The (y, v_y) Phase-Space Acceptance and the Nonlinear Forces

In the y -direction the phase-space acceptance area A_{yacc} at the launch position ($Z = 0$), with the physical apertures and nonlinear forces included in the trajectory calculation, is shown in Fig. 3.33 in blue, with a 2 RMS beam ellipse shown in red. The fountain acceptance has an phase-space area of $A_{yacc} = 221 \text{ mm}^2/\text{s}$, which covers most of the 2 RMS beam ellipse of area of $A_{yacc} = 176 \text{ mm}^2/\text{s}$.

The A_{yacc} acceptance-area trajectories in the francium fountain are shown in Fig. 3.34, for a D1–F2–D3 plate half-gap of 6 mm, and an E4 plate half-gap of 5 mm (In the figure the BD–BF doublet apertures shown are nonphysical—they are only used to show the lens positions). As can be seen, the acceptance is totally determined/limited by the E4 lens gap-width—which has to be small because of the large main electric field.

For a Francium beam with initial RMS size $\sigma_y = 1 \text{ mm}$ and $\sigma_{vy} = 14 \text{ mm/s}$, the 2D phase-space beam density (% atoms/(mm^2/s)) in the A_{yacc} acceptance area (Fig. 3.33) is shown in Fig. 3.35, and includes 89% of the beam. The transverse (x, y) phase-space acceptance should then transport about 82% of the initial beam back to its launch point.

3.12.9 Recovery of Atoms into the Launching Trap

The francium fountain transverse acceptance will transport about 92% of the initial beam in the x phase space and about 89% in the y phase space. We therefore expect that about 82% of the initial beam will return to the launch point. It will be possible to decelerate and cool these atoms after detection and return them to the launching trap to

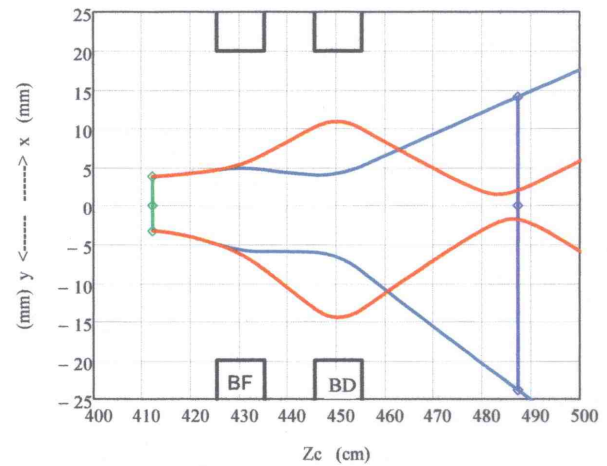


Figure 3.37: The RMS beam envelope after heating in the fluorescence region, for the BD–BF doublet focusing polarity σ_B on the way down, the same as on the way up (blue) and with it reversed (red). Also see Table 3.9.

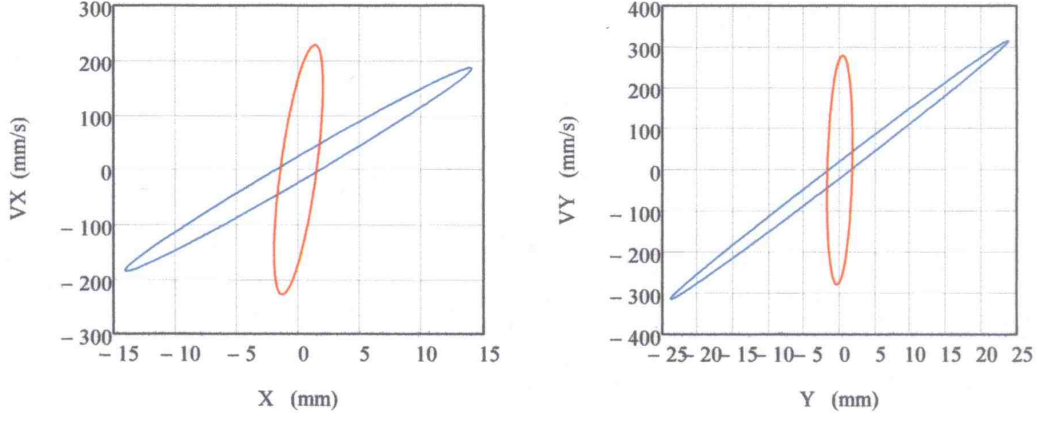


Figure 3.38: The RMS phase-space ellipse at the launch MOT, for the BD-BF doublet focusing polarity σ_B on the way down, the same as on the way up (blue) and with it reversed (red). Also see Table 3.9.

be reused, provided one keeps the expansion of the beam due to heating in the fluorescence region under control.

Atoms that arrive in the upper fluorescence region in the lower $S_{1/2}$, $F = 4$ hyperfine level are not fluoresced at all and so arrive in the lower fluorescence region cold. After fluorescence in the lower region these atoms will then have

$$\begin{aligned} \langle v_y^2 \rangle^{1/2} &= \langle v_z^2 \rangle^{1/2} = 0.107 \text{ m/s} \\ \langle v_x^2 \rangle^{1/2} &= 0.0909 \text{ m/s} \end{aligned} \quad (3.111)$$

Atoms that are fluoresced in the upper region arrive in the lower region with contributions to rms velocity and position of

$$\begin{aligned} \langle v_y^2 \rangle^{1/2} &= \langle v_z^2 \rangle^{1/2} = 0.107 \text{ m/s} \\ \langle v_x^2 \rangle^{1/2} &= 0.0909 \text{ m/s} \end{aligned} \quad (3.112)$$

After being heated again, the rms velocities in the directions transverse to the laser increase by a factor of $\sqrt{2}$ to

$$\begin{aligned} \langle v_y^2 \rangle^{1/2} &= \langle v_z^2 \rangle^{1/2} = 0.152 \text{ m/s} \\ \langle v_x^2 \rangle^{1/2} &= 0.0909 \text{ m/s} \end{aligned} \quad (3.113)$$

We see that the atom bunch is strongly heated in the fluorescence region at travel distance $Z_{rf} = 412 \text{ cm}$ (75 cm above the launch MOT). In the

x phase space, the initial temperature of $4.7 \mu\text{K}$ (19 mm/s) increases to $105 \mu\text{K}$ (91 mm/s), resulting in an 18-fold increase in the emittance. The initial (red) and final (blue) RMS (x , v_x) phase-space ellipses are shown in Fig. 3.36.

The result of the very large emittance growth in both x and y phase space is that the BD-BF doublet can no longer focus the beam, as we see from the RMS beam envelope in Fig. 3.37 (blue). To refocus the beam, we optically pump the atoms using a circularly polarized beam into the upper hyperfine level $S_{1/2}$, F and into the particular state $|FF\rangle$ so that all the atoms will be focussed identically by the pair of magnetic lenses.

By reversing the states of the atoms returning to BF and BD from those used at launch, the focusing polarities σ_B of the BD-BF doublet are reversed (BD lens becomes focusing and BF lens becomes defocusing), and then for the same magnetic field strengths B_{s2} in the lenses (Table 3.9), we can focus the beam down to a small RMS size of about 2 mm at the launch MOT as shown in red in Fig. 3.37.

The RMS phase-space ellipses at the MOT ($Z = 487 \text{ cm}$ transit distance) are shown in Fig. 3.38, where the RMS sizes of the focused beam (red) are $\sigma_x = 2.0 \text{ mm}$, $\sigma_{vx} = 230 \text{ mm/s}$, $\sigma_y = 1.8 \text{ mm}$, and $\sigma_{vy} = 280 \text{ mm/s}$. The transverse velocities are a factor of 40 below the capture velocity of a francium MOT. To transport the beam without loss,

the good-field half-aperture of the BD–BF doublet should be at least 45 mm (three RMS).

During the approximately ten seconds between launches, about 3.6% of the recaptured ^{211}Fr atoms will undergo radioactive decay. If 2/3 of the atoms launched return to the launch MOT and are captured, then after about ten cycles, the recaptured atoms added to the atoms from the collector MOT will boost the average number of atoms in the experiment by a factor of 2.7. If, we achieved the calculated transport efficiency of 82% the average number of available atoms would increase by a factor of 4.6.

3.13 Deflection Due to Electric Field Plate Misalignment

Problems caused by misalignment

If the electric field plate gap is wider at one side (x direction in Fig. 3.1 (b)), the resulting electric field gradient (See Eq. 3.106) will deflect the atoms towards the narrow side of the gap and can possibly lead to a loss of atoms. The effect is cumulative over the time spent in the electric field, making the deflection largest on the descent. Beam transport is however not especially sensitive to the atoms' descent: the defocusing effects upon the atoms' exit from the electric field is followed by the atoms passing through state analysis and detection which do not have the severe space constraints of the electric field plates. Also the atoms are accelerating so that their remaining time in the fountain is small.

If, in an extreme case, the displacement were very large, the francium atoms would approach the edge of the main electric field plates, where the drop in electric field creates a restoring force that will reflect atoms back towards the center. This restoring force also defocuses the atoms in the direction of the main electric field (y direction in Fig. 3.1 (b)) causing some of the atoms to strike the plates with

a subsequent loss of atoms. Consequently it is desirable to keep these gradients small and possibly to correct for them²⁴.

The possibility that ascending and descending atoms, because they follow different paths, may on average be subject to slightly different magnetic fields and field gradients is already taken into account in the experimental method for suppressing systematic effects (Section 3.7.3, Chapter 5, and [WMJ12]). The trajectory does not change when the electric field is reversed, and absent an EDM, the phase advance from magnetic fields and electric field will not change from their integral values of π when the electric field is reversed. Any resulting systematic effects will therefore occur in a higher order than the proposed experiment is sensitive to. And it is straightforward to test for the effect of different ascent and descent trajectories.

Size of misalignment

To understand the possible size of an electric field plate gap misalignment, we note the measured plate gap misalignment from a set of electric field plates used for cesium scalar polarizability measurement [AG03]. The electric field plates had a gap spacing of 3.98 mm with a variation in the gap spacing of up to 4 microns. The variation varied over the length of the plates and was largely random. If the same four micron variations occur in the EDM experiment and rather than being random, are uniform (with one side of the electric field plates having a gap spacing 4 microns larger), then from Eq. 3.106, the francium fountain will be deflected by nearly 2 mm over its trajectory through the main electric field plates. This is small compared to the transverse beam dimensions and small compared to the approximately $x = \pm 12.5$ mm linear region of the electrostatic triplet lenses. Consequently, this amount of misalignment would not pose a beam loss problem for the experiment.

²⁴Variations in the gap spacing over the vertical dimension cause the atoms to speed up or slow down by a few mm/s. This has no effect on the experiment.

To understand the effect of random plate gap variations on beam trajectories, we undertook a calculation described in Appendix A. The results are that for an RMS plate gap deviation of ± 1 micron and maximum gap deviation of 4 microns, the average trajectory deviation is no larger than 1.0 mm and the RMS deviation in the beam trajectory is 0.7 mm.

Again, deflections considerably larger than this are not likely to cause a significant loss of signal because most of the consequences manifest themselves on the descent, after the atoms have exited the main electric field plates, where they have sped back up to 3.5 m/s, and where only 0.5 s of their 1.5 s flight remains. Because the state analysis laser shines in the x direction, it is insensitive to the width or location of the atoms in the x direction. Because the sextupole focusing element gap is very large, and because of its proximity to the MOT, there is little time for nonlinear focusing effects to distort the beam reaching the detector.

Managing misalignment and its effects

The electric field plates used for the cesium polarizability experiment [AG03] were machined from aluminum alloy with the gap spacing determined by alumina spacers. The only concession to maintaining uniformity was that all of the spacers were ground simultaneously and the two electric field plates were milled (using an ordinary milling machine) in the same fixture. To ensure that beam deflection from misaligned electric field plates is not a problem in the EDM experiment, some or all of the following steps will be investigated as needed:

1. The electric field plates will be designed and fabricated in a way that minimizes the variation in gap spacing in the x direction²⁵. This may include precision machining, attention to how the plates are mounted in the apparatus

²⁵For EDM measurements, we care about the uniformity of the gap spacing: the actual value should be measured but it need not be set beyond that needed for beam transport and maintaining the electric field. For tensor polarizability experiments, measuring the gap spacing to 100 microns is more than sufficient.

to equalize stress, and consideration of temperature control measures. A metal prototype will be tested (Section 7.2) with extensive beam diagnostics.

2. If there is a net transverse deflection in the electric field plates, its average can be compensated by the laser beams used for state preparation (or even state analysis) in which two beams counter propagate in the x direction. Balanced intensity minimizes displacement by absorption and emission of the laser beams but it is a simple matter to unbalance the beams to provide a small transverse velocity. The photon recoil velocity being about 2.8 mm/s for francium and the transit time from the state preparation to the exit of the electric field being 0.67 s, the atoms can have an average of deflection of 2 mm as well as more or less.
3. We can add a set of electrostatic deflector plates—very short electric field plates with deliberate misalignment—at the bottom of the D1 triplet element. The atoms will make a second pass through the deflection region on their descent, but they are traveling fast, the time to the detector is short, and as noted above, alignment in the detector is not critical. Calculations will be done to evaluate this option's range of usefulness.
4. The beam trajectory can be changed by changing the orientation of the magnetic sextupole doublet and/or its displacement. This could cause the atoms to arrive at the electric field plates either slightly displaced from the centerline and/or with a slight transverse velocity.
5. Should all else prove unsatisfactory, we can add piezoelectric translators at ground potential to adjust the gap spacing. The translators push against the spacers that in turn push against the backing plates so as to slightly distort the electric field plate backing plate slightly, reducing the gap spacing. Adjusting the plate gap uniformity using piezoelectric translators would be done after the electric field plates were installed and under voltage. Again, beam diagnostics, described in the next section, will allow fine tuning of the beam trajectories.

3.14 Beam Diagnostics – Imaging the Beam

3.14.1 Viewing Transverse to the Atomic Beam

To provide the diagnostic information needed to tune the atomic optics we need to image the spatial distribution of the atomic cloud at select points along the trajectory of the atomic beam.

We begin by examining the image accumulated as a sausage-shaped atomic cloud falls through a fixed laser. We use the atomic beam coordinate system where the atomic cloud falls vertically parallel to the z axis, where the lasers that fluoresce the cloud run horizontally parallel to the x axis, and where the cloud is observed by an optic aligned with the y axis. The chief information we would seek would be the distribution of the cloud in x , averaged over y and z .

The previous estimates suggest that a cloud of 10^6 atoms can be made to scatter $1.11 \cdot 10^{10}$ photons as it falls at 5.5 m/s through a pair of anti-propagating laser beams tuned to the cycling transition and of 6 mm nominal diameter. We use 10^6 atoms here because until the apparatus is tuned up we will be working with fewer than our expected 6×10^8 atoms/launch and because we might want to launch more frequently than every ten seconds to speed the tuning process.

A suitable camera such as the Hamamatsu C9100-23 contains an 8.2 mm square CCD (charge-coupled device) chip with a 512×512 pixel array. A so-called back-thinned CCD chip puts the gate electrodes on the back of the chip where they do not obstruct the light that enters. The effective quantum efficiency averaged over the chip surface is > 0.75 for photons of wavelengths between 718 nm and 780 nm. Could we but use the unit magnification optic already described (See Fig. 3.13), with its essentially 100% collection efficiency over a cone of 20° half-angle (equal to a fraction $3.01 \cdot 10^{-2}$ of 4π steradians), to transfer the photons directly from the cloud to the

chip, we would record roughly

$$1.11 \cdot 10^{10} \times 3.01 \times 10^{-2} \times 0.75 = 2.52 \times 10^8 \quad (3.114)$$

electrons per cloud. If the atomic cloud were 4 mm wide, with a unit magnification optic, the photons would be confined on the chip to a rectangle 4 mm wide, and the height of the rectangle would equal the 6 mm nominal diameter of the fluorescing laser. The number of pixels in this rectangle would be

$$\frac{4 \text{ mm} \times 6 \text{ mm}}{(8.2 \text{ mm})^2} \times (512)^2 = 9.36 \cdot 10^4, \quad (3.115)$$

which is an image with a more than sufficiently fine granularity, and the number electrons stored per pixel would be

$$\frac{2.62 \cdot 10^8}{9.36 \cdot 10^4} = 1.19 \times 10^5. \quad (3.116)$$

The electron capacity of a pixel [pix] is nominally 3.7×10^5 , so all these counts would actually be useful.

The readout of a CCD pixel introduces a certain amount of noise. The CCD technology uses an on-chip Floating Diffusion Amplifier (FDA) to convert an accumulated charge into a voltage; the noise introduced by the amplifier is usually expressed in terms of an effective fluctuation in the number of electrons stored in the pixel. The slower the readout, generally the lower the amplifier noise. There is also thermal dark noise, which can be reduced by cooling the CCD; a cooled CCD camera such as the Hamamatsu ORCA II [hamc] achieves a readout noise of 4 electrons root-mean-square per pixel. Readout noise can be reduced further by introducing an electron-multiplication stage between the CCD pixel and the readout, to make the amplifier noise a smaller fraction of the total signal; cooled cameras that use such Electron-Multiplier CCD chips, such as the Hamamatsu C9100-13 camera [hamd], achieve total noise whose equivalent is 1 electron root-mean-square per pixel.

Obtaining such a low noise requires the slowest of the readout speeds; nonetheless an entire image can be read out in less than 0.5 s, which is adequately short compared to the multiple second intervals between launches of new clouds of atoms. We will take

5 electrons rms as a working estimate for an easily achieved noise per pixel.

We have somehow to get the light out of the innermost magnetic shield. The simplest idea is to image a roughly 3 mm diameter cloud using a unit-magnification optic onto a 3 mm \times 3 mm square coherent fiber-optic cable, such as for example the cable manufactured by Schott [Sch]. The numerical aperture for acceptance into this cable is 0.6, generously large compared to the 0.342 numerical aperture that is required to accept all light within a cone with a half-angle of 20°. The transmission through the cable falls short of unity essentially because the core of the optical fibers does not cover all the cross sectional area of the cable; for the Schott cable the fraction incident that is transmitted is 0.40, which is acceptable. The cable is available in lengths up to 4.5 m, which is sufficient.

At the opposite end of the cable we can again use a unit-magnification optic to image the end of the cable onto the CCD chip. Because the diameter of a whole fiber, 10 μ m, is a rough match to the length of a square side of a CCD pixel, there is no significant loss in resolution caused by transmitting an image through the cable. The angular acceptance of the CCD chip is determined by the box that surrounds it, but is a rough match to a cone of half-angle 20°.

While it would be possible to bond the end of the cable directly to the chip, this would require a custom construction and it should prove easier merely to focus the light from the cable onto the chip through its insulating vacuum window. It would be possible to design a custom fiber optic that took, say, four separate 3 mm \times 3 mm square fiber bundles and to assemble them into a single square block the end of which could be imaged with unit magnification onto the 8.2 mm \times 8.2 mm CCD chip; in this way we could take the two horizontal images of a nominally 1 mm diameter beam at either of two vertical locations and not require more than the one CCD camera.

Whether the standard optical fiber bundle, particularly its plastic sheathing, is sufficiently nonmagnetic to use inside the innermost magnetic shield will have to be researched.

The quality of the image is limited by both the 10 μ m diameter of the optical fiber and by the 16 μ m \times 16 μ m size of the pixel on the chip. More subtly, even an atom initially at rest will suffer random displacements as photons scatter and transfer momentum to the atom; even the light from this single atom will therefore be imaged onto a spot with a finite size. The atom has a faster growth in rms velocity in the direction of the laser beam, and a smaller growth in directions transverse to the laser beam.

We will ignore the phenomenon of Doppler cooling and so get an upper limit on the size of the effect. For a circularly polarized beam and a unit magnification optic, the spot size projected onto the CCD surface is [Mun07a]

$$\frac{1}{2\sqrt{3}} v_r T \sqrt{N} \times \begin{cases} \sqrt{3/10} & \text{transverse to laser beam} \\ \sqrt{7/5} & \text{parallel to laser beam} \end{cases} \quad (3.117)$$

Here T is the total time over which the atoms are fluoresced, N is the number of photons scattered by an atom, and v_r is the velocity imparted to an atom at rest by the absorption of one laser photon. For $T = 1.09 \times 10^{-3}$ s and $N = 1.11 \times 10^4$ and $v_r = 2.64 \times 10^{-3}$ m/s, the resulting rms sizes for ^{211}Fr are respectively

$$\begin{aligned} \langle y^2 \rangle^{1/2} &= \langle z^2 \rangle^{1/2} = 48 \mu\text{m} , \\ \langle x^2 \rangle^{1/2} &\leq 104 \mu\text{m} . \end{aligned} \quad (3.118)$$

Another estimate takes into account the phenomenon of Doppler cooling. For a detuning of $\Delta/\Gamma = \sqrt{3}/6$ we have seen the velocity parallel to the beam will increase and equilibrate to

$$\langle v_x^2 \rangle^{1/2} = 0.0909 \text{ m/s} ; \quad (3.119)$$

if we imagine that the entirety of this warming occurred at time zero and the resulting hot distribution merely expanded over the time T the atom was within the laser, we would obtain the estimate

$$\langle x^2 \rangle^{1/2} \leq 99.3 \mu\text{m} . \quad (3.120)$$

Using a laser that wasn't round but was a ribbon, with a width still of 6 mm but a height of 1.5 mm, would reduce the time T by a factor of 4 and so the

blur in $\langle x^2 \rangle^{1/2}$ also by a factor of 4, to $25 \mu\text{m}$; the cost would be a reduction in the number of counts by this same factor of 4, which we can afford.

The image quality is also blurred by the finite depth of the cloud. If an atom displaced by 2.0 mm away from the object location of the optical periscope, then light emitted at a half-angle of 20° will not hit the center of the image but will fall on the edge of a circle of radius

$$r = 2.00 \text{ mm} \times \tan(20^\circ) = 728 \mu\text{m} , \quad (3.121)$$

and so from light from this location the spot on the image plane will have transverse dimensions with rms sizes of

$$\langle x^2 \rangle^{1/2} = \langle y^2 \rangle^{1/2} = r/2 = 364 \mu\text{m} ; \quad (3.122)$$

if one averages over the depth of the cloud of assumed uniform density the resulting blur would be smaller by yet another factor of 2, or $182 \mu\text{m}$. We have so many photons available to form the image that reducing the number of photons collected by a factor of 6 by installing a slit to reduce the blur of the image in x by a factor of 6, down to $31 \mu\text{m}$ is entirely feasible. The unit-magnification optic already discussed has a finite spot size (nominal diameter $40 \mu\text{m}$) when an atom is located at its focus, but a ray is emitted at a full 20° with respect to the optical axis; this blurring too diminishes when the aperture is stopped.

In summary, lowering the counts per pixel by a net factor of 24 to 5000, still a factor of 1000 larger than the assumed readout noise, would give a net blur in the transverse direction of

$$\langle x^2 \rangle^{1/2} = [(25 \mu\text{m})^2 + (31 \mu\text{m})^2]^{1/2} = 40 \mu\text{m} , \quad (3.123)$$

which is about 2 orders of magnitude less than the nominal width of the cloud.

3.14.2 Viewing Parallel to the Atomic Beam

Another approach to viewing the atomic beam is to run the fluorescence lasers vertically and to observe

the fluorescence at a small angle with respect to vertical. This would have two advantages: viewing both transverse dimensions of the atomic cloud in a single image; and being able to image the cloud at a large range of vertical positions merely by adjusting the timing of the pulse the does the fluorescence. The disadvantages are several. One is that the solid angle over which one can collect photons is limited by the $\sim 1 \text{ cm}$ gap between the electric field plates; because a 1 cm^2 point of observation $\sim 1 \text{ m}$ away subtends a fraction of 4π steradians equal to $2.5 \cdot 10^{-5}$, then the number of photons that can be collected over a nominal 0.0909 s is

$$1.11 \cdot 10^{10} \cdot 2.5 \cdot 10^{-5} = 2.8 \cdot 10^5 , \quad (3.124)$$

and if these are distributed over the $4.8 \cdot 10^4$ pixels of a 4 mm diameter image then, accounting for the quantum efficiency of the CCD chip, the number of electrons accumulated per pixel is

$$0.75 \times 2.8 \times 10^5 / 4.9 \times 10^4 = 42 ; \quad (3.125)$$

thus the modeled ~ 5 -electron readout noise becomes significant for a launch of 10^6 atoms. The vertical laser has to pass up through the plates, increasing the amount of photons that are scattered by the plate surfaces; and since one is now looking almost directly into the laser beam, it is more likely that such a photon will enter the detector. Discovering if such a viewing scheme is feasible will be part of the development work, but the purpose of establishing the feasibility of the experiment we shall not rely on it.